Dissertation

submitted to the

Combined Faculty of Mathematics, Engineering and Natural Sciences

of Heidelberg University, Germany

for the degree of

Doctor of Natural Sciences

Put forward by

Patrick Friebel

born in: Bruchsal

Oral examination: 12.11.2025

THz vibrational dynamics of Liquid Crystals:
from molecular origin to bulk response

Referees: Dr. Laura Cattaneo
Prof. Dr. Peer Fischer

Abstract

The interplay between the macroscopic collective order and the microscopic intra- to intermolecular vibrational response of the Liquid Crystal (LC) class of anisotropic molecular systems, is investigated. LCs provide an ideal platform because of their mesophase behavior, in which their collective arrangement is tunable from isotropic to orientationally and positionally ordered ensembles. The collective dynamics in molecular systems occur in the terahertz (THz) frequency range; therefore, the LCs are investigated through linear and nonlinear THz spectroscopic methods. The main LC under investigation is 4-cyano-4′-n-octylbiphenyl (8CB), and is compared to the structurally similar 4-(4′-n-octyloxyphenyl)benzonitrile (8OCB) and trans-4-(4′-n-pentylcyclohexyl)benzonitrile (PCH5), allowing the separation of single-molecule and collective contributions from the vibrational response. THz absorption spectra, measured using linear THz time domain spectroscopy (THz-TDS), allow for the identification of intramolecular vibrations above 3 THz through comparison with single-molecule gas phase DFT calculations. In contrast, the low-frequency spectrum deviates from the calculations and is associated with intermolecular interactions. Nonlinear THz Kerr spectroscopy probes the electronic polarizability and rotational diffusion dynamics of the samples. The transiently induced birefringence exhibits a signature attributed to resonant driving of the low-frequency intermolecular modes identified in the TDS spectra.

Das Zusammenspiel zwischen der makroskopischen kollektiven Ordnung und der mikroskopischen intra- bis intermolekularen Vibrationsantwort der Flüssigkristall-(LC)-Klasse anisotroper molekularer Systeme, wird untersucht. Flüssigkristalle bieten eine ideale Plattform aufgrund ihres Mesophasenverhaltens, bei dem ihre kollektive Anordnung von isotrop bis hin zu orientierungs- und positionsgeordneten Ensembles kontrollierbar ist. Die kollektive Dynamik in molekularen Systemen findet im Terahertz-(THz)-Frequenzbereich statt; daher werden Flüssigkristalle mithilfe linearer und nichtlinearer THz-spektroskopischer Methoden untersucht. Der zentrale LC dieser Untersuchung ist 4-Cyano-4′-n-octylbiphenyl (8CB), das mit den strukturell ähnlichen Verbindungen 4-(4′-n-octyloxyphenyl)benzonitril (8OCB) und trans-4-(4′-n-pentylcyclohexyl)benzonitril (PCH5) verglichen wird. Dies ermöglicht die Trennung von Molekül- und kollektiven Beiträgen zur Vibrationsantwort. THz-Absorptionsspektren, gemessen mit linearer THz-Zeitbereichsspektroskopie (THz-TDS), ermöglichen die Identifikation intramolekularer Vibrationen oberhalb von 3 THz durch den Vergleich mit Molekül-DFT-Berechnungen in der Gasphase. Im Gegensatz dazu weicht das niederfrequente Spektrum von den Berechnungen ab und wird mit intermolekularen Wechselwirkungen in Verbindung gebracht. Die nichtlineare THz-Kerr-Spektroskopie untersucht die elektronische Polarisierbarkeit und Rotationsdiffusionsdynamik der Proben. Die transient induzierte Doppelbrechung zeigt eine Signatur, die der resonanten Anregung der niederfrequenten intermolekularen Moden zugeordnet wird, die in den TDS-Spektren identifiziert wurden.

Peer reviewed publications

- *Unveiling Low THz Dynamics of Liquid Crystals: Identification of Intermolecular Interaction among Intramolecular Modes*
  Patrick Friebel, Daria Ruth Galimberti, Matteo Savoini, and Laura Cattaneo
  The Journal of Physical Chemistry B **2024** *128* (2), 596-602
  https://doi.org/10.1021/acs.jpcb.3c07947

Conference presentations

- Hot Topic Talk (selected from poster contribution, poster prize awarded) *THz vibrational dynamics of Liquid Crystals: from molecular origin to bulk response*
  838. WE-Heraeus-Seminar "Manipulating Molecular Electronic Properties by Vibrational Excitations: Novel Spectroscopies and Microscopies"
  17th - 21st August 2025, Bad Honnef, Germany

- Talk *Transient THz Kerr Spectroscopy on Liquid Crystals*
  Rank Symposium on THz Applications of Liquid Crystals
  11th - 14th November 2024, Lake District, Cumbria, UK

- Keynote Talk *Time Resolved Liquid Crystal Dynamics In Intense THz Fields*
  10th Optical Terahertz Science and Technology Conference (OTST2024)
  8th - 12th April 2024, Marburg, Germany

- Talk *Liquid Crystal Response in Intense THz Fields*
  20th Optics of Liquid Crystals Conference (OLC2023)
  17th - 22nd September 2023, Szczecin, Poland

- Talk *Ultrafast Terahertz Response of Thermotropic Liquid Crystals*
  The 15th Femtochemistry Conference (FEMTO 15)
  30th July - 4th August 2023, Berlin, Germany

Conference poster contributions

- Poster *Molecular THz vibrational dynamics of Liquid Crystals and their collective response*
  Gordon Research Conference: Connecting Molecular Structure and Dynamics to Collective Properties in the Liquid State
  3rd - 8th August 2025, Holderness, New Hampshire, United States

- Poster *Time Resolved THz Dynamcis in Thermotropic Liquid Crystals*
  Faraday Discussion: From optical to THz control of materials
  23rd - 25th May 2022, London, UK

- Poster *Time Resolved THz Dynamcis in Liquid Crystals*
  DPG Meeting SAMOP21 (virtual)
  20th - 24th September 2021

Conference proceedings

- *THz spectroscopy of thermotropic liquid crystals*
  Patrick Friebel, Daria Galimberti, Riccardo Piccoli, and Laura Cattaneo
  Proc. SPIE 12442, Emerging Liquid Crystal Technologies XVIII, 1244204;
  https://doi.org/10.1117/12.2646581

In preparation

- Transient THz Kerr spectroscopy on liquid crystals (working title)
  Patrick Friebel, and Laura Cattaneo

Related publications

- *Liquid crystal-based temperature-controlled recirculating flat jet system*
  Marta L. Murillo-Sánchez, Natalia Copete-Plazas, Elias Bürkle, Patrick Friebel, Laura Cattaneo
  Rev. Sci. Instrum. 1 October 2024; 95 (10): 103902.
  https://doi.org/10.1063/5.0210575

- *High-order harmonic generation in liquid crystals*
  Andrea Annunziata, Luise Becker, Marta L. Murillo-Sánchez, Patrick Friebel, Salvatore Stagira, Davide Faccialà, Caterina Vozzi, Laura Cattaneo
  APL Photonics 1 June 2024; 9 (6): 060801.
  https://doi.org/10.1063/5.0191184

- *Liquid crystal wave plate operating close to 18 THz*
  Fabio Novelli, Patrick Friebel, Marta L. Murillo-Sanchez, J. Michael Klopf, and Laura Cattaneo
  Opt. Lett. 49, 2061-2064 (2024)
  https://doi.org/10.1364/OL.519177

Contents

List of abbreviations

amu	atomic mass unit
DFT	density functional theory
DMOAP	N,N-dimethyl-n-octadecyl-3-aminopropyltrimethoxysilyl chloride
DSTMS	4-N,N-dimethylamino-4′-N′-methyl-stilbazolium 2,4,6-trimethylbenzenesulfonat
EOS	electro-optic sampling
FFT	fast Fourier transform
GaP	gallium phosphide
IR	infra red
LC	liquid crystal
LN	litium niobate
nCB	4-cyano-4′-n-alkylbiphenyl
NIR	near infra red
nOCB	4-(4′-n-alkyloxyphenyl)benzonitrile
OPA	opical parametric amplifier
OPM	off-axis parabolic mirror
OR	optical rectification
PCHn	trans-4-(4′-n-alkylcyclohexyl)benzonitrile
PNPA	(E)-4-((4-nitrobenzylidene)-amino)-N-phenylaniline
POM	polarized light optical microscopy
PVA	poly vinyl alcohol
RH	relative humidity
Si	silicon
SiC	silicon carbide
SiN	silicon nitride
SNR	signal-to-noise ratio
TDS	time domain spectroscopy
THz	terahertz
TOPAS	ambiguous: 1. cyclic olefin copolymer (trademark *Polyplastics*) 2. commercial optical parametric amplifier (*Light Conversion*)
VDOS	vibrational density of states
ZnTe	zinc telluride

1. Introduction

Liquid crystals (LCs) offer a unique platform to study systems exhibiting order within disorder. These materials transition into mesophases (from the greek *mesos* translating to middle or intermediate) between the isotropic liquid state and the crystalline state, which are disordered on one hand and ordered in a neat lattice on the other. They are liquid phase materials in which the constituent molecules retain their ability to flow, but additionally they show characteristics typically associated with crystalline systems, such as macroscopic alignment or positional periodicity along a given axis. LC mesophases are generated by the (anisotropic) molecular geometries, are classified by the type of molecular arrangement, and are therefore numerous. Depending on the mesophase, the molecules create a collective environment that is characterized by a certain extent of positional and orientational order, or lack thereof. This combination of properties is the rationale for the name this class of materials carries [1, 2].

Given their ability to create order, and to tune this order via phase transitions into different LC states, they allow the study of the interplay between molecular dynamics on a microscopic scale and the macroscopic collective environment. In particular, the molecular scale vibrational dynamics are expected to be influenced by the interaction with nearest neighbors. This raises questions, such as how are the intermolecular dynamics influenced by the collective order? And can these dynamics be driven and tuned in such a way, that the bulk properties are transiently modified? In this thesis, the interplay between molecular dynamics and macroscopic collective order will be investigated by means of linear and non-linear spectroscopic techniques in the terahertz (THz) domain.

THz spectroscopy has emerged relatively recently with the development of ultrafast laser systems as a unique tool sensitive to weak intermolecular forces. Vibrational dynamics in the infrared (IR) regime are confined to specific functional groups of the molecule and their spectroscopic fingerprint usually falls within a narrow frequency range. This makes chemical tagging of compounds from simple IR spectroscopy possible. In the far-IR, which is nowadays referred to as the THz spectrum, this simple mode assignment technique breaks down. Why is that the case?

Chemical bonds can be described, in first approximation, by an harmonic oscillator with a given force constant. This picture derives generally from a Taylor expansion around the minimum of the Lennard-Jones potential describing real interatomic potential energy surfaces. Stronger bonds are described by steeper potentials. In it's ground state the system is steady, and in order to launch an oscillation the ground state wave packet has to be excited, and the minimum energy required for a quantum harmonic oscillator is $\hbar\omega$. The frequency ω of the oscillation encodes the force constant of the harmonic

oscillator k and the reduced mass of the system μ by the relation $\sqrt{k/\mu}$.

This is the simplest possible picture describing intramolecular vibrations, considering isolated harmonic oscillators. In reality, many more forces are acting on each atom in the system. When the bonds are strong and the potentials steep, the possible influence from outside forces and changes to the reduced mass have little influence on the overall interatomic forces, and the expected shifts to the frequency of the oscillator remain small. For this reason, in IR spectroscopy, functional groups and the nature of their vibrations (stretch, bend,...) fall within the same window in the absorption spectrum, regardless of the details about the rest of the molecule.

The shallower the interatomic potentials are, the lower the frequency of the oscillator. Once the external forces compete with the internal forces, these outside contributions to the resulting dynamics can no longer be neglected. This can be illustrated by comparing the bond-strength of typical intermolecular forces to typical interatomic forces within the molecules. Vibrational transitions of covalent interatomic bonds are typically found at mid-IR frequencies. For example, the O-H stretch vibration is located at $3200\,\mathrm{cm}^{-1}$ to $3600\,\mathrm{cm}^{-1}$, which corresponds to $\sim$0.42 eV or $\sim$100 THz. On the other hand, the total binding energy of intermolecular van-der-Waals potentials can be found, depending on the system, between 1 meV to 70 meV, or 0.25 THz to 17 THz. This gap in relative energy scales shows clearly the sensitivity of different bond-types to environmental perturbations.

In THz spectroscopy, the recorded spectra gain significantly in complexity on one hand, but on the other hand they can be seen as highly sensitive to the surrounding environment. This transition from intra- to intermolecular vibrations falls into the low THz frequency spectrum. It is a gradual one and cannot be marked neatly by a sharp cutoff frequency that separates intramolecular modes from intermolecular ones. In this frequency range, both classes of vibrations are present with the lower frequency part of the spectrum dominated by long range interactions, and the high frequency spectrum by internal modes [3].

The exact dynamics associated with the THz spectra depend on the nature of the material. Liquid state materials behave differently to solid state samples, and within solids, inorganic crystals compared to organic ones. And crystals behave differently compared to amorphous materials. Each presents a different arrangement of differently complex smallest units, that manifest in different THz frequency dynamics.

Considering ideal crystals, where a unit cell is periodically arranged over macroscopic distance, two distinct classes can be considered. Simple inorganic crystals, where the unit cells consist of few atoms, and complex organic molecular crystals. In both cases the THz activity can be described as dipole active phonons, meaning lattice vibrations that couple to electromagnetic radiation through an induced dipole moment. In the first case, the active THz phonons in these materials are no different from optical phonons active in other IR frequency bands. For example, Tellurium has various optically active phonon modes between 2 THz to 4 THz within its unit cell consisting of three atoms, that can be described with the same concepts as lattice vibrations at higher frequencies [4].

The real advantage of THz spectroscopy is revealed when considering the more complex cases of weakly bonded molecular crystals. The development of THz spectroscopic

tools has gone hand in hand with the development of computational methods sensitive enough to understand the complex THz spectra these materials present. The result is a mature field that is capable of structure identification, competing with x-ray diffraction techniques. This sensitivity is coupled with other advantages, such as non-invasiveness and non-destructiveness.

Ideal test cases are molecules that crystallize in different polymorphic structures. Experimentally it is well-established, that two distinct forms of the same molecular crystal show significantly different THz spectra, while their mid-IR dynamics show only subtle differences. For example, L-glutamic acid crystallizes in α or β forms, with different molecular conformations (in dihedral angles), unit cells, and number of hydrogen-bonds each molecule forms. Both THz spectra show sharp absorption bands, but are overall distinct as shown in Figure 1.1a, with the clearest difference between the two forms being the complete lack of distinct features of the α spectrum below 1.5 THz [5]. Similar things can be said for tartaric acid, which forms molecular crystals in its chiral-L form, or in a DL-form in 1:1 mixture of D and L enantiomers, among others [6]. Distinct THz spectra can be found in any complex molecule that forms polymorphs, and can therefore be used for material analysis application, for example in pharmaceuticals as reviewed by Zeitler *et al.* [7, 8]. Given the strong sensitivity to the intermolecular potential environment, it is reasonable to expect the THz spectra to undergo changes with temperature, simply within the picture of thermal expansion. In fact, there is a strong interplay between the THz vibrational modes and the anisotropic thermal expansion. The measured THz spectra broaden and more importantly shift with sample temperature, because in these systems it is the softening of anharmonic intermolecular potentials that drives the thermal expansion process. This picture based on an underlying potential energy landscape is illustrated in a recent temperature dependent THz spectroscopy study on the co-crystal TMA-azo [9].

The sensitivity of THz spectra to intermolecular modes includes the direct implication that the vibrations associated with those modes involve complex movements of more than one molecule against each other. Ibuprofen has been found to exhibit hindered translations and rotations mixed with internal vibrations in the low frequency spectrum that become almost exclusively internal to the molecule above 4.5 THz [10]. Candidate molecules for organic semiconductor applications received special attention, since their charge transport performance is depending on the transfer integral between molecule pairs that have sufficient orbital overlap, for example through π-stacking. These low frequency inter-molecular motions can modulate this transport probability significantly, which is a form of electron-phonon coupling and is a process termed as dynamic disorder. For example, the linear elongated molecule 2,6-(thien-2-yl)anthracene in its crystallized form presents an anti-parallel sliding motion of two molecules facing each other at 1 THz, completely disrupting transport capability as outlined by Ruggiero *et al.* [11–13]. From these examples, it is apparent, that these low frequency intermolecular vibrations can have large effects on macroscopic bulk properties.

In order to go beyond sample tagging, and to use THz spectroscopy in vibrational mode identification and in structure investigations, computational methods are unavoidable, given the complexity of the molecules involved. Neat crystals have the advantage

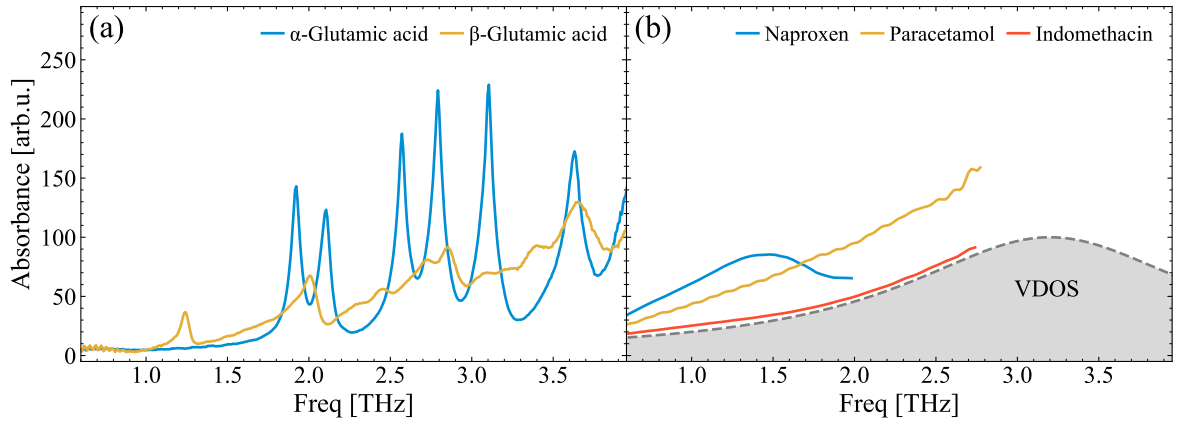

Figure 1.1.: (a) THz absorption spectra of α- and β-glutamic acid. Data taken from Ruggiero et al. [5]. (b) THz absorption spectra of amorphous pharmaceutical samples. Data taken from Sibik et al. [14]. The shaded area represents an extended qualitative picture of the VDOS band, expected for amorphous systems.

of periodicity in translation of their unit cell, which keeps the computational cost under control. The typical approach is based on Density Functional Theory (DFT), where periodic boundary conditions include the long range interactions present on THz scales [3]. The other favorable aspect from a physical perspective, is the relatively narrow width of those absorption features. The smaller the correlation length over which the vibration can be sustained, the broader the line width is. In the phonon picture, this can be described as a limitation of the life time of the phonon by scattering processes.

In the extreme limit, these materials are classified as poly-crystalline or amorphous, such as glasses. Zeitler *at al.* show that their THz spectra are characterized by a lack of any distinct and sharp features and that everything collapses into one broad absorption band, as for the amorphous molecular samples shown in Figure 1.1b [15, 16]. Often, it is referred to as the vibrational density of states (VDOS), and researches have found ways to extract information about these systems from it. Well below the the glass transition temperature of the material, it was found that the VDOS is temperature independent. In the framework of potential energy surfaces, this indicates that the system is trapped in a deep minimum. As it is heated across a critical temperature, the VDOS becomes temperature dependent, indicating anharmonic contributions to the intermolecular potential energy landscape and is connected to the onset of mobility in the system [17, 18].

Finally, weakly bound systems that exhibit strong disorder and mobility are liquids. The THz spectra measured in liquids look very similar in shape to amorphous solid spectra, but have their origin in different dynamics, given the molecular mobility within the material. The main example for liquids is naturally water, for its prevalence outside the laboratory. But there is also a deeper connection between water and THz radiation. The forces associated with the hydrogen bond network are resonant on THz scales, meaning THz light is a direct probe for the picosecond network dynamics responsible for

energy dissipation in the water matrix [19]. Beyond the direct access to hydrogen bonds, also other universal features occur in polar liquids on THz scales. Restricted rotations, so called librations, occur on THz scales and are a consequence of rotations driven by the torque exerted on the polar molecules by the external field and the restriction imposed by the presence of neighboring molecules [20].

Also non-linear THz dynamics have been a subject of study in liquids. Particularly THz Kerr Effect measurements by Sajadi *et al.* [19, 21–23] have been used to infer the third order nonlinearities $\chi^{(3)}$ and the relaxation times connected to rotational diffusion processes. Furthermore it was possible to extract the polarizability anisotropy on a molecular level [24, 25].

Clearly, there is a wide range of fundamental dynamics playing out on THz scales that originates from the exact intermolecular relationship within the material and the degree of long range order. The inherent low photon energy of THz radiation puts it into resonance with these weakly bonded systems. The vibrational modes connected to these resonances are often involving multiple molecules, which carries impact on macroscopic material properties on picosecond time scales. Hence, THz spectroscopy is a sensitive tool for investigation of intermolecular interactions, across various types of packing and order on a molecular level, as will be the point of study in this work. As presented in the opening paragraphs, LCs are a unique tunable material in this regards. This makes them, in addition to the obvious technological interest that they carried for decades, interesting from a fundamental molecular dynamics perspective.

The far-infrared properties of LCs have been studied by various groups, with the early work originating from the 1970s and 1980s. Evans *et al.* studied the monomolecular LC N-(methoxybenzylidene)-4-butylaniline (MBBA) [26] and molecules of the alkyl-4-cyanobiphenyl (nCB) family [27, 28] between 1 THz to 6 THz using early commercial far-IR spectrometers based on the Fourier Transform Infrared (FTIR) spectroscopy principle. They explained the measured spectra by a combination of intramolecular modes and Poley absorption (rotational oscillations of polar molecules) assigned to the low frequency band. In order to isolate the Poley absorption, they experimented with designing more rigid molecules that have dipole moments pointing perpendicular to the long axis of the molecule [29]. Murphy *et al.* performed similar studies and speculated about the additional presence of pseudo-lattice modes [30].

In parallel to these linear absorption studies and into the 2000s, research groups started to exploit new pulsed ultrafast laser systems for investigations of non-linear dynamics of materials, including LCs. Using the Transient Grating technique, Fayer *et al.* found for different LC compounds in isotropic and nematic phase reorientational dynamics on sub-ps time scales. The laser field couples to the molecular polarizability leading to a coherent librational motion de-phasing within 2 ps [31, 32].

Also within this context of non-linear dynamics fall studies based on optical Kerr effect spectroscopy, with one particular study by Hyun *et al.* finding a heavily damped 3 THz oscillation [33]. They did not comment any further on this behavior. Furthermore, Cattaneo *et al.* observed the ultrafast off-resonant Raman excitation of THz oscillations from all optical pump probe measurements, similar to optical Kerr effect geometries, in

which the probe is encoding a bulk phase shift and transmission imposed by the excited sample [34].

Finally, with new coherent THz sources available, extensive THz-TDS studies were performed on various LC compounds by Vieweg *et al.* They were able to determine the macroscopic refractive indices and absorption coefficients for various nCB materials [35] and other LCs [36–38] up to 2.5 THz. And from a microscopic perspective they were able to extract from this data the order parameter S and the polarizabilities on a molecular level [39, 40]. Later, using ultra-broadband THz generation, they extended their investigations to the high THz frequencies, and compared for the first time with molecular level DFT calculations, showing a good match at high frequencies, and defining a cutoff frequency analogous to glassy systems at 1 THz, separating a disordered response from molecular vibrations [41, 42].

In this work, the idea is to focus in detail on the nature of the intermolecular collective dynamics on the one hand, and the intramolecular vibrations on the other hand, and the crossover between both regimes. From an experimental perspective, macroscopic and microscopic properties will be compared in terms of their impact on the measurement. On the macroscopic scale, changing the LC phase corresponds to tuning the collective order of the molecular environment. On the microscopic scale, three closely related molecular species are compared. They differ from each other only by specific functional groups, which allows to isolate the impact of the molecular composition.

Both linear and nonlinear THz experiments are part of this work. Firstly, linear THz Time Domain Spectroscopy (TDS) is performed, revealing the THz refractive indices and absorption coefficients. Secondly, THz induced transient birefringence measurements are conducted, where the THz takes part as a resonant pump, driving the THz dynamics coherently. The broad outlook to this work lies in the assessment whether LC material functionalities can be modified when these intermolecular modes are driven strongly and resonantly.

This thesis is structured to introduce the main concepts before presenting the results. **Chapter 2** introduces the LC samples under investigation in detail, with a focus on the molecular properties, the mesophases, and alignment techniques used in pursuit of sample control. **Chapter 3** then discusses the THz techniques used to investigate the sample. First the methods for generation and detection of pulsed THz radiation are discussed, before introducing the setup and the intended measurements. The following **Chapter 4** then discusses the sample delivery for providing aligned LCs into the interaction region in the aforementioned setup. **Chapter 5** discusses the spectroscopic results. Finally, **Chapter 6** provides concluding remarks and an outlook.

2. Liquid crystals

Since their discovery in 1888 by Friedrich Reinitzer [43], liquid crystals (LCs) have been an extensively investigated phase of matter, and have become one of the pillars of the soft matter world [1, 2, 44]. They have found numerous applications in science and technology, due to their electro-optical properties and tunability. These macroscopic properties emerge from the microscopic geometries on a molecular level. The realm of molecules and their connected mesophases is wide, and keeps producing new discoveries, such as ferroelectric nematic LC phases, which have been postulated over 100 years ago, but discovered in nature only recently [45]. It is this interplay between macroscopic bulk phase appearance and molecular collective interactions that form the backbone of the studies presented within this work.

This chapter will lay the foundation for the rest of this thesis, by introducing the common concepts relevant to LC materials here. Furthermore, the samples of choice will be presented including the motivation for their selection. As already stated, the LC set of options is wide ranging and full of exotic behavior. But here, the most commonly known molecular species act as benchmark systems, bridging the gap between the Liquid Crystal and THz communities.

2.1. Macroscopic appearance

The macroscopic appearance and behavior in the LC mesophase is closely linked to the geometries on the molecular level. On the lowest level, LCs can be described as fluids that possess anisotropic properties across a number of possible observables, such as in their flow characteristics [46], their interaction with light [47–50], and their ability to allow for charge transport [51]. All these characteristics on macroscopic scales are fundamentally emerging from the strongly anisotropic molecular constituents of the LC.

The second factor governing the emergence of collective order is of macroscopic nature. Essentially, it influences how the forces driving the molecules together are balanced against the forces counteracting this tendency. Broadly, LCs are categorized in two classes. Thermotropic LCs undergo phase transitions as a function of temperature. On the other hand, the lyotropic class of LCs shows macroscopic order as function predominantly of concentration of amphiphilic molecules in a solvent, forming supramolecular structures [52]. Soap is a commonly found example of such systems [53, 54]. Here, the focus is solely on thermotropic systems, since the direct next neighbor interactions between molecules are the subject of interest.

In the context of thermotropic LCs, the most common cases are [2]:

- elongated rod-shaped molecules that support LC phases in which all molecules are

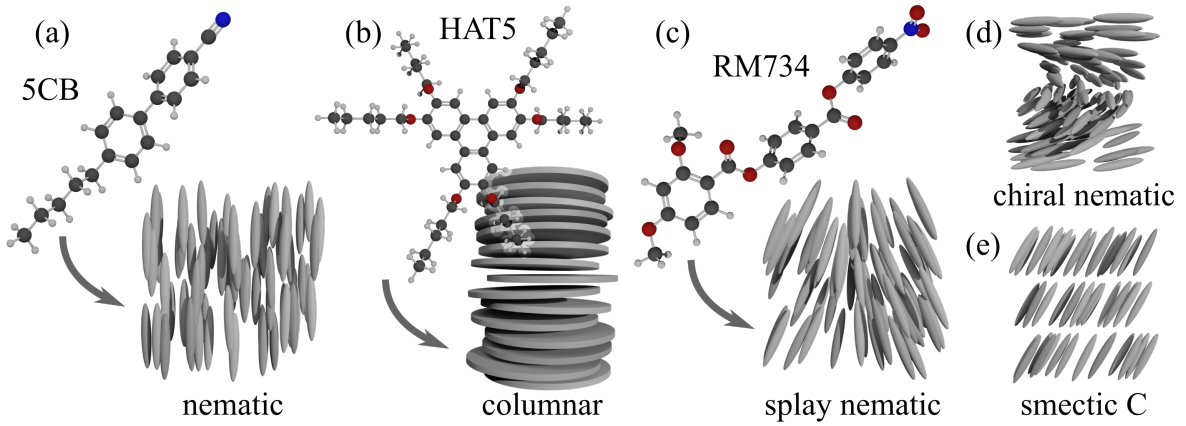

Figure 2.1.: Examples of known molecules showing LC behavior: (a) the rod shaped 5CB molecules packs in the nematic phase, (b) the disc shaped HAT5 molecules arrange in a column, (c) the wedge shaped RM734 molecule forms the splay nematic alignment (in fact, together with its large dipole moment, it is an example of a ferroelectric LC state) Without Examples: (d) chiral nematic, and (e) smectic C arrangements.

oriented along a common axis called director.

- disk-shaped molecules, extended in two dimensions, often with a degree of rotational symmetry, that preferentially stack in columns.
- chiral (cholecteric) molecules, that align just like the rod-shaped molecules, but add a twist of certain pitch to the alignment axis.

Figure 2.1 presents examples of molecules and representative molecular arrangements schematically. Here, all further work is exclusively focused on the rod-like molecules and their most common LC phases. These thermotropic systems are exclusively investigated in mono-molecular composition. Mixtures (typical in industry applications, where desired LC properties are designed) or solutions are not considered. Between the well known isotropic liquid and the crystalline solid phase, the nematic and smectic A phases appear as temperature is lowered through first-order phase transitions. Figure 2.2 presents a typical sequence of phase transitions from crystalline to smectic A, nematic, and finally to isotropic phase, in which the molecules are randomly oriented as in an ideal liquid.

2.1.1. Nematics

The simplest arrangement that rod-shaped molecules can form is expressed as the *nematic* phase, in which all molecules retain their ability to flow in all three space dimensions, but point along a common axis. This means, collectively they show no positional order, as in an ideal fluid, but have a degree of orientational order in one dimension. The common alignment axis is typically called *director* and is expressed as a unit vector

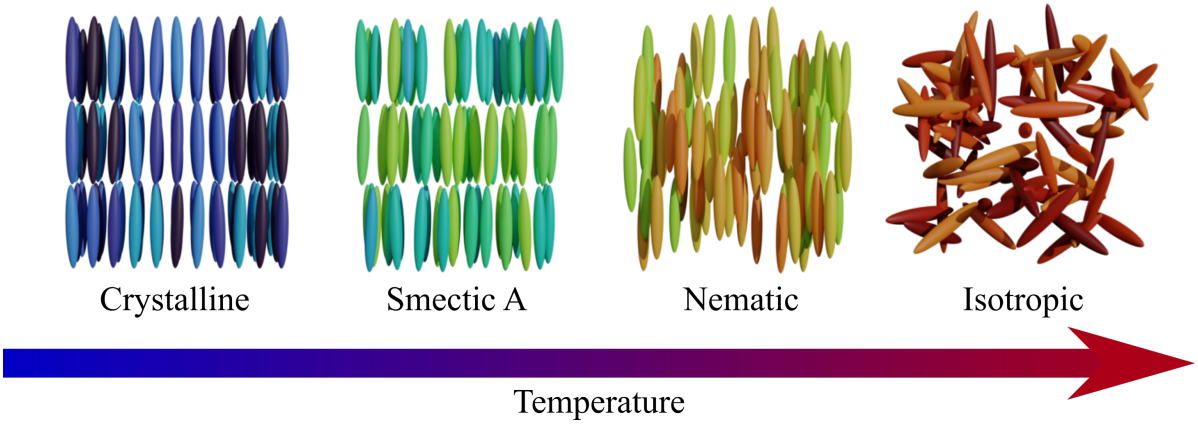

Figure 2.2.: Sketches of the two LC phases of interest in this work, nematic and smectic A, between the crystalline and liquid phases in which the molecules are depicted as rods. The color is visualizing the increase in temperature.

n. It is a macroscopic property expressing the pointing average of all molecules within a volume element. If the alignment is not actively controlled, it can vary in space, which gives rise to Schlieren textures (slowly varying director orientation in space, visible in microscopy), or even point or line defects (called disclination lines), where the director is undefined. This can happen when the director approaching this point from different directions is forced to make a discontinuous jump. LC defects and their associated topology is a rich field, that allows the study of other topological systems through analogy [55]. Figure 2.3a shows a typical nematic Schlieren texture under polarized light optical microscopy (POM, described in section 4.2.1) when no alignment is imposed, and panel c shows a homogeneously planar aligned nematic, in which the molecules form one orientational mono-domain.

The alignment with the director is not perfect and the molecules are driven out of this ideal alignment by thermal fluctuations. This misalignment of the individual molecules from their collective average axis is captured by the so called order parameter S accompanying the director n at every point in the material volume. For a given angle θ between molecular orientation and director, the scalar order parameter S is the average over the volume element of $P_2(\theta)$ and is given by equation 2.1.

$$S = \left\langle \frac{3\cos^2\theta - 1}{2} \right\rangle \tag{2.1}$$

It takes values between 0 and 1, with 0 indicating total rotational disorder and 1 indicating perfect alignment with n (the case of perfect alignment perpendicular to n would give -0.5). Typical values for nematics are in the range of 0.6 [39].

2.1.2. Smectic LCs

Smectic LC phases posses similar orienatational character as the nematic phase, in that the molecules point along a common axis. In terms of positional order, the molecules

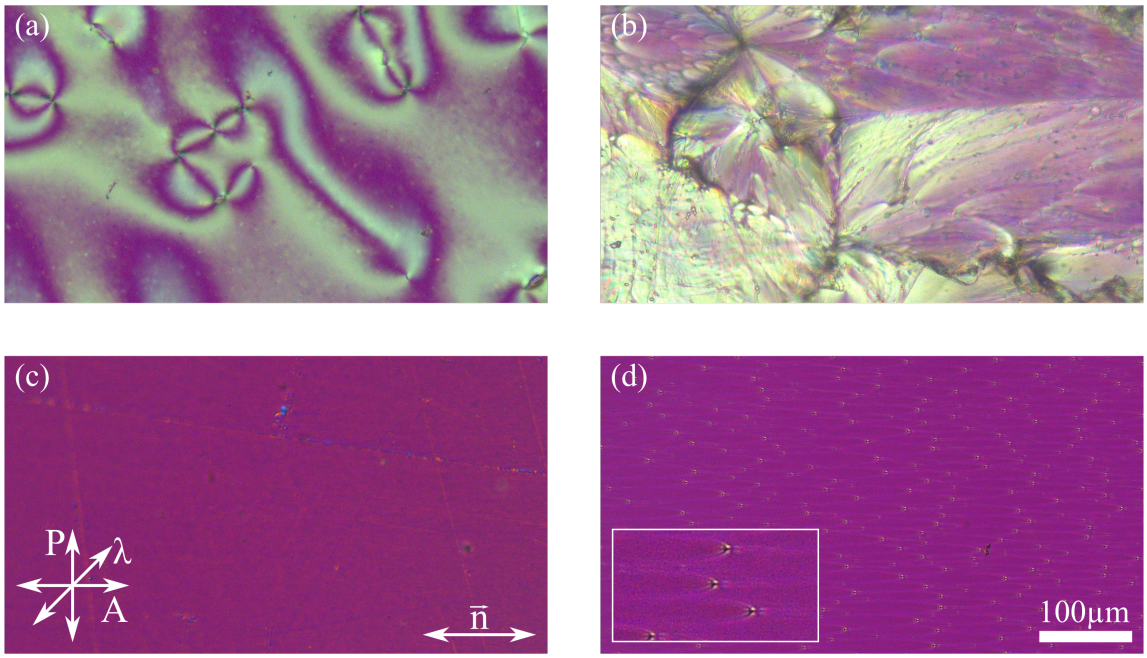

Figure 2.3.: Polarized light microscopy images for (a) an unaligned nematic system, (b) an unaligned smectic A system, (c) an aligned nematic system, and (d) an aligned smectic A system, with the inset focusing onto the conical defects. The arrows in the lower left corner assign the polarizer, analyzer and lambda plate axes for all panels. The scale in the lower right corner applies to all panels. See section 4.2.1 for the measurement principle. $\vec{n}$ represents the LC alignment director for panel c and d.

within a smectic phase are not free to translate in all three space directions. Instead, in the simplest imaginable smectic phase (smectic A) the molecules show stacking behavior along the director axis, but no positional order within each layer. It could be imagined as a stack of two dimensional fluids. In LCs that show both nematic and smectic phases, the smectic phase is typically found at lower temperatures than the nematic phase. As a general trend, lower temperature phases show higher degrees of molecular order. While this smectic A configuration is the one relevant for this work, the next paragraph will provide examples of other, more complex, smectic phases.

The smectic B phase shows the same stacking behavior of molecules as in smectic A, with the addition of loose hexagonal packing within each layer. Smectic C is again similar to smectic A, with a tilt of the director within each layer, meaning the stacking axis and director vector are no longer parallel. Smectic C* has an alternating tilt from layer to layer in a chevron pattern. Beyond these examples, even more exotic phases exist just within the family of smectic alignments.

The smectic layering leads to different defect types that accommodate the molecular arrangement under external stress. Focal conic defects form because of strain relaxation reasons, in which the different elastic tensors (splay, twist, bend) maintain the layered structure [56]. Figure 2.3b shows a smectic A sample without imposed alignment, and

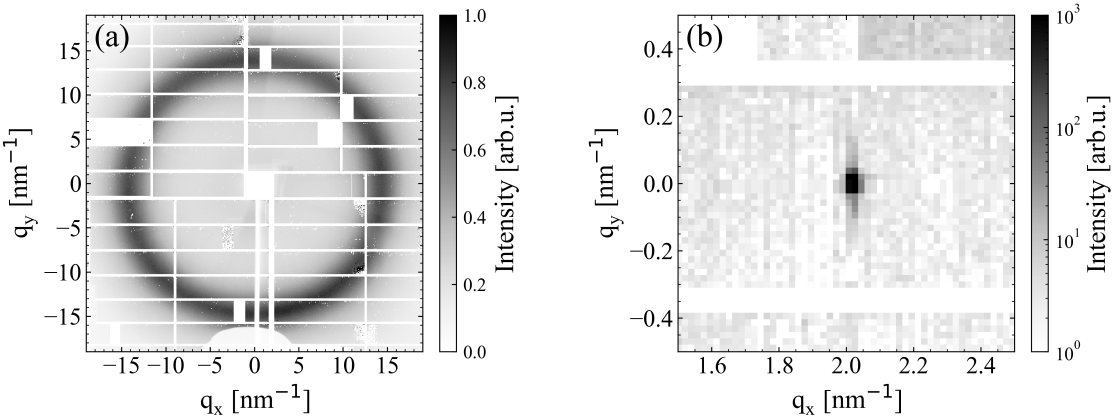

Figure 2.4.: The order of a smectic A phase 8CB sample probed by X-ray diffraction. (a) Transmission geometry, normal to the layers, revealing the interlayer liquid like structure through the diffusive ring. (b) Bragg condition to the layer spacing, revealing the ordered nature through the sharp Bragg peak. The ring radius is determined by the intermolecular correlation length, and the Bragg spot position by the layer spacing.

panel d shows a homogeneously planar (from left to right) aligned smectic A cell, with a zoom in onto the focal conic defects in the inset.

These combinations of positional and orientational order manifest in different ways. One of the most interesting consequences is their diffraction behavior. Taking the smectic A phase as an example, depending on the orientation of the LC to the incoming radiation, it can diffract X-ray diffusively as expected from a liquid, or in the form of a sharp Bragg peak as from the layers of a lattice. Figure 2.4 shows these two cases measured in hard X-ray diffraction experiments at the FXE beamline at the EuXFEL facility. In panel a, a freely suspended 8CB (introduced in detail in the next section 2.2) film is exposed to 8.9 keV photons with its director pointing along the beam propagation direction. The photons are sensitive to the arrangement within each layer, and are diffracted by a phase grating of average grating constant given by the intermolecular distances in the plane of each layer, leading to a symmetric diffraction ring. The width is related to the intermolecular correlation, or the distribution of distances. Panel b, on the other hand, is recorded with the sample exposed in grazing incidence. For this purpose, a thin layer was deposited on a functionalized surface (see sections 2.4 and 4.2.3), imposing alignment with the director pointing normal to the surface plane. In Bragg condition, meaning the scattered photons from each layer interfere constructively, a sharp peak is formed according to the layer spacing. This duality of behaviors, typically found in liquids or solids, justifies why the term liquid crystal was established in the first place.

In the smectic samples under investigation here, one notable aspect is that the layer spacing is not equal to the length of the molecular long axis. Specifically talking for one of the candidates under investigation 8CB, with 3.1 nm it is 1.55 times larger than the molecule alone [57, 58], which corresponds to the size of the 8CB dimer. This points to one more aspect regarding the intermolecular forces. On top of the expected van-

der-Waals forces, also dimerization takes place through dipole-dipole interaction (see section 2.2).

2.1.3. Thermodynamic origin of the LC phases

Phenomenologically, the appearance of the LC phase can be described in terms of thermodynamic properties. The Landau-de Gennes description is able to capture the behavior in terms of the order parameter tensor of the system in a free energy minimization process. The global minimum of such a system is a uniform director field. It is possible to add temperature dependence into the solution, and the Landau-de Gennes theory is successful in this context in describing the behavior of LC systems across the nematic-isotropic phase transition, for example predicting the discontinuous nature of the transition [1, 2, 55].

Taking into account strains to the system in the form of bend, splay, and twist distortions, the elastic free energy can be treated in the Frank-Oseen formalism and is expressed in terms of n (with the choice that the unperturbed director is pointing along the z axis) in the form

$$F_{\text{elastic}} = \frac{1}{2}k_{11}(\nabla \cdot n)^2 + \frac{1}{2}k_{22}(n \cdot (\nabla \times n))^2 + \frac{1}{2}k_{33}(n \times (\nabla \times n))^2 \tag{2.2}$$

The term $\nabla \cdot n = \frac{\partial n_x}{\partial x} + \frac{\partial n_y}{\partial y}$ describes the splay distortion of the nematic field with its strength k_{11}. The twits is given by $n \cdot (\nabla \times n) = \frac{\partial n_x}{\partial y} + \frac{\partial n_y}{\partial x}$ with its strength k_{22}. And finally the bend of the director field is described by $(n \times (\nabla \times n))^2 = (\frac{\partial n_x}{\partial z})^2 + (\frac{\partial n_y}{\partial z})^2$ and amplitude k_{33}. It is a common choice to set $k_{11} = k_{22} = k_{33} = k$, given that these constants are of the same order of magnitude in real systems, leading to the elastic free energy description of

$$F_{\text{elastic}} = \frac{1}{2}k[(\nabla \cdot n)^2 + (\nabla \times n)^2] \tag{2.3}$$

The minimization of this free energy leads to the director field within the volume. Additional terms can be added to the free energy, in order to account for more complex systems. Examples are external fields, surface anchoring, or suspended objects/particles within the LC. In all these cases, the director field will realign, in order to accommodate these extra terms.

2.2. Molecular candidates

The molecules selected here represent well known benchmark systems from the perspective of the LC community. The macroscopic (phase transitions, refractive indices, elastic constants,...) and microscopic (molecular dipole moments, polarizabilities,...) properties are reported in literature. Therefore these molecules are reasonable starting points for bridge building into the THz molecular dynamics field. From a more fundamental

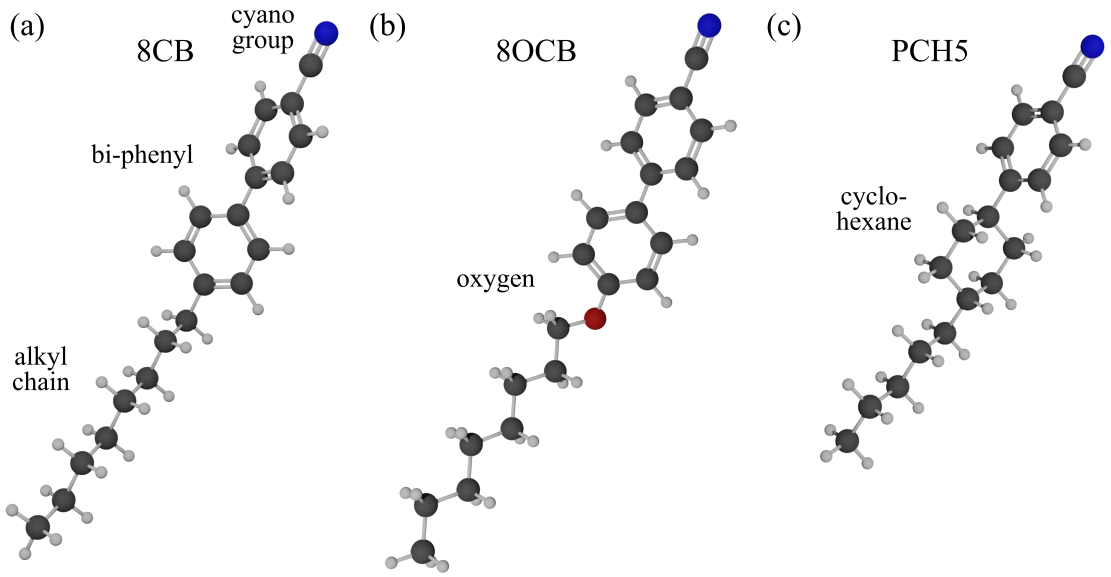

Figure 2.5.: The molecular structures of (a) 8CB, (b) 8OCB, and (c) PCH5. 8CB consists of a biphenyl core with attached cyano group and alkyl chain of eight carbon atoms length. 8OCB contains an additional oxygen atom between biphenyl and alkyl chain. PCH5 has one phenyl ring exchanged for a flexible cyclohexane group, and an alkyl chain of length five.

perspective, the choice of molecules is also guided by experimental considerations. The three main targets are shown in Figure 2.5 and receive a detailed discussion. It can be seen at a glance, that the three molecules are closely related to each other. This resemblance of the chosen molecules is by design. The idea is to use the structural similarities as a comparison point between measurements, and to identify how small changes to the molecular composition impact on the results. This is intended to help in gaining insight into the dynamics, from a purely experimental perspective before theoretical support.

2.2.1. nCB family of LCs

From the nCB (4-cyano-4′-n-alkylbiphenyl) family of LCs, the sample of highest interest is 8CB, which is shown in Figure 2.5a. It consists of a biphenyl group (”B”), with a cyano group attached on one end (”C”), and an alkyl chain of eight carbon atoms length (”8”) attached at the other end. The chain can vary in length n, and each of these distinct molecules has its own phase transition properties. Figure 2.6a shows the phase sequences of the nCB series between two and twelve. 5CB is the first molecule in the series that shows liquid crystal behavior, and is generally regarded as the benchmark molecule for LCs. The choice for 8CB, on the other hand, is made because it is the first to also shows the smectic A phase. This will allow to tune the collective order in more steps in the experiments. For all nCB samples, the phase transitions occur in an easily

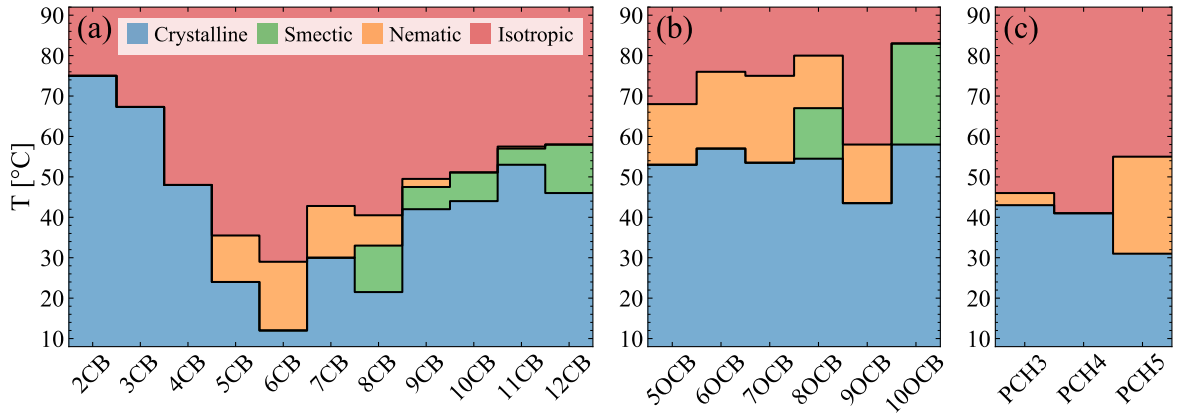

Figure 2.6.: Phase diagrams showing the phase transition temperatures as function of alkyl chain length for families of (a) nCB, (b) nOCB, and (c) PCHn. Data taken from the vendor Synthon Chemicals [62].

accessible temperature range.

From a molecular dynamics perspective, the nCBs possess a large reported permanent dipole moment of 4.9D [59] (exp.) to 6.2D [60, 61] (theo., gas phase DFT), generated mostly by the polar cyano group and remains reasonable constant with the alkyl chain length. The consequence are dipole-dipole interactions between neighboring molecules, leading to loosely bound anti-parallel dimers, as hinted at above. The biphenyl is rigid and makes up the backbone of the LC unit, with a torsional angle between the two phenyl rings. Electronically speaking, it is characterized by delocalized π orbitals that show high degrees of polarizability and allow of π-stacking in principle (favoring charge transport). On the other hand, the non-planar nature of the two rings counteracts this tendency. In contrast to the rigid core, the alkyl chain is highly flexible and able to adapt to the environment.

2.2.2. nOCB family of LCs

8OCB (4-(4′-n-octyloxyphenyl)benzonitrile) is structurally highly similar to 8CB, with the only change being an inserted oxygen molecule between biphenyl core and alkyl chain. Parallel to the nCB section, Figure 2.5b shows the 8OCB structure and Figure 2.6b shows the phase transitions as function for various chain lengths in the nOCB series. The added oxygen is primarily responsible for raising the phase temperatures on a macroscopic level, and for raising the permanent dipole moment on a microscopic level to 7.3D [63] (theo., gas phase DFT). Just as for 8CB, 8OCB is the first in its series to show both the nematic and smectic phases. Additionally it makes the direct comparison easier, since the chain lengths are equal between them.

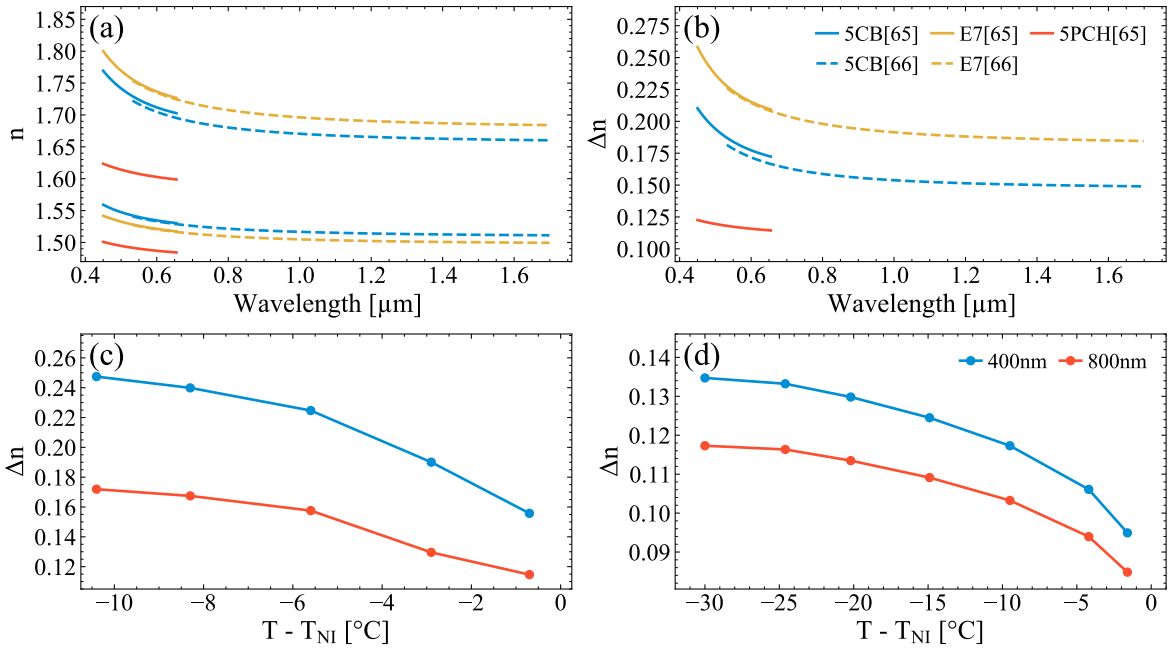

Figure 2.7.: Refractive indices and birefringence values for select LC samples, as reported in [64–66]. (a) Refractive indices for 5CB (blue), PCH5 (red), and E7 (multi-molecular mixture, yellow) across the visible and NIR electromagnetic spectrum, and (b) the resulting birefringence. Furthermore, the birefingence is plotted as function of temperature difference to the nematic-isotropic phase transition T_{NI} for (c) 5CB and (d) PCH5.

2.2.3. PCHn family of LCs

Finally, PCH5 (trans-4-(4′-n-pentylcyclohexyl)benzonitrile) is the third molecule considered for the experiments, as presented in Figure 2.5c, and the related phase transitions in Figure 2.6c. PCH5 is similar to 5CB, except for the exchange of one phenyl-ring (at the alkyl chain end) for a cyclo-hexane group. This group is highly flexible and can be more seen as an extension of the alkyl chain than a modification of the ring itself. Electronically speaking, it does not have the delocalized character of a phenyl ring, and therefore no ability to π-stack, and a similar electronic polarizability, with roughly 40 $Å^3$ for PCH5 [40] compared to about 45 $Å^3$ for 5CB [39] and 5OCB [40].

2.3. Optical properties

The highly anisotropic nature of the LC materials translates to anisotropy of bulk properties, such as in their interactions with light. In its simplest description nematics can be described as uni-axial crystals, with their optic axis equal to the director. Then the refractive index along the director corresponds to the extraordinary axis n_e, and the refractive index perpendicular corresponds to the ordinary axis n_o. Hence, LC are

birefringent materials, which is a property that makes them highly interesting for technological applications. Together with their response to external stimuli, discussed in the next section 2.4, they are able to act as tunable phase shifters. Figure 2.7a and b give representative examples of refractive indices and birefringence values for common LC samples. The average (isotropic) refractive index for rod-shaped molecules can be expressed as $\bar{n}^2 = \frac{1}{3}n_e^2 + \frac{2}{3}n_o^2$. Furthermore, their technological usefulness is enhanced by the fact that they are typically transparent over the entire visible and large parts of the NIR spectrum.

Within the LC phases the birefringence is highly sensitive to temperature. As the system approaches the phase transition to the isotropic state, the birefringence drops dramatically. This is an expression of the thermal energy in the system, competing with the forces that drive the molecules into collective alignment. Ultimately, the birefringence is tied to the order parameter S, which is sensitive to temperature. Figure 2.7c and d show this effect on the examples of 5CB and PCH5, respectively.

2.4. Response to external stimuli

In addition to these intrinsic properties of LC materials, another heavily exploited property in application is the easy tunability of the material through response to external stimuli. The two most well known cases, which are both used in liquid crystal display (LCD) applications, are the alignment by application of external electric fields, and the alignment by imposition of boundary conditions. Both effects will be used for sample delivery in the experiments performed in this work, and therefore get dedicated discussions here [1, 2, 55].

2.4.1. Electric fields

The anisotropic nature of LCs is also expressed in their dielectric properties. The susceptibility and polarizability are a reflection of the molecular anisotropic nature and strong permanent dipole moment. This interaction of the material with the external influence can be expressed in the context of the free energy of equation 2.3 through the dielectric coupling.

$$F_{\text{diel.}} = -\frac{1}{4\pi}\int DdE = -\frac{\epsilon_\perp}{8\pi}E^2 - \frac{(\epsilon_\parallel - \epsilon_\perp)}{8\pi}(n \cdot E)^2 \tag{2.4}$$

with the dielectric displacement D, and the dielectric permittivity ϵ parallel and perpendicular to the director. In practice, only the second term generates realignment through it's coupling between n and E, and it can be added to the elastic free energy in equation 2.3.

Over a certain threshold field strength, the alignment along the field vectors becomes energetically favorable, and the director experiences a torque. This effect is termed Fréederickz transition. For the example case of an LC confined between two windows

with planar alignment, and the switching on of an electric field across the cell gap d, one finds threshold fields E_T in the form

$$E_T = \frac{\pi}{d}\sqrt{\frac{k_{22}}{\epsilon_\parallel - \epsilon_\perp}} \tag{2.5}$$

Typically, the voltage is applied in the form of high frequency AC fields, because in the DC case ionic impurities migrate to the electrodes, leading to a current and eventual heating of the sample across phase transitions. The high frequency (beyond 100 Hz) ensures that the material experiences an effective constant field on reorientational time scales.

2.4.2. Boundary effects

The molecular next-neighbor interactions can force alignment on scales spanning macroscopic distances, easily up to millimeter domain sizes. These interactions can be exploited to induce a mono-domain of orientation in the LC sample, by imposition of alignment at the surfaces. In the framework of the Landau-de Gennes description, it is expressed by addition of an interaction term. It contains an alignment axis e for the surface (called the easy axis), and a coupling energy W which parameterizes the strength of the alignment. Integration over the surface S leads to additional free energy in equation 2.3 of the form

$$F_{\text{Surface}} = -\frac{1}{2}W\int (n \cdot e)^2 dS \tag{2.6}$$

When the total free energy is minimized, the surface free energy leads to alignment throughout the bulk.

Experimentally, this is achieved through surface functunalization. Boundary conditions can be imposed by micro-grooved surfaces, leading to planar alignment along the groves. Typically this is achieved through application of thin polymer layers (such as poly vinyl alcohol (PVA)), that are then rubbed with a fine cloth. Alternatively, chemical interactions can lead to certain alignments. For example, deposition of a thin layer of molecules with certain functional groups can interact with the polar heads of the LC molecules (or other parts of them), imposing perpendicular (homeotropic) anchoring.

Alignment techniques can also be combined. As it happens, most LCDs rely on both surface and field effects. An LC layer placed between two cross polarizers can block any light from passing the assembly in the condition of zero applied electric field, if the surface anchored alignment direction is not turning the polarization. Switching on a voltage in order to turn the molecules out of this initial configuration can then lead to light leakage through the second polarizer. Indium Tin Oxide (ITO) is a common substrate that is both conductive and transparant in the visible spectrum.

3. THz methods

The range that comprises the THz electromagnetic spectrum represents one of the two extreme ends of it. Opposite to the X-ray range, it is characterized by long wavelengths and photon energies that are comparable to thermal energy at room temperature. Formally, THz radiation is defined by the frequency range of 0.3 THz to 10 THz, corresponding to 1000 µm to 30 µm in wavelength, or 1 meV to 40 meV in photon energy. Efficient and coherent THz sources rely on nonlinear optical processes for generation (or cryogenic operation, as is the case for quantum cascade lasers QCLs).

THz radiation has the advantage of long wavelengths over all other spectral regions, from the mid-IR to the extreme ultraviolet, allowing the sampling and resolution of the full coherent electric field waveform. Therefore, it gives direct access to both amplitude and phase of the THz light. While there has been work done to extend this advantage to higher frequencies [67], typically in these conventional regions only intensities are directly measurable, loosing any absolute phase information.

THz science is a mature field [68–73], with methods for generation and detection that are numerous and can be picked to suit the given experimental goals. The same is true for the manipulation of THz light through optical elements. In the following, a general overview will present the techniques with their advantages and disadvantages, in order to motivate the choices made for the particular investigation of this work. These techniques will then be discussed in more detail. Lastly, the experimental setup, and the two THz measurements performed with this setup will be introduced.

3.1. THz generation, detection, and manipulation

The coherent generation and detection of the THz pulses that interact with the sample is the foundation for this work. This section is intended to provide all details necessary to understand the chosen experimental conditions.

3.1.1. THz generation

Most coherent generation mechanisms for THz radiation rely on the employment of ultrafast optics, since purely electronic techniques are too slow and don't reach THz frequencies. There are numerous ways to generate THz radiation, such as photo conductive antennas, which have become the work horse within this field, given their cost effectiveness [74]. Here, the radiating electric field is generated by a photo current in a biased semiconductor with sufficiently short carrier lifetimes. Other options are quantum cascade lasers (QCLs) [75] two color air plasma sources [76, 77], spintronic

emitters [78], difference frequency generation (DFG) techniques [79, 80] or quasi-phase matched crystals (such as periodically poled lithium niobate PPLN) [81] for narrow band THz generation, and linear accelerator facility based sources like FELIX (Nijmegen, the Netherlands) [82] and FELBE (Dresden, Germany) [83, 84].

The following discussion will focus on the optical rectification (OR) technique [85, 86] chosen for this work, for its good compromise between high THz field strength and broadband THz spectrum achievable for tabletop sources. Transmission spectroscopy experiments benefit from an extended spectral bandwidth, while nonlinear experiments require high intensities. OR can provide a means to both. In particular, the discussion begins with a general description of the optical rectification process, followed by the particular implementation in this work.

3.1.1.1. Optical rectification

The optical rectification process originates from nonlinearities in the dielectric response of a material, where the induced polarization of the medium deviates from a purely linear proportionality with the incident electric field. In this sense, it belongs to the same class of processes as second harmonic generation (SHG), and other wave mixing processes [73, 87].

It's typical for these materials to have small nonlinearities and to behave effectively linear for small electric fields. Hence, they reveal their nonlinear nature once the field strength compares with the internal interatomic fields. This relation between the polarization density $P(t)$ and the incident electric field $E(t)$ is represented by a Taylor expansion of the form presented in equation 3.1 with the (non-) linear susceptibilities $\chi^{(n)}$.

$$P(t) = \epsilon_0(\chi E(t) + \chi^{(2)}E^2(t) + \chi^{(3)}E^3(t) + ...) \tag{3.1}$$

The higher order terms are responsible for generating wave mixing processes and frequency conversion. The exact details about which processes are dominant depend on the materials and symmetries used. Finally, the connection between the time-varying polarization density and the generated propagating electric fields is given in a classical description by Maxwell's Equations and the wave equation 3.2.

$$\nabla^2 E(t) - \frac{n^2}{c^2}\frac{d^2E(t)}{dt^2} = \mu_0 \frac{d^2P(t)}{dt^2} \tag{3.2}$$

Hence, in the far field the radiated electric field is proportional to the second derivative of the induced polarization in the nonlinear medium. From here, the question remains how these wave mixing processes lead to coherent THz radiation in practice. Looking at the second order polarization term $P^{(2)}(t) = \chi^{(2)}E^2(t)$ in equation 3.1, and considering a two color light field $E(t) = E_1\cos(\omega_1 t) + E_2\cos(\omega_2 t)$ for simplicity, one finds terms oscillating with different frequencies. Among them are terms that represent second harmonic

generation $\propto \cos(2\omega_i t)$ (SHG), sum frequency generation $\propto \cos((\omega_1 + \omega_2)t)$ (SFG), difference frequency generation $\propto \cos((\omega_1 - \omega_2)t)$ (DFG), and DC terms $\propto \cos((\omega_i - \omega_i)t)$ that are called the optically rectified terms (OR).

In the continuous wave (cw) case, the rectified term is naturally neglected, since DC polarization does not radiate. Only in pulsed applications is it of use. In these cases, the rectified term follows the pulse envelope, leading to a time varying polarization density that radiates pulses with frequency bandwidth proportional to the inverse of the driving pulse time duration. From the frequency perspective, optical rectification can be understood as an intrapulse difference frequency process, but this formulation will not be further discussed here.

As is the case for any medium, the conversion mechanism alone is not a sufficient description of its performance. In practice phase matching considerations are important [88,89] and dictate if a $\chi^{(2)}$ material is suitable for Second Harmonic Generation or Optical Rectification. Common inorganic materials that are well phase matched at easily available pump wavelengths are Lithium Niobate ($LiNbO_3$, LN) and Zinc Telluride (ZnTe). While they deliver wider bandwidth than photoconductive antennas, the improvement is modest, and in the case of LN phase matching requires complicated tilted wave front techniques. Therefore a number of organic crystals have emerged as options. Across the board they have approximately one order of magnitude higher conversion efficiencies than their inorganic counterparts, and even larger bandwidths. The downside is their lower damage threshold and required thermal management, and substantially increased commercial cost.

3.1.2. THz detection

What makes the THz regime unique, are wavelengths that can be fully resolved. The retrieved waveforms correspond to the electric fields of the light, hence they make amplitude and phase accessible at the same time. Typical all-optical techniques use geometries in which the THz beam is overlapped with an ultrashort gate pulse that encodes the instantaneous electric field value as a function of its relative position in time. The two most common techniques are based on photoconducitve antennas [90] and Pockels crystals, and both represent in some sense the reverse effect as used for THz generation. In photo-conductive antennas a total current (carrier lifetime must be much shorter than a THz cycle) is measured with the THz acting as a bias field. Alternatively, in EOS, the THz acts as an instantaneous applied voltage over a Pockels crystal, imprinting a change in polarization onto the gate pulse. The following section will describe this second technique in more detail, since it is of relevance in this work.

3.1.2.1. Electro optic sampling

The typical scheme to measure THz traces via electro-optic sampling (EOS) [91,92] involves a co-propagating ultrashort gate pulse through an electro-optic material, followed by a quarter-wave plate, a Wollaston prism, and two balanced photo-diodes detecting

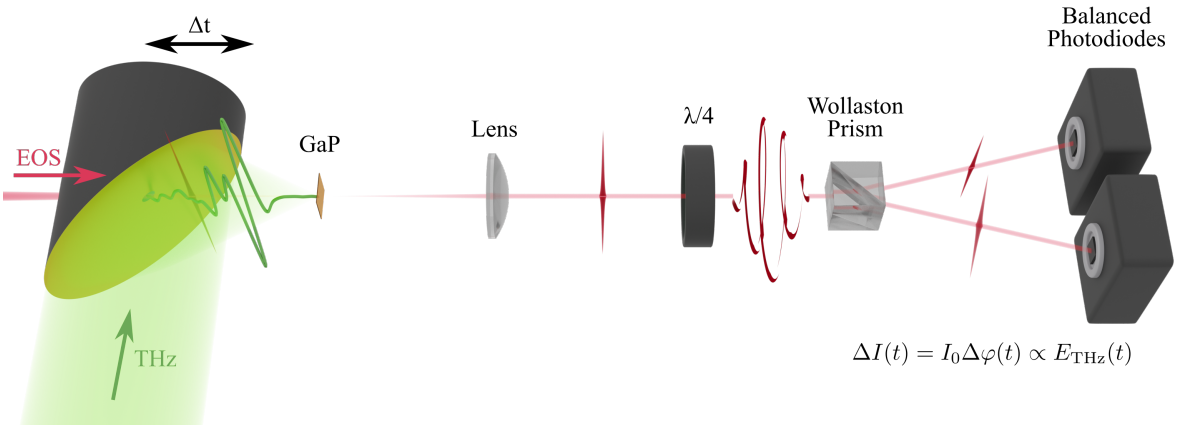

Figure 3.1.: Electro-optic sampling scheme. The linearly polarized THz and probe pulses are focused through a common focus in the Pockels crystal (GaP) with variable time delay. Afterwards, the probe is collimated by a lens, converted to circular polarization by a quarter waveplate, and split into s- and p-polarization by a Wollaston prism. In the absence of electric field applied to the crystal, both arms contain the same light intensity. THz electric fields add additional phase to the probe polarization, leading to an intensity difference between the final beams.

both outputs. The scheme is based on the Pockels effect in electro-optic crystals, in which the refractive index is modified as function of the electric field strength present.

The Pockels effect [73, 93, 94] is a linear electro-optic response of materials and can be discussed in the framework of anisotropic changes of the index ellipsoid in the presence of electric fields. In the most general case, it can be expressed through the impermeability tensor η_{ij} as

$$\sum_{ij} \eta_{ij} x_i x_j = 1 \tag{3.3}$$

For the case that the ellipsoid axes match the principle axes, it simplifies to the known form $x_1^2/n_1^2 + x_2^2/n_2^2 + x_3^2/n_3^2 = 1$. The change of the impermeability tensor with applied electric field $\eta_{ij}(E)$ can be expanded in a Taylor series, and the first order term is related to the linear change in refractive index $\Delta n(E)$

$$\eta_{ij}(E) = \eta_{ij} + \sum_k r_{ijk} E_k + ... \tag{3.4}$$

where the r_{ijk} coefficients are the electro-optic coefficients characterizing the strength of the response. This tensor in principle has 27 elements, but can be simplified, since it is symmetric by nature. Furthermore, not all elements are independent, with the exact form being dictated by the crystal point group of the material. For cubic $\bar{4}3m$ crystals, such as the GaP and ZnTe crystals used in this work, the electro-optic tensor simplifies

down to

$$r_{Ik} = \begin{bmatrix} 0 & 0 & 0 \\ 0 & 0 & 0 \\ 0 & 0 & 0 \\ r_{41} & 0 & 0 \\ 0 & r_{41} & 0 \\ 0 & 0 & r_{41} \end{bmatrix} \tag{3.5}$$

The crystals used in this work are optically isotropic $n_1 = n_2 = n_3 = n_0$. This leaves the electric field modified index ellipsoid equation in the form

$$\frac{x^2}{n_0^2} + \frac{y^2}{n_0^2} + \frac{z^2}{n_0^2} + 2r_{41}E_x yz + 2r_{41}E_y xz + 2r_{41}E_z xy = 1 \tag{3.6}$$

In order to simplify the response, EOS is typically performed with crystal cuts along the [110] crystallographic plane, and the pulses propagate perpendicular to it. In order to solve this case, a coordinate transform is performed into this new reference frame via

$$X = \frac{1}{\sqrt{2}} \begin{pmatrix} -1 \\ 1 \\ 0 \end{pmatrix}, Y = \begin{pmatrix} 0 \\ 0 \\ 1 \end{pmatrix}, Z = \frac{1}{\sqrt{2}} \begin{pmatrix} -1 \\ -1 \\ 0 \end{pmatrix} \tag{3.7}$$

$$x = -\frac{X+Z}{\sqrt{2}}, x = \frac{X-Z}{\sqrt{2}}, z = Y \tag{3.8}$$

Assuming the applied THz electric field is polarized along the new x axis, the ellipsoid equation simplifies to

$$\frac{X^2}{n_0^2} + \frac{Y^2}{n_0^2} + \frac{Z^2}{n_0^2} - r_{41}E_{\mathrm{THz}}XY = 1 \tag{3.9}$$

In order to bring this equation into a form that allows for easy identification of the induced refractive indices, the new axes A and B are defined

$$A = -\frac{X+Y}{\sqrt{2}}, x = \frac{Y-X}{\sqrt{2}} \tag{3.10}$$

$$\frac{Z^2}{n_0^2} + \frac{A^2}{n_0^2} + \frac{B^2}{n_0^2} - r_{41}E_{\mathrm{THz}}(B^2 - A^2) = 1 \tag{3.11}$$

which represent axes 45° diagonal to the axes defining the plane of polarization. For the condition $r_{41}E_{\mathrm{THz}} << \frac{1}{n_0^2}$, the effective refractive index of the modified system is

$$n_A = n_0 + \frac{1}{2}n_0^3 r_{41}E_{\mathrm{THz}} \tag{3.12}$$

$$n_B = n_0 - \frac{1}{2}n_0^3 r_{41}E_{\mathrm{THz}} \tag{3.13}$$

The gate pulse, as it co-propagates with the THz pulse through the electro-optic material, experiences a birefringent environment proportional to the electric field strength present. The effect of the THz on the material is assumed to be instantaneous for all practical purposes, hence the detector response function of this process is fundamentally given by the convolution in time and space of both pulses, as well as the velocity mismatch.

The induced ellipticity of the probe beam as function of relative time delay in THz pulse is the read out in a balanced detection scheme. In this scheme, the probe propagates through a quarter wave plate, Wollaston prism, and is then detected by two balanced photo diodes. In the case of no THz, the probe polarization is turned circular by the quarter wave plate, split into s and p polarization by the Wollaston prism, and each beam is detected by one photo diode. In this no THz example, both beams have equal intensity, and therefore the detected balance signal is $\Delta I = 0$. If THz light is present, the detected intensities are out of balance according to equation 3.14.

$$\Delta I = I_0 \Delta\varphi = \frac{I_0 \omega L}{c} n_0^3 r_{41} E_{\mathrm{THz}} \tag{3.14}$$

By measuring at different time delays, the entire THz field can be sampled and reconstructed. Equation 3.14 can also be solved for the electric fields and used to extract the amplitudes in absolute units according to equation 3.15, if the relevant material parameters of the electro-optic crystal are known.

$$E_{\mathrm{THz}}(t) = \frac{c}{\omega n_0^3 r_{41} L} \frac{\Delta I(t)}{I_0} \tag{3.15}$$

3.1.2.2. Gallium phosphide detection efficiency

The generated THz pulses used in this work are spectrally broad compared to other OR sources, and exhaust the available detection bandwidth of GaP in the EOS scheme. The detection limit is given by a phonon mode of GaP located at around 11 THz. In its vicinity in the frequency domain, the refractive index $n(\omega)$ and the electro-optic coefficient $r_{41}(\omega)$ are modulated. These effects were modeled by Leitenstorfer *et al.* [95] and are plotted for the case of a 50 µm thick crystal in Figure 3.2 with the material parameters for GaP taken from Leitenstorfer *et al.* [95] and Mankowsky *et al.* [96]. Panel a shows the refractive index $n(\omega)$ and extinction $k(\omega)$ (real and imaginary parts of the complex refractive index), while panel b shows the electro-optic coefficient $r_{41}(\omega)$. Mathematically, they are expressed by equations 3.16 and 3.17 [97].

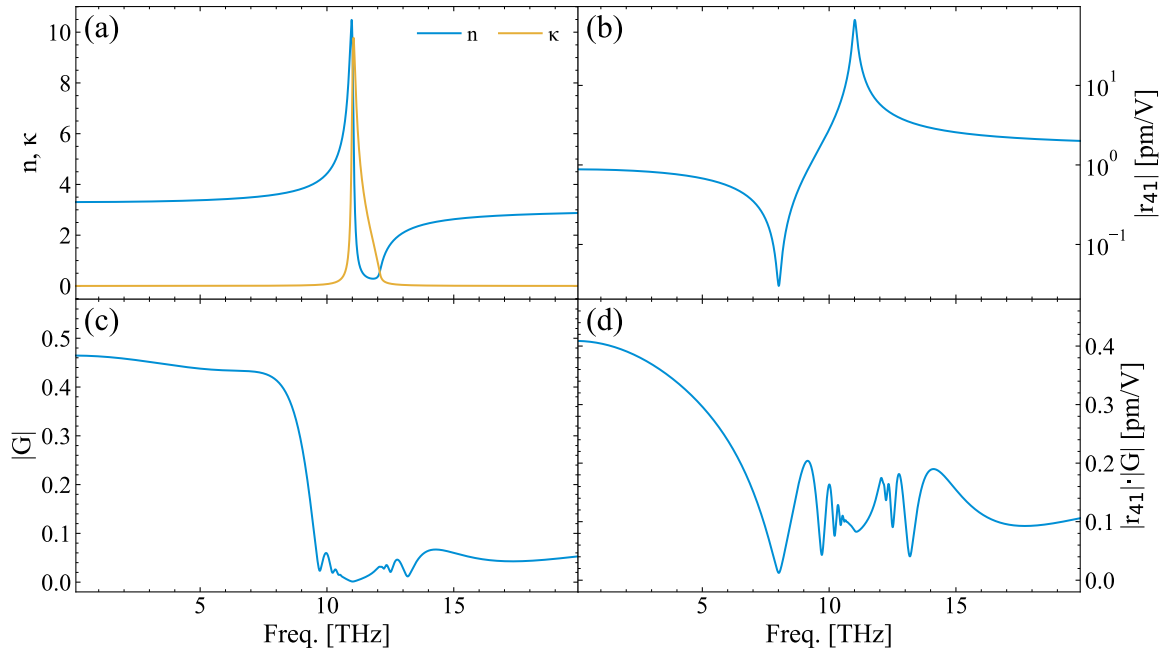

Figure 3.2.: Gallium phosphide material parameters determining the EOS detection efficiency. (a) Real and imaginary part of the refractive index. (b) Electro-optic coefficient. (c) Efficiency based on Fresnel transmission and velocity mismatch. (d) Total detection efficiency.

$$n(\omega) = \sqrt{\epsilon_\infty \left[1 + \frac{(\hbar\omega_{\mathrm{LO}})^2 - (\hbar\omega_{\mathrm{TO}})^2}{(\hbar\omega_{\mathrm{TO}})^2 - (\hbar\omega)^2 - i\hbar\gamma\omega}\right]} \tag{3.16}$$

$$r_{41}(\omega) = r_{\mathrm{e}} \left(1 + C\left(1 - \frac{(\hbar\omega)^2 - i\hbar\gamma\omega}{(\hbar\omega_{\mathrm{TO}})^2}\right)^{-1}\right) \tag{3.17}$$

Consequently, three effects play into the total detection efficiency. The refractive index dictates the frequency dependent Fresnel reflection strength and the velocity mismatch with the NIR probe pulse centered at 800 nm wavelength λ_{o} experiencing the group index $n_{\mathrm{g}}(\lambda_{\mathrm{o}})$. Both effects are expressed in equation 3.18 and plotted in Figure 3.2c, with the first term representing the Fresnel transmission into the crystal and the second term representing the averaged electric field over the velocity mismatch [98]. Thirdly, the electro-optic response of GaP to the THz field is frequency dependent, meaning certain frequencies could be underestimated.

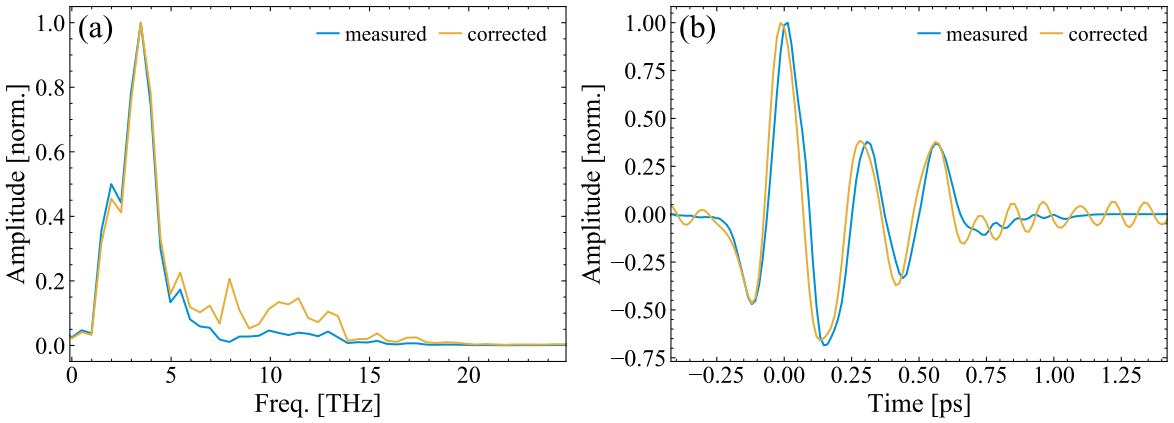

Figure 3.3.: Measured and corrected (a) spectra and (b) time traces for 50 µm *GaP. The ringing in the corrected time trace stems from the* 8 THz *peak in the corrected spectrum, generated by the minimum in the response curve.*

$$G(\omega) = \frac{2}{n(\omega)+1} \cdot \frac{c[\exp(-i2\pi\omega d(n_g(\lambda_o) - n(\omega))/c) - 1]}{-i2\pi\omega d(n_g(\lambda_o) - n(\omega))} \tag{3.18}$$

In total, the detection efficiency of GaP in EOS schemes is expressed as $R(\omega) = G(\omega) \cdot r_{41}(\omega)$ and is corrected in frequency domain by division $E_{\mathrm{THz}}(\omega) = E_{\mathrm{measured}}(\omega)/G(\omega) \cdot r_{41}(\omega)$. This total detection efficiency is presented in Figure 3.2d, showing a roll-off to zero until 8 THz, representing the underestimation of the higher frequencies and the bandwidth cutoff in these experiments here. In practice, the traces in time should be Fourier transformed into frequency domain, corrected, and back-transformed into time domain. The measured and corrected spectra (normalized) are shown in Figure 3.3a, and the THz traces in time domain are shown in panel b. The underestimation of spectral content up to 8 THz is evident. Furthermore, the corrected time trace is faster by an estimated factor 0.97, and was showing a significant amount of high frequency noise, originating from the fast oscillations in $R(\omega)$ above 8 THz (Figure 3.2d), which was suppressed in frequency domain before the back-transformation. The ringing before and after the main pulse in the corrected time trace stems from the 8 THz peak in the corrected spectrum, generated by the division of the minimum point in $R(\omega)$.

This correction will be applied in the THz Kerr analysis in Chapter 5.2, since the exact THz time trace is of importance there. It will be performed by scaling the THz time axis by this factor 0.97, with the above analysis serving as justification. The spectroscopy data of Chapter 5.1 will remain unaffected by the correction, since it is analyzed by referencing the traces containing the sample information against traces without sample in the beam path.

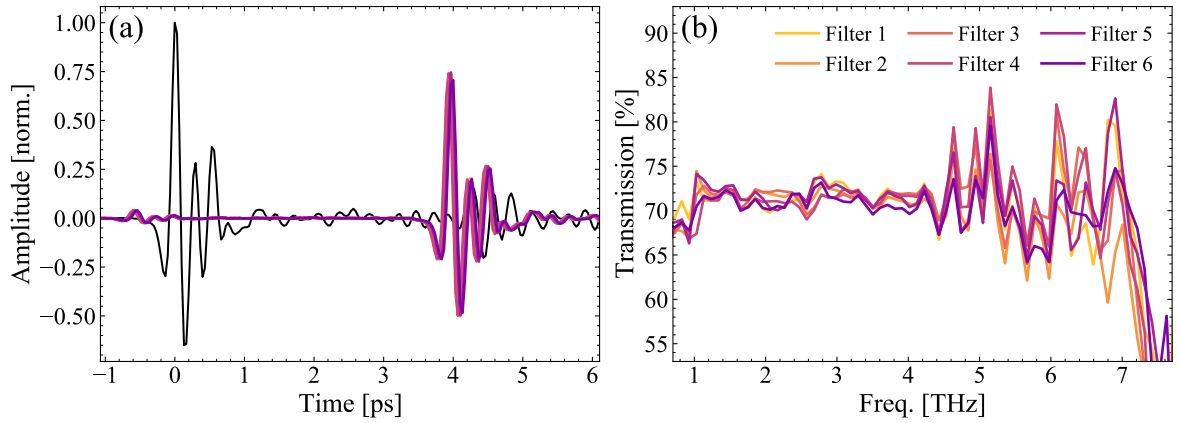

Figure 3.4.: Attenuation properties of all used Si transmission filters. (a) THz traces in the time domain, referenced against an unattenuated pulse. (b) The resulting frequency resolved transmission spectrum.

3.1.3. THz attenuation

One key parameter in this work presented here is the scaling behavior of the measured response with THz field strength. In general, there are many ways in which THz light can be attenuated [99, 100]. One convenient and continuously tunable method is based on two wire grid polarizers in sequence, but bandwidth is a concern. Another simple method is to attenuate the pump beam which is driving the OR process in the nonlinear crystal. But this method also influences the generated frequency content of the THz pulse, making analysis by amplitude and shape overly difficult. The method chosen for attenuation in this work is based on insertion of intrinsic Si wafers. Here, attenuation is achieved through simple Fresnel reflection on both Si interfaces. As depicted in Figure 3.4, intrinsic Si has a flat refractive index across the relevant part of the THz spectrum ($n = 3.42$), which leads to reflection loss of the electric field of 70% (50% in intensity). One drawback is that attenuation can only be controlled in increments of 0.7^N, with N being the number of wafers, and fine tuning is not possible. For each inserted filter, the THz beam accumulates relative delay against the NIR gate pulse of 4 ps, due to the increased optical path length of $l_{\text{opt.}} = (n_{\text{Si}} - 1)d$.

3.1.4. THz spectral filtering

Part of the work presented in this thesis explores the measured response of the sample for different THz pulse shapes. The simplest form of pulse shaping is spectral filtering, cutting frequency components from the incoming pulses. For this purpose, a set of THz bandpass filters is available and characterized. In general, the consequences of bandpass filtering for the transmitted pulse shapes are a narrower spectrum leading to a longer pulse duration accordingly, and a loss of peak intensity/field strength, since spectral intensity is simply discarded.

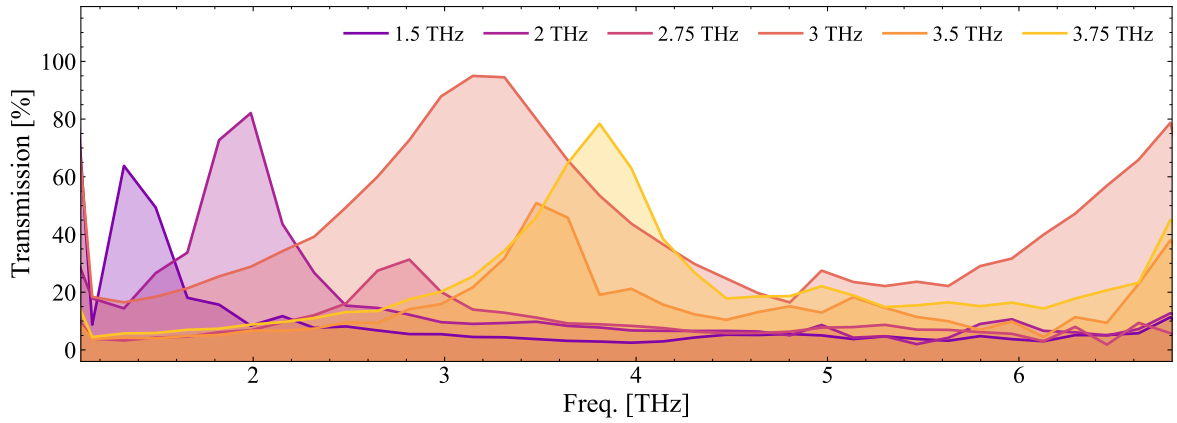

Figure 3.5.: Selection of available THz transmission bandpass filters as function of frequency, provided by Lepto.

The filters used here (provided by *Lepto*) [101] are constructed of patterned gold foil deposited on thin (micrometric) TOPAS foils (section 4.4 for further general THz properties of TOPAS). This ensures relatively high transmission through the supporting substrate, with negligible relative time delays for the pulses in the experiment. Each available filters is characterized through standard THz-TDS and the transmission spectra are presented in Figure 3.5.

3.2. Experimental realization

The entire THz Setup is depicted in Figure 3.6. It is designed to allow for easy back-and-forth between TDS (Fig. 3.12) and Transient Kerr measurements (Fig. 3.21). The following section will introduce the overall setup with the elements relevant to both configurations. Afterwards, each configuration is discussed in detail in dedicated subsections.

All beams in the setup originate from the same commercial Ti:Sa (titanium doped sapphire as lasing medium) system. The output is split and frequency converted as needed through nonlinear processes, and finally recombined in the relevant interaction regions with variable delay. The initial source is an Astrella-He system produced by *Coherent*, and it delivers pulsed 800 nm light of 35 fs (nominal) duration at 1 kHz repetition rate. The output polarization of the NIR pulses is p-polarization or horizontal in the lab frame. The total output power is above 9 mJ and the majority of it ($\sim$ 8 mJ) is used to pump a commercial optical parametric amplifier (OPA) system (TOPAS Prime-He, *Ligth Conversion*). It is split off by a 90:10 beamsplitter located right after the Astrella output port, and the transmitted 10% is available for other applications. A fraction of this fraction (split off with a pellicle right after the first beamsplitter) is used as a gate pulse in the THz setup. The targeted THz pulses in the setup are generated from multiple down conversions of the NIR light propagating towards the OPA.

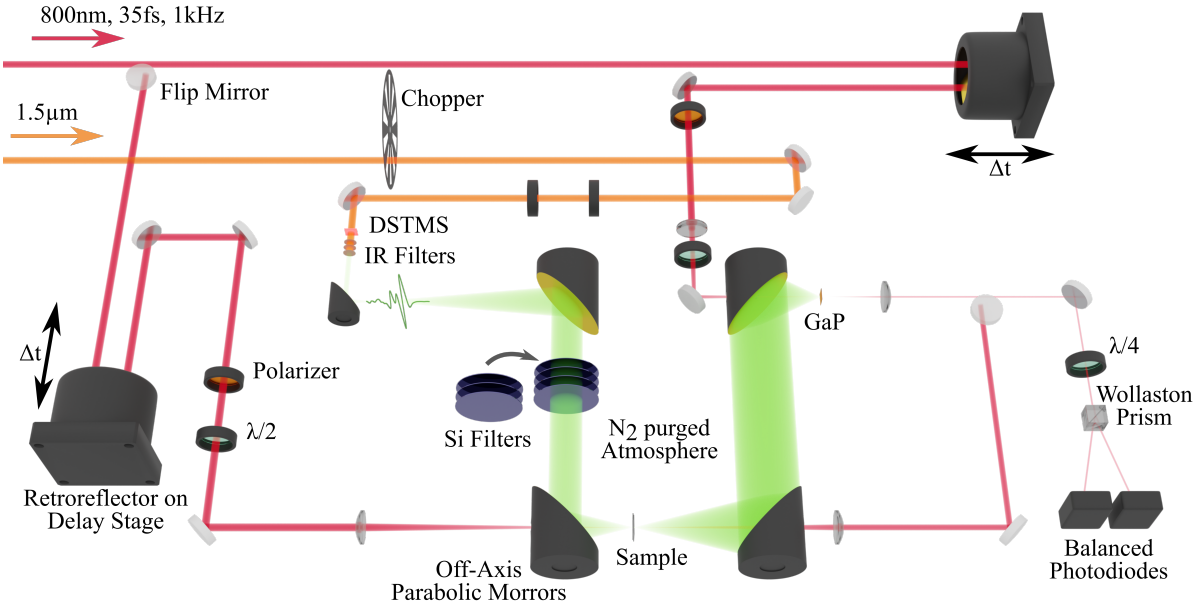

Figure 3.6.: Overview over the experimental setup, enabling time domain spectroscopy (TDS) and THz Kerr measurements with minimal adjustments. The THz pulses (green) are generated by pptical rectification in the organic crystal DSTMS by pumping with 1.5µm pulsed light (orange). Off-axis parabolic mirrors guide the THz light to the interaction regions with the sample and electro-optic crystal (GaP). Broadband attenuation is achieved by insertion of Si wafers acting as 70% attenuators. For both measurement types, the same ultrashort 800nm gate pulse (red) is used and measured in standard balanced detection configuration. The gate pulse has variable delay by retroreflectors on delay stages, and can be modified in its polarization state by half wave plates. The environment is encapsulated and purged with dry nitrogen, in order to avoid absorption by water.

The OPA consists of three stages and is tunable across signal and idler beams between 1.15 µm to 2.6 µm in wavelength. The output polarizations of the signal is s-polarization (vertical), and of the idler p-polarization (horizontal). The three stage nature of the design allows for high conversion efficiency and therefore high pulse energy at the output. In practice, the peak efficiency sits at 1.3 µm, as can be seen from the tuning curve in Figure 3.7. In terms of pulse duration, it is estimated at 50 fs. It has not been independently measured, since only the THz pulse traces are of importance, which are intrinsically characterized as part of the experiments. Both the signal beam of the OPA and the 800 nm beam coming directly from the Ti:Sa laser are guided to the setup via standard silver optics (red and orange beams in Figure 3.6). The second frequency conversion from infrared signal beam to final THz pulse is done further downstream, close to the sample.

The conversion into the THz regime is realized by OR in the organic crystal DSTMS [88,

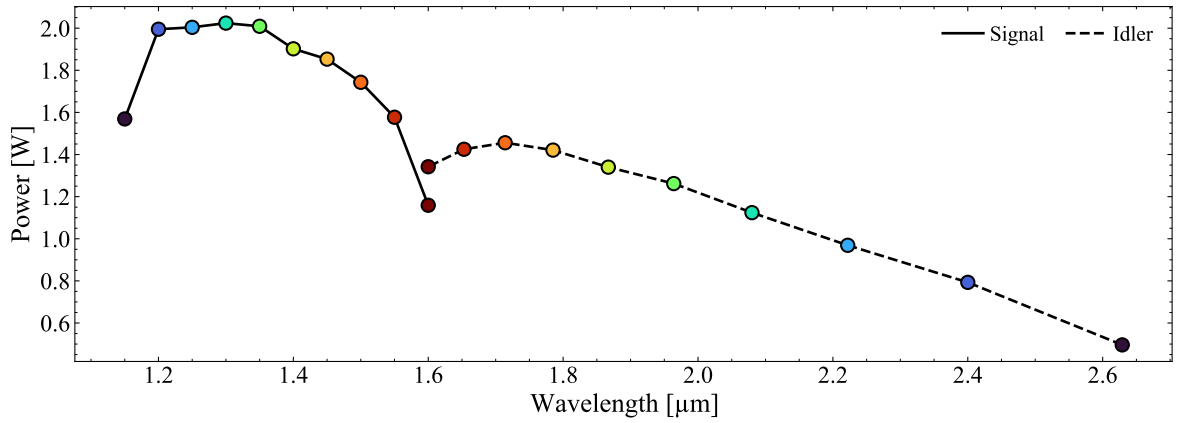

Figure 3.7.: Typical tuning curve of the TOPAS-He system in the laboratory. The signal is tuned between 1.4 µm *to* 1.55 µm *to drive the optical rectification process in the THz setup. The colored markers are meant to indicate which signal and idler wavelengths are generated in tandem, in other words their sum frequency would yield back the input* 800 nm *wavelength.*

102], as detailed in section 3.1.1. The relatively high conversion efficiency at simple collinear phase matching across a broad bandwidth between 1 THz to 7.5 THz makes the inclusion in the setup straightforward. The DSTMS crystals used in this work have been purchased from *Rainbow Photonics* and have a 6 mm open aperture with 600 µm thickness along the propagation direction. The signal pump beam coming from the OPA is collimated down to fit this size, and is tuned in wavelength from 1.4 µm to 1.5 µm, depending on the experiment.[1] After the IR pump beam propagates through the DSTM crystal, the residual IR intensity is filtered out by a set of three consecutive THz-transparent IR-filter foils, in order to avoid any possible damage of the sample and optics, or even unwanted interaction within the sample.

The OPA pump beam, before entering the OR crystal, is chopped to half the repetition rate with a 50% duty cycle chopper. Chopping before the OR process, rather than after, improves the average power experienced by the sensitive organic OR crystals. The acquisition of the THz experiment is done by referencing against signal without THz pulses present. In detail, the acquired time traces are measured by the balanced photo diodes as $V_{\mathrm{THz-on}} - V_{\mathrm{THz-off}}$, and averaged over 1000 events for each data point. This eliminates drift of the laser system and offset in voltage, coming from different responses of photo diode A and B. Furthermore, each measurement is the average of multiple passes of the delay stage, typically five.

The broadband THz light is best guided through reflective optics. Transmissive optics suffer from potentially high loss (depending on the material), and chromatic aberration given the large relative bandwidth, especially within this work. Off-axis parabolic mir-

[1] 1.5 µm provides slightly higher THz peak fields, which has been fully optimized for the Transient Kerr measurements. This difference is hardly an issue, since the relevant parameter, the THz trace in time, is always fully known through direct measurements via EOS.

rors (OPM) are the standard choice for these applications. In this setup, the THz is propagating through a five 90 ° OPM system. In sequence of beam propagation they are:

1. A telescope configuration consisting of a 1 inch focal length and 6 inch focal length OPM, with a focus in between. They pick up the collimated beam, expand it by a magnification factor 6, and collimate it again. This collimated section contains a stack of movable Si intensity filters, as described in section 3.1.3. The large magnification ensures tighter focusing afterwards, in order to increase the achievable field strengths in the sample.

2. The beam is picked up by a third OPM of 2 inch focal length and focused into the interaction region of the light with the sample.

3. After the sample, the transmitted light is collected by an 4 inch focal length OPM, which again collimates. These two OPMs before and after the sample have each a small hole in them to allow for a further probe beam to co-propagate with the THz optical axis.

4. Finally, the fifth OPM of 2 inch focal length is focusing the THz pulses into the electro-optic crystal for EOS. It has a hole for the EOS beam to co-propagate with the THz beam.

As stated towards the beginning of this section, the probe beam originates from a fraction of the unused Ti:Sa laser light. Right after the pellicle, it is collimated down to a few millimeter beam size by a telescope, and made to propagate a few meters between silver mirrors to compensate for the path length of the parallel OPA line, before entering the setup. There, it enters a corner cube retroreflector on a variable delay stage, followed by a polarizer (to ensure well defined linear polarization), a $\lambda/2$ wave plate (to enable control over the polarization angle),[2] and finally a lens that focuses the beams into the interaction region through the holes of the OPMs. The spot size of the probe is on the order of magnitude 10 µm FWHM, much smaller the the order of 100 µm FWHM of the THz beams[3]. Afterwards, the probe is measured in balanced detection condition as described in the previous section 3.1.2. The switch between TDS and THz Kerr configurations is done with two flippable mirrors.

Overall, one parameter that commonly requires addressing in THz experiments is the absorption by atmospheric water. In gas phase, it has multiple absorption lines in the

[2]Note on the order of polarizer and waveplate: ideally, the polarizer is the last element before the interaction region, in order to truly ensure a well defined linear polarization. In practice, with the optics available the beam pointing is strongly affected when rotating the plane of polarization, negatively impacting the spacial overlap of THz and probe beams, as verified by placing a CCD camera in the focus position. Therefore, the order is set as described in the main text, with the polarizer only set with its transmission axis to the incoming polarization, and then the waveplate to turn afterwards. This has been found to keep the pointing change to a manageable amount, at the cost of a small but negligible amount of static ellipticity, when moved out of its initial condition.

[3]Measured by knife edge method

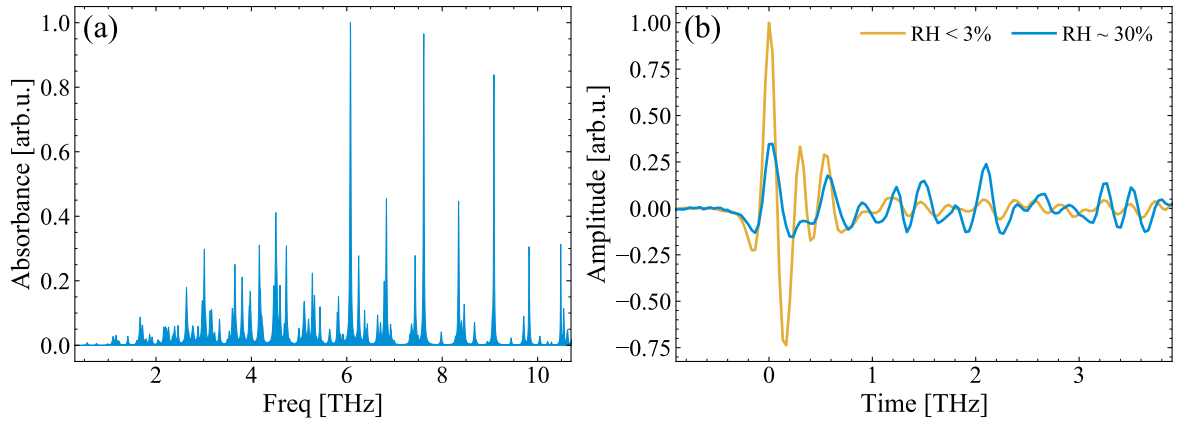

Figure 3.8.: (a) Absorption spectrum of atmospheric water across the THz frequency range, taken from the HITRAN database [103]. (b) THz pulses measured as function of relative humidity (RH).

THz range related to rotational transitions, shown in Figure 3.8a. Therefore, humidity in the environment has to be controlled. It is standard (and cost effective compared to vacuum solutions) to purge the volume in which the THz pulses propagate with nitrogen or dry air. Here, nitrogen is used to purge the volume from the DSTMS crystal to the GaP crystal for TDS. This volume is enclosed by a box with openings and exits for all beams used. The humidity level is monitored by *Sensirion* sensors and typically kept stable below 3% relative humidity.[4] This 3% level is chosen as a compromise between the marginal gains from better relative humidity and the time it requires to purge further down. Panel b of Figure 3.8 shows THz pulse measurements in humid and dry environments for comparison.

3.2.1. THz properties

The typical DSTMS generated and GaP detected pulses are shown in Figure 3.9, accompanied by the frequency spectrum. The measured traces compare well with published data, even though in the spectral domain, significantly more intensity is seen in the higher frequency parts of the spectrum. This is likely due to the shorter than usually reported pump pulse duration, which is directly responsible for larger bandwidths in OR processes. Furthermore, the spectral signal has a shoulder between approximately 5.5 THz to 7.5 THz which is still useful for linear absorption spectroscopy, albeit with larger uncertainty bands given the reduced signal-noise ratio (snr). At the low frequency end of the spectrum, the generation crystal DSTMS presents an IR active phonon (lattice vibration mode) at 1 THz, hence everything at and below 1 THz will be neglected.

The experimental setup contains two interaction points in which the THz beam and the

[4]The laboratory is stabilized to 20 °C, but not humidity stabilized. It can vary between 25% to above 70% depending on the outside conditions and season.

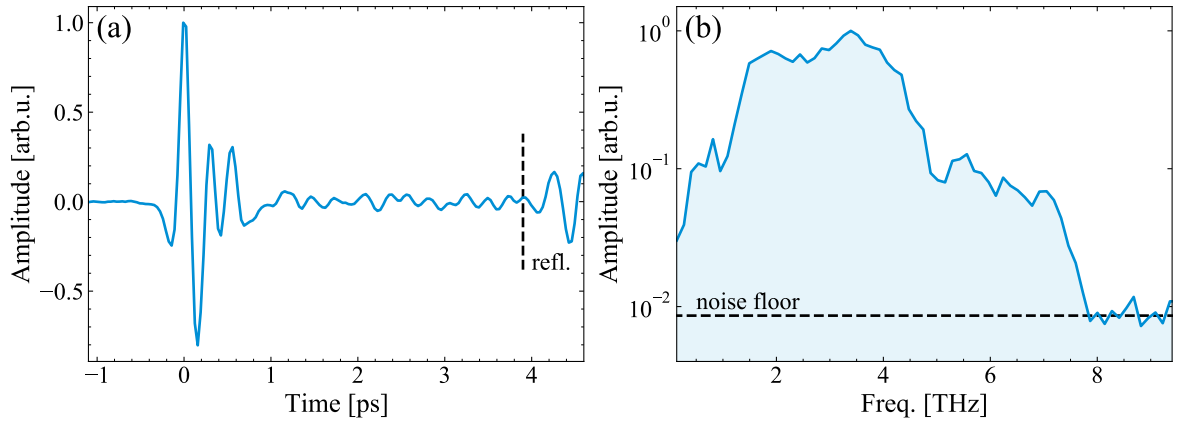

Figure 3.9.: Typical DSTMS generated THz traces in the THz experiments reported within this work (a) Normalized THz traces in the time domain. (b) The resulting normalized frequency spectrum.

probe beam co-propagate through a common focus. In other words, in these two points the THz pulse can be fully characterized. In the EOS focus for the TDS measurement, this is a standard part of the protocol. While the shape of the pulse contains important information for the spectral analysis, the amplitude in physical units is neglected, since only the relation to the reference matters. The second case of the interaction point with the sample itself is different, in that characterization of the THz transients in shape and strength is explicitly required. This means removing the entire sample stage and replacing it with an EOS crystal. The reasons are twofold: (i) The exact shape of the traces are necessary in evaluating the dynamics induced in the Kerr response, since they are governed by the THz driving fields. (ii) For the nonlinear experiments, knowledge of the absolute value is necessary and measured through EOS, in order to extract physical system parameters.

Using the formalism presented in equation 3.15, the peak fields in the sample position are estimated to reach $2\,\mathrm{MV\,cm^{-1}}$. These values are measured using a thin GaP crystal of 50 µm thickness, and attenuating the THz beam going into the crystal with six silicon wafers acting as transmission filters (see section 3.1.3 for details). The directly measured THz field strength is then calibrated back with the known attenuation factor. These two steps are necessary in order to keep the electro-optic response of the detection crystal in the linear regime and prevent saturation. A further aspect to consider is that the four times thinner GaP has a closer internal reflection signal in the time trace. Hence, the usable Fourier window is shortened accordingly, and the resolution in frequency space is reduced significantly. Therefore, as a general rule applied within this work, for characterization in time domain the thin GaP is used, for evaluation of the spectroscopic content the thick GaP is used.

The majority of results presented in this thesis have been obtained with the DSTMS generated THz pulses. One part towards the end makes use of changed pulse shapes. This is achieved in two ways. Firstly, exchanging the generation crystal, and secondly

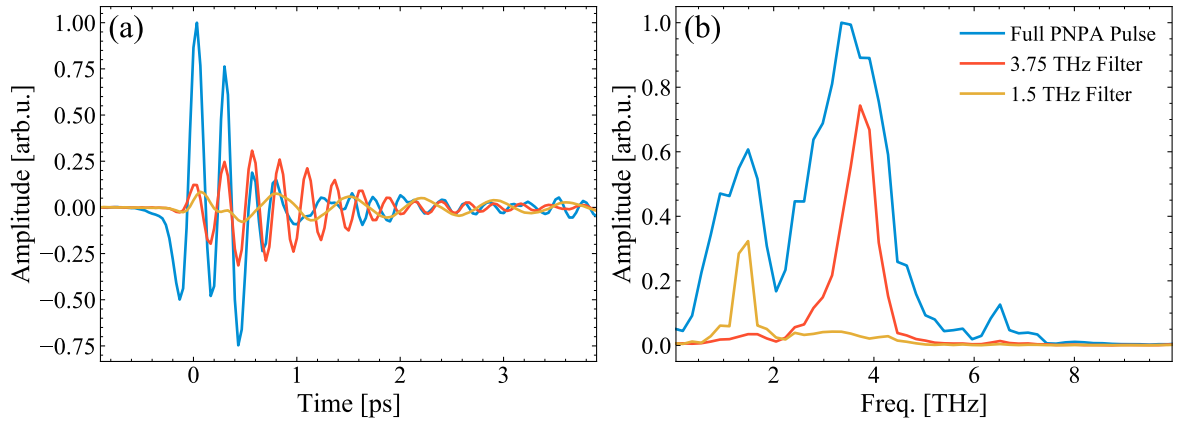

Figure 3.10.: (a) TDS traces measured in the sample position, generated using PNPA for generation and bandpass filters (b) Corresponding frequency spectra

through further spectral filtering. In terms of crystal, the choice is PNPA, provided by *THz Innovations*, and it generates similar yet distinct THz time traces with peak fields on the same order of magnitude. It is pumped with a slightly detuned OPA signal beam of 1550 nm, yielding peak field strengths of 1.45 MV cm^{-1}. In combination with the bandpass filters, a significant amount of field strength is lost. The corresponding peak fields are on the order of 500 kV cm^{-1} and 100 kV cm^{-1} for the 3.75 THz and 1.5 THz filters. Given the nonlinearity of the response, the expected strength of the signal will be weaker accordingly, and therefore also the snr. The measured THz time traces are shown in Figure 5.24a and their corresponding spectra are shown in panel b.

3.3. Time domain spectroscopy

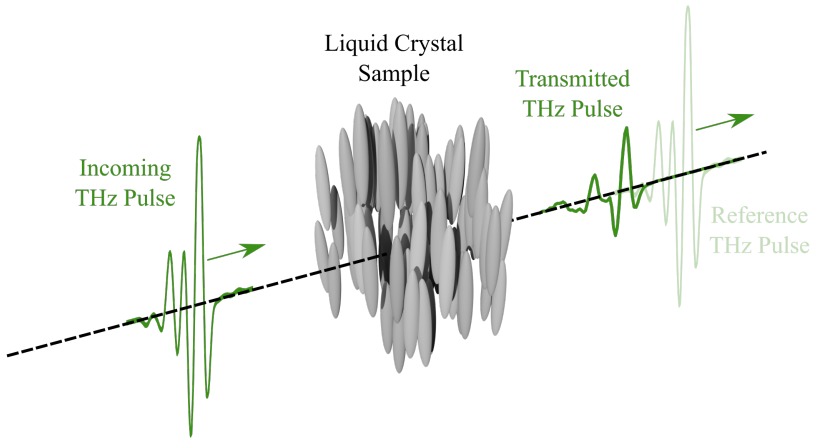

Figure 3.11.: THz time domain spectroscopy scheme. A THz pulse is transmitted through the LC sample (planar alignment as depicted - extraordinary axis, or planar perpendicular - ordinary axis), and measured after propagation though interaction region. It is referenced against a THz pulse measured without sample in the region.

The TDS configuration setup is depicted in Figure 3.12. It requires the gate beam to pass through the last OPM and to overlap with the THz beam inside the electro-optic crystal. Here, it is a 200 µm thick GaP of (110) cut, which gives a good compromise of phase matched coherence length [73] and temporal cutoff due to multiple reflections inside the crystal. Both attributes play a role in the data quality for spectroscopy. While the first effect is represented by a general instrument response function, expressed as a convolution of the real pulse with a Gaussian representing the walk-off in time, the second effect limits the available information for the Fourier Transform, since the data containing the reflection needs to be cut from the measured traces. The general properties of FFTs dictate that the length of the available time interval is directly proportional to the resolution in frequency space. Another aspect is the 35 fs pulse duration of the gate, which limits the resolution.

The THz pulse is vertically polarized, while the gate pulse is horizontally polarized. The gate pulse is on a variable mechanical delay through a *Thorlabs* delay stage, enabling the sampling of the THz pulse.

THz-TDS is conceptually equivalent to absorption spectroscopy in any other wavelength range. The typical mode of operation in any case is to measure the intensity spectrum of two light beams, one that is transmitted through the sample of interest and one that acts as a reference. After the optical setup, the light is converted into the spectral domain, collected, and finally the absorbance is calculated, typically assuming Lambert-Beers law. The conversion to spectral domain is typically done on the table top with dispersive optics, such as prisms and gratings. Since in the THz range the pulses are fully known in time, there is no need for optical treatment and the spectrum of all THz pulses can be accessed via standard Fourier transformations. In addition, as

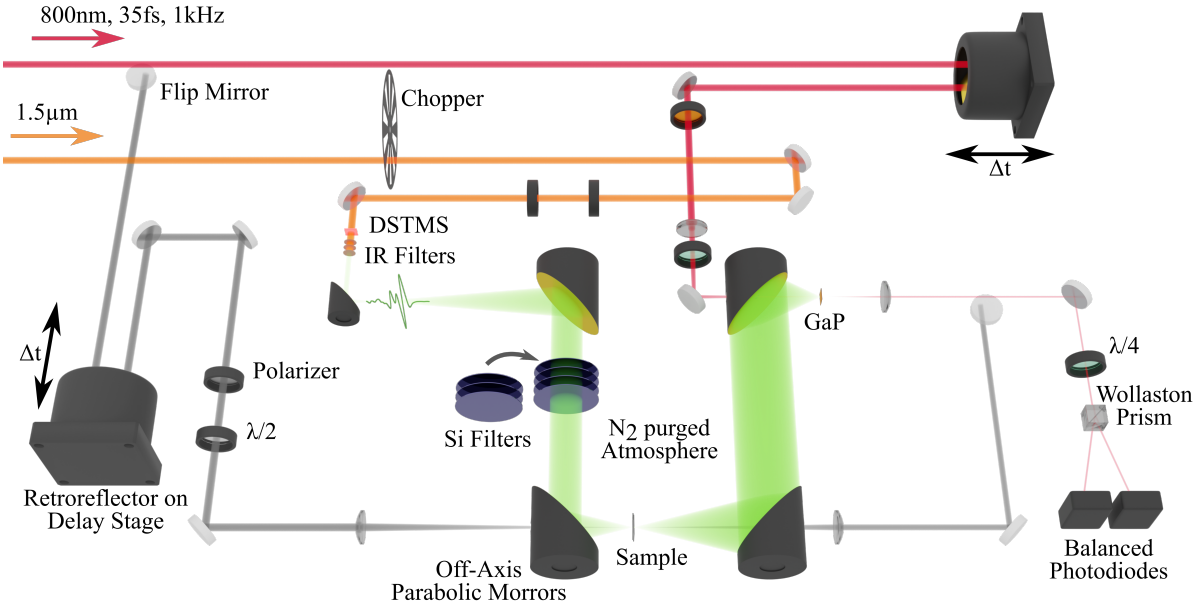

Figure 3.12.: THz Setup for time domain spectroscopy. The optics and beams used for this measurement technique are highlighted in color, while the unused parts are grayed out.

already stated above, the full phase information between the two beams allows access to the refractive index and dispersion of the sample across the spectral range covered by the THz pulse.[5]

The standard formulation to calculate TDS spectra out of the measured time traces is based on Lambert-Beers law for electric fields and is modified to account for reflection losses that would lead to overestimation of the absorbance [69]. Fresnel loss is only dependent on the refractive index discontinuity at the sample interfaces, depends only on the refractive indices and the angle of incidence, and is included with the factor $T^{-1}(n_{\text{Sample}}, n_{\text{Interface}}, \theta)$. This transmission factor simplifies for normal incidence and for sample-air interfaces, where $n_{\text{Interface}} = 1$. Furthermore, n_{Sample} is an intrinsic result of the TDS measurement scheme. Here the situation is more complicated, since the interface with the sample is formed by the cell window. The comparison between the filled cell and empty reference cell lead to transmission factors at every interface of the form $t_i = \frac{2n_1}{n_1+n_2}$, where i denotes the interface, and the indices 1 and 2 the medium through which the beam passes first and second. Finally, with $n_{\text{TOPAS}} = 1.54$ (see Figure 4.1), the correction factor reads as equation 3.19.

[5]Note that in the Mid-IR range, spectroscopy often also involves Fourier Transforms. In FTIR (Fourier Transform Infrared) spectroscopy both beams are interfered, and the resulting intensity recorded as a function of relative delay. The spectrum is then calculated via Fourier transform of this interference trace.

$$T = \frac{t_{\text{TOPAS}\to\text{Sample}} \cdot t_{\text{Sample}\to\text{TOPAS}}}{t_{\text{TOPAS}\to\text{Air}} \cdot t_{\text{Air}\to\text{TOPAS}}} = \frac{n_{\text{Sample}}(\omega)(1+n_{\text{TOPAS}})^2}{(n_{\text{Sample}}(\omega)+n_{\text{TOPAS}})^2} \tag{3.19}$$

Any electromagnetic wave propagating through a material will be modified by it's dielectric function $\epsilon(\omega) = (1 + \xi(\omega)) = (n(\omega) + i\kappa(\omega))^2$ which contains the material refractive index n and it's extinction coefficient κ according to Maxwell's equations [69, 73].

$$E(\omega) = E_0 \exp(ikr) = E_0 \exp\left(i\frac{\omega(n+i\kappa)}{c}r\right) \tag{3.20}$$

$$= E_0 \exp\left(-\frac{\alpha r}{2}\right) \exp\left(i\frac{\omega n}{c}r\right) \tag{3.21}$$

Here, $\alpha = 2\omega\kappa/c$ is the absorption coefficient. The real part of the exponential represents the amplitude attenuation from absorption, while the imaginary part is the phase shift experienced by the wave due to its refractive index. When referenced against the same THz field not propagated through the sample of thickness d, and including the transmission correction, one gets the following relation.

$$\frac{E_{\text{Sample}}(\omega)}{E_{\text{Ref.}}(\omega)} = T \exp\left(-\frac{\alpha d}{2}\right) \exp(i(n-1)kd) \tag{3.22}$$

$$\Delta\varphi = (n-1)kd \tag{3.23}$$

Thus, in detail the refractive indices $n(\omega)$ are extracted from the TDS measurements from the phase difference $\Delta\varphi$, and the absorption coefficient $\alpha(\omega)$ from the ratio of spectral amplitudes. Equations 3.24 and 3.25 are the standard relations in TDS between material parameters and experimental observables.

$$n(\omega) = \frac{\Delta\varphi(\omega)}{kd} + 1 \tag{3.24}$$

$$\alpha(\omega) = -\frac{2}{d}\ln\left(\frac{E_{\text{Sample}}(\omega)}{E_{\text{Ref.}}(\omega)}T^{-1}\right) \tag{3.25}$$

3.3.1. Practical considerations in TDS data processing

Both the extraction of the phase and the spectral amplitude from the acquired data come with a few practical difficulties, that need addressing. In this context, this section details the practical numerical procedures applied to the data presented in this work. Even though these details are all related to the nature of numerical Fourier transforms, this section is subdivided in three subsections: absorption calculation, phase retrieval, and uncertainty band definition [72, 100, 104].

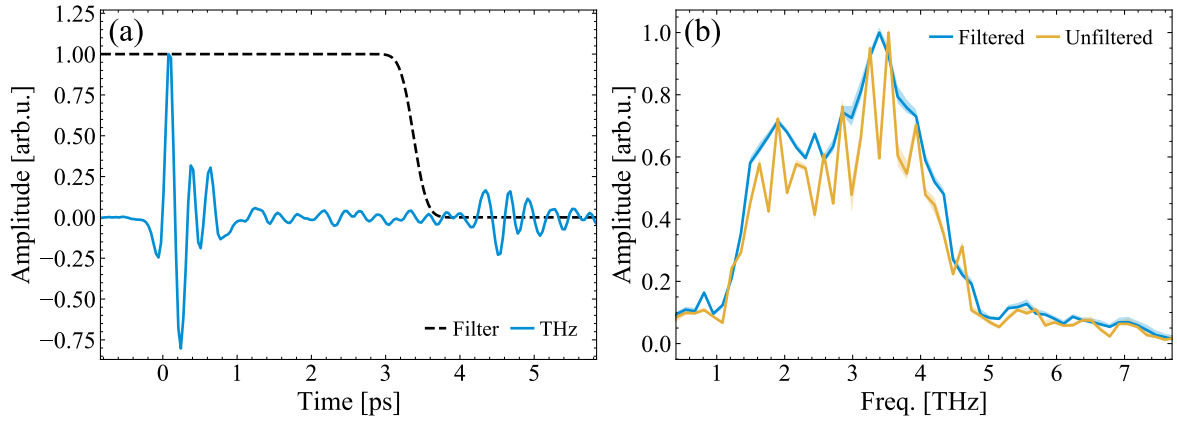

Figure 3.13.: THz filtering. (a) THz electric field trace in time domain, and associated filter function. (b) The THz spectra obtained by Fourier transformation with and without filter applied. The interference fringes from inclusion of the reflection are clearly visible in the ungated spectrum.

3.3.1.1. Absorption calculation

As touched on previously, the major limitation in the data is the co-propagation of a reflection within the EOS crystal that appears in the time traces with a temporal shift. Keeping it in the data processing will lead inevitably to interference fringes in frequency domain, and thus impact negatively on the quality of the results. Therefore, the reflection must be cut from the trace, which is setting a limit on the time interval available for the Fourier transform.

A general property of FFT is in their connection between sampling step size and cutoff from one domain into another. The step size in time domain dictates the cutoff in frequency domain in the form of the Nyquist frequency. The cutoff in time domain, on the other hand, which here is set fundamentally by the EOS crystal thickness, leads to a step size in frequency domain. In other words, the EOS crystal thickness defines a resolution limit in the spectral domain.

In this work, instead of truncating the array sharply before the reflection and possibly zero-padding the array, the reflection is suppressed by multiplying the array with a smoothly decaying function that has approached zero by the time the reflection appears [72]. The strictly ideal choice is a Gaussian function, since in Fourier transforms the multiplication of two functions in time domain results in a convolution of both individual Fourier transforms in frequency domain. Gaussians are ideal for such an application, since their Fourier transform is again a Gaussian, meaning in frequency domain the result is free of any artificial modulations.

Generally speaking, filter design is a deep field of signal analysis and processing with sophisticated solutions. In the context of the traces presented here, using simple error functions yield TDS results without apparent artifacts. Examples of the filter function and the calculated spectra are shown in Figure 3.13.

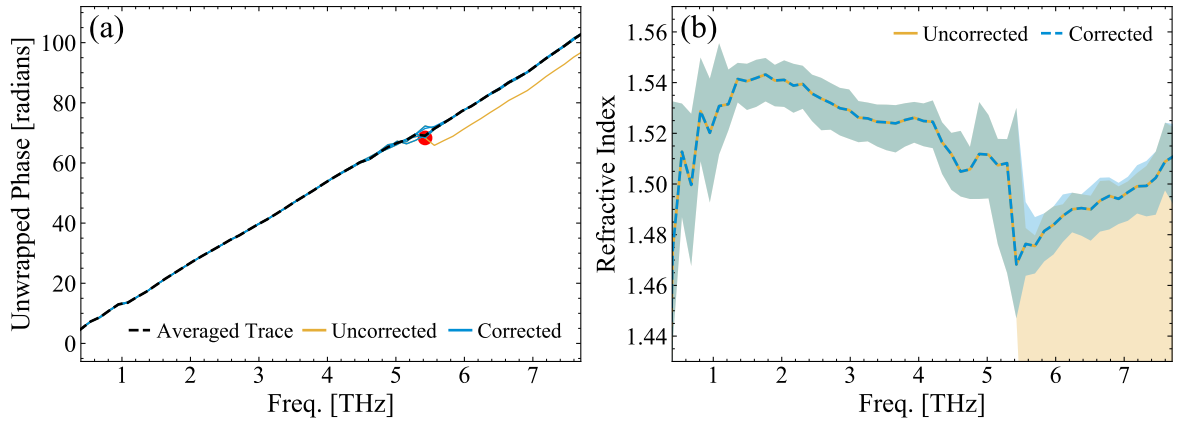

Figure 3.14.: Phase unwrapping corrections. (a) The unwrapped pases of the averaged THz trace in time, and the individual traces. A phase jump is clearly visible, and marked by the red circle. This data point is corrected by π. (b) The resulting refractive indices before and after correction.

3.3.1.2. Phase retrieval

A dedicated and comprehensive review of phase retrieval procedures specifically for THz applications has been published by Jepsen [104], but this section will provide the procedure as applied to the data within this work. The phases are calculated as the argument of the complex arrays that are the output of the standard numerical FFT functions. These numerical phases are returned as values between 0 and 2π, hence over the full spectrum the phase shows numerous discontinuities. In this state the calculated phase difference $\Delta\varphi$ between sampling pulse and reference is practically unusable and requires further processing.

This is a common problem in signal processing and standard functions for phase unwrapping are easily available in numerical packages. These functions look at the magnitudes of the phase jumps between points, and add a full 2π shift if a threshold is overcome. They work well in finely sampled, well-behaved data (continuous, low noise, etc.), but need checking in case these preconditions are poorly fulfilled. In the THz data within this work, this is frequently the case (rarely for the averaged traces, few times for the unaveraged traces per measurement), and these phase jumps are applied manually for every measurement from which the refractive index is extracted. Typically, it is easily evident from the final refractive index traces that a phase error is present. An example of a corrected and uncorrected unwrapped phase and the results for the refractive index are shown in Figure 3.14.

3.3.1.3. Uncertainty intervals

Uncertainty bands are reported with the absorption spectra and refractive indices extracted from the TDS measurements. THz spectroscopy is somewhat unusual, in that

measurements are carried out in time domain, but the sample properties of interest are given in frequency domain, such as absorption spectra. This means that the statistical errors have to be propagated through a Fourier transformation. These are linear operations from a mathematical point of view, and therefore should be possible in principle. In practice, it is not straight forward, even though work adapting numerical FFT algorithms to include error propagation exists [105]. Unfortunately, these methods are not standard inclusions in numerical packages and therefore have to be implemented. Hence, frequently confidence intervals are not reported in THz literature [106].

One way relative uncertainty of THz data is given, is by including the dynamic range of the experimental apparatus as part of the results. By identifying the noise floor in the spectral domain, an "absorption spectrum" is calculated from the reference and this noise floor level. The result represents the maximally measurable absorption in the experiment. The parts of the absorption spectra that reach the dynamic range level are excluded as unreliable [107]. Here, the samples are constructed to be thin enough to fit their absorption spectra just within the dynamic range of the experimental setup (with the exception of the sharp high frequency absorption band of 8OCB in Figure 5.2).

Instead, here qualitative uncertainty bands are reported, that are not strictly speaking providing a quantification in the form of a standard deviation or confidence level. The bands provide a relative uncertainty across the spectrum and are meant as a guide to the eye for the relative confidence. Each measured time trace is an average of several measurements in sequence to provide sufficient statistics. The reported spectra are calculated with the mean of each THz trace in time. The uncertainty band is formed by calculating the spectrum for every permutation of reference and measurement trace before taking the mean. This band represents the total spread of all these results and the area between its minimum and maximum represents a qualitative confidence interval. In this work, the uncertainty is plotted as a shaded area behind the bold lines calculated by the mean if the THz time traces.

3.4. Density functional theory calculations

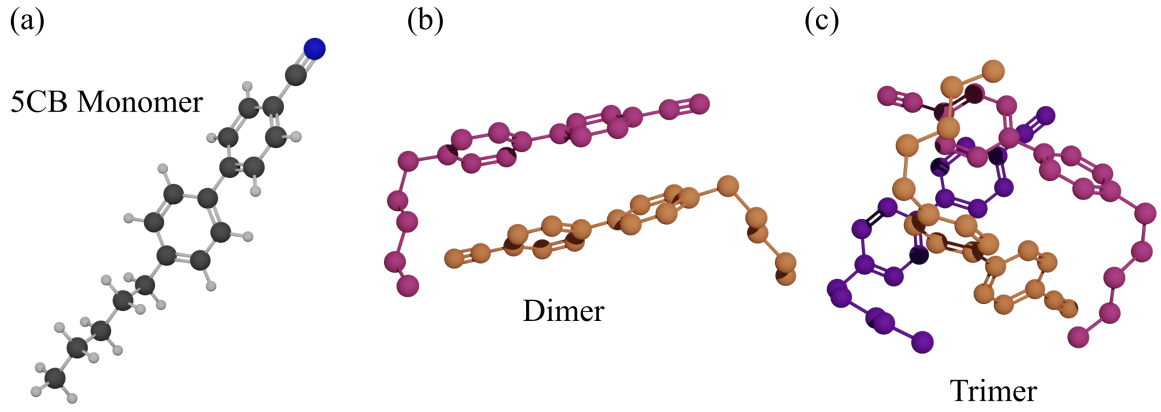

Figure 3.15.: (a) Monomer, (b) dimer, and (c) trimer structures of 5CB, used for the cluster DFT calculations. The molecules are colored and the hydrogen atoms are omitted for improved readability. The structures are picked from the pool of conformers found in the DFT computation.

To interpret the measured spectra, theory calculations were performed for comparison and mode assignment. This was done in collaboration with Prof. Galimberti (Radboud University Nijmegen), who ran the calculations. The analysis of the results was done in collaboration. As a simplest analogue to the condensed phase experiments, the calculations consider gas phase single molecules, since a bulk phase description is computationally expensive and time consuming beyond the limit of this work. The LC molecular arrangement shows positional (flow) and rotational (order parameter) degrees of freedom, similar to liquids. As a consequence, simplifications like periodic boundary conditions, representing unit cells (for example for crystalline systems), lose their cost advantage, because the box has to contain thousands of molecules in order to give accurate results [108, 109]. This single molecule approach is most successfully applied for MidIR absorption bands, where vibrations of specific molecular functional groups appear within a similar frequency window, and environmental influences lead to relatively small effects. In the low THz regime, once the interatomic forces associated with these low frequency oscillations compete with the intermolecular forces, the spectral response becomes increasingly complex. The transition from the intramolecular regime to the intermolecular one cannot be easily identified, and it is reasonable to expect presence of both types of vibrations across this transition. Nevertheless, gas phase DFT calculations provide useful comparisons to help interpretation of the measured spectra. In order to learn about the role of intermolecular effects on the spectra, the single molecule calculations are extended with dimer and trimer calculations, still in the gas phase.

3.4.1. DFT basics

Simulating molecular properties with accuracy is challenging, because a full quantum mechanical description of complex systems is an electronic many-body problem, and solving the full Schrödinger equation is often not feasible [3, 110]. The well known Hartree-Fock method approaches such systems by assuming (in addition to the Born-Oppenheimer approximation) that each electron can be treated independently, interacting with a background field representing all other electrons in the system. This means electron exchange is modeled by ensuring the wave function is fully antisymmetric, while electron correlations are completely omitted.

Density functional theory (DFT) takes a different approach, where the electron density $\rho = \sum_i |\Psi_i(r_i)|$ is in the center of the description. Here, the total energy of the system is given by a functional of the density $F[\rho]$, and the potential $V(r)$ in which the density lives. The total energy of the system is then given by equation 3.26.

$$E[\rho] = F[\rho] + \int V(r)\rho(r)dr \tag{3.26}$$

The challenge is in finding the exact form of the functional, since it is a priori not know. These days, the choice of functional is numerous and guided by the system under study and what properties are of interest. The atomic wavefunctions are represented by basis sets, meaning linear combination of primitive functions which build up the orbitals. Typically, the atom centered basis sets are constructed from Gaussian functions.

Furthermore, van der Waals forces (dispersion interaction) originate from fluctuations of the electronic structure, leading to transient weak dipole fluctuations. These forces are not included in the DFT methods and need to be corrected for, in order to compute accurate results. Interatomic dispersion energies are calculated separately and added to the total determined energy.

An accurate result of the electronic energies and potentials is necessary in order to compute reliable vibrational modes and intensities. The geometries of the systems under investigations are optimized for their energies with respect to atomic displacement. The resulting minima of the potential energy surface represent different conformations of the system. Finally, the quantity of interest is computed for each conformer individually and averaged with a weighting, typically of Boltzmann distribution form, where every calculated spectrum is weighted by a probability factor $p_i = \exp(E_i/k_BT)/Z$, with the partition function Z ensuring normalization.

Once the energetic minimum is found, it is possible to extract the vibrational dynamics of the system. In order to access the force constants of the oscillator, the interatomic energy is varied against displacement of the atoms with respect to each other, forming the Hessian matrix D_{ij}.

$$D_{ij} = \frac{\partial^2 E}{\partial r_i \partial r_j} \tag{3.27}$$

Finally, the Hessian is mass weighted and diagonalized. The results are eigenvalues representing the frequencies of the oscillator, and eigenvectors representing the vibrational

Table 3.1.: Number of conformers contributing to each calculated DFT spectrum

System	Number of conformations
5CB	27
8CB	264
8OCB	120
PCH5	29
5CB dimer	119
5CB trimer	219

normal modes. The IR intensities I_k of the calculated vibrations then depend on the induced dipole during the oscillation. They are calculated by the change in dipole moment μ of the system after displacement q_k along a vibrational normal mode k.

$$I_k = \left| \frac{\partial \mu}{\partial q_k} \right|^2 \tag{3.28}$$

In general terms, the procedure for calculating vibrational IR intensities through DFT methods is a four step process.

1. Search of the energetic minima, yielding the conformers and their geometries.
2. Computation of the Hessian matrix D_{ij}.
3. Computation of the eigenvalues and -vectors of D_{ij}, representing the vibrational frequencies and normal modes.
4. Computation of the intensities I_k for each normal mode of each conformer, and averaging with the appropriate weight.

3.4.2. Computational methods

The DFT calculations for this work are performed using the following procedures [111]. All spectra have been computed with the Gaussian16 code [112]. An (unconstrained) conformational search was run using the Gaussview software [113] and the MMFF4 force field as a first step for all the analyzed cases, imposing an energy window of 3.5 kcal/mol. From the generated pool of structures, in the case of the single molecule calculations, all the conformations have been retained for the next step. The number of structures for each case are reported in Table 3.1.

Afterwards, a geometry optimization at the DFT level for all the selected conformations is run. All the degrees of freedom have been fully optimized and no specific packing order/alignment imposed. In the case of the single molecules, the B3LYP functional [114, 115] augmented with the Grimme D3 dispersion term [116], and the 6-311++G** basis set have been chosen.

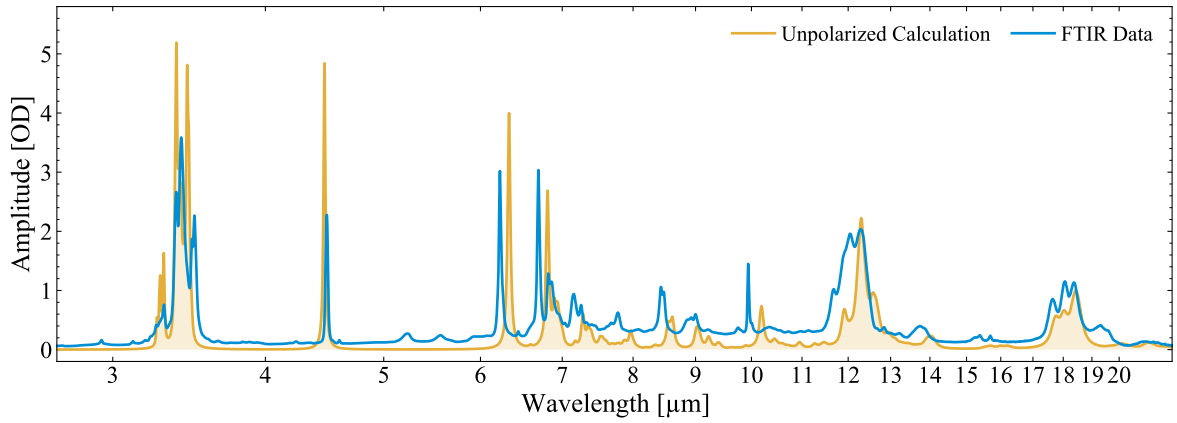

Figure 3.16.: FTIR spectrum of 5CB, once measured in amorphous sample alignment in a commercial Brucker spectrometer (red), and the calculated unpolarized DFT spectra

As a last step, the spectra for all the optimized structures are computed in double harmonic approximation at the same level of theory used for the geometry optimization. The final spectra have been obtained as a weighted average by the Boltzmann populations (at 323 K) of the set of computed spectra. The ordinary and extraordinary components of the IR absorption spectra have been computed projecting the induced dipole moment respectively on the direction perpendicular and parallel to the static dipole moment of the molecule.

As a proof of principle, Figure 3.16 shows an unaligned 5CB sample measured for comparison with the calculated results. Except for some minor expected red or blue shifts of the modes, the results agree well with each other. The amplitude offset in the experimental trace is due to reflection loss at the sample interface, which has not been accounted for.

3.4.3. Cluster calculations

One part of the discussion in the results chapter will consider how the computed spectra look for gas phase multi-molecule clusters, as a toy model approach to including intermolecular interactions in the compared spectra. This section outlines the approach taken in detail and Figure 3.15 shows representative structures.

3.4.3.1. Comparison 5CB to 8CB

Firstly, instead of 8CB, the slightly shorter 5CB molecule will act as a test case for this investigation, due to the computational cost. Figure 3.17a compares absolute intensities and the mode shapes of the 5CB and 8CB computed single molecule spectra. 5CB and 8CB have similar total (integrated) intensities per molecule in this spectral region, which is not surprising, considering that the activity of this region is dominated by the contributions of the cyano group and the phenyl rings (charges and charges fluxes),

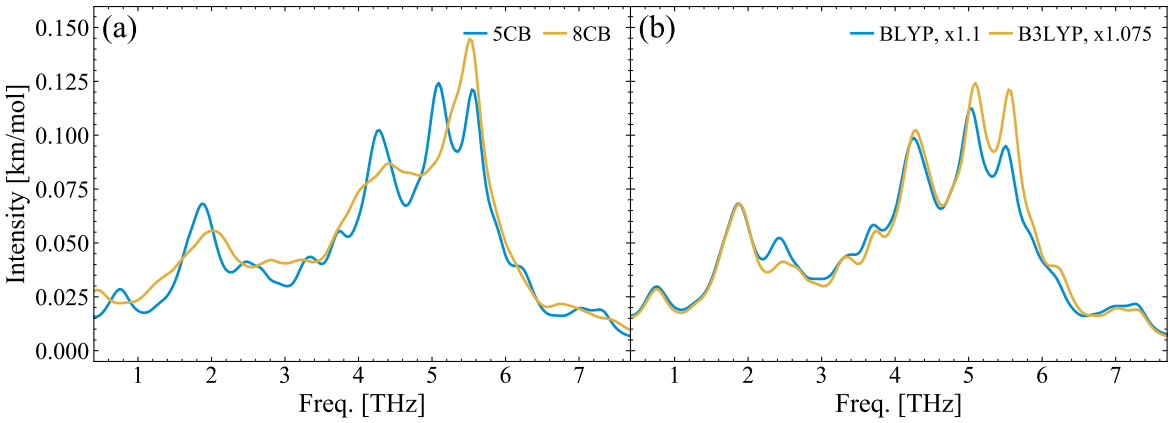

*Figure 3.17.: (a) B3LYP-D3/6-311++G** singe molecule harmonic spectra intensity for 5CB (blue) and 8CB (yellow). The frequencies have been scaled by a factor 1.075. The spectra shown here have been obtained as a weighted average by the Boltzmann populations (at 323 K) of the set of computed ordinary spectra. (b) BLYP-D3 (blue) and B3LYP-D3 (yellow) 5CB harmonic spectra (6-311++G** basis set in both cases). The frequencies are scaled by different factors to match the experimental trace: BLYP-D3 by a factor 1.1, B3LYP-D3 by a factor 1.075. The spectra shown here have been obtained as a weighted average by the Boltzmann populations (at 323 K) of the set of computed spectra.*

and these groups are the same between the two molecules. However, the length of the tail still gives non-negligible effects on the spectra, modulating the spectral appearance, in particular in the region above 4 THz. The modes of this spectral region are always delocalized on the whole molecule and the number of CH_2 units modifies the couplings between phenyl ring and alkyl chain. In general, the features of 5CB are more narrow compared to the ones of 8CB. The region below 3.5 THz instead a spectral broadening in the computed spectra, but not significant changes between 5CB and 8CB. Therefore, 5CB has been considered a good enough model as a compromise for the computational cost to study the effects of the intermolecular interactions on this region for all the nCB.

3.4.3.2. Dimer and trimer computation

Due to the computational cost, for the 5CB dimer and trimer calculations, the structures with an energy more than 2 kcal/mol from the global minimum have been discarded. Furthermore, another change made in order to keep the computational cost under control is the use of a simpler functional. Figure 3.17b compares the 5CB single molecule gas-phase harmonic spectra computed with the BLYP functional and the B3LYP functional (Gaussian16 code [112], 6-311++G** basis set, Grimme D3 dispersion term [116]). The main difference between the two descriptions is a general shift of the modes in the BLYP spectrum compared to the B3LYP one. Apart from these, the BLYP functional and B3LYP functional predictions are similar for the spectral range under consideration.

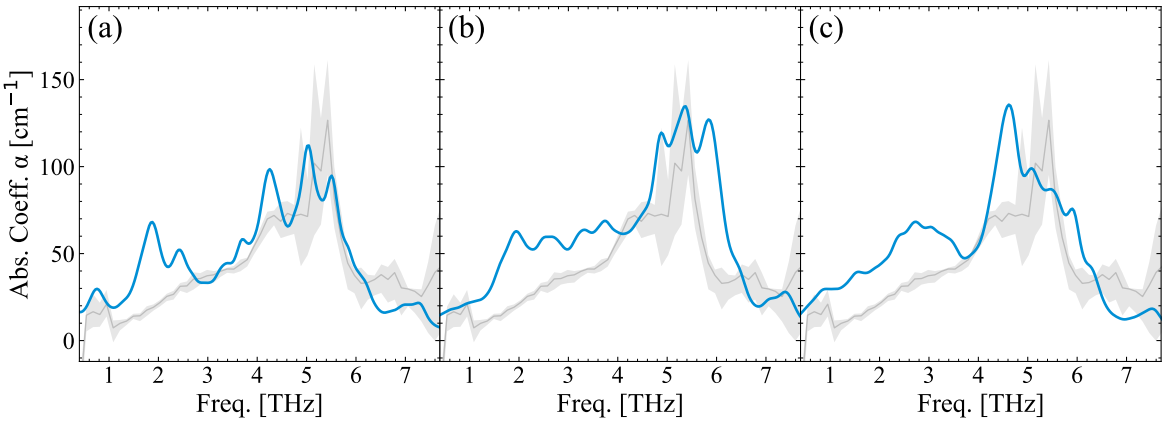

*Figure 3.18.: Full traces of (a) monomer, (b) dimer, and (c) trimer 5CB cluster calculated harmonic spectra (BLYP-D3/6-311++G**). In each case the isotropic measurement result is included in the background (light grey) for additional comparison to the experiment. The computed intensities have been normalized on the strongest mode. The frequencies have been scaled by a factor 1.1. The spectra shown here have been obtained as a weighted average by the Boltzmann populations (at 323 K) of the set of computed spectra.*

Therefore, in the case of the 5CB cluster calculations (dimers and trimers), the BLYP functional has been preferred to the more expensive B3LYP one.

3.4.3.3. Alignment weighting

The full calculated cluster spectra, zoomed out to the full range under investigation, are shown in Figure 3.18. It is evident, that in addition to the low THz mode, also the modes at higher frequency change. The comparison of Boltzmann weighted computed spectra and the experiments above 4 THz get worse with the dimer and trimer clusters. However, this effect is due to the artificial arrangement of the molecule in the clusters, due to the gas-phase calculations that do not reflect the molecular order in the bulk LC condensed phase. The intermolecular arrangement is governed in this system by the balance between the (anisotropic) Van der Waals intermolecular interactions, the dipole interactions (that favor an antiparallel configuration), and the ring stacking (that requires that the rings face each other). In a real bulk LC condensed phase, the molecules can orient themselves in antiparallel configurations without penalizing the Van der Waals interaction between the chain, and therefore they preferentially do it even in the isotropic phase [117].

Unfortunately, in small clusters instead, these three driving forces are competitors. In the final balance between them, the antiparallel arrangement is partially (dimers) or totally (trimers) lost for most of the clusters. To qualitatively validate this hypothesis, instead of using the Boltzmann weights, also average spectra are computed using the degree of "antiparallelness" as weight. These spectra are presented in Figure 3.19. The

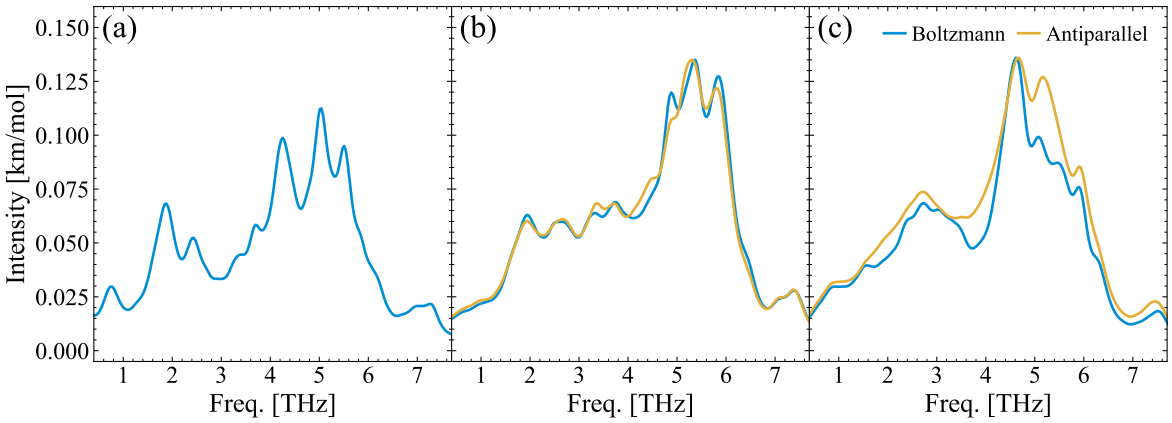

Figure 3.19.: Boltzmann (blue) and antiparallel weighting (yellow) distributions for the monomer (a), dimer (b), and trimer (c) cluster calculations at BYLP-D3 level. The Boltzmann results are given in absolute units, while the antiparallel traces are normalized to the maximum Boltzmann values. The frequencies are scaled by a factor 1.1.

degree of "antiparallelness" has been defined as

$$w = \exp(-(\cos 180^\circ - \cos\theta)) \tag{3.29}$$

for the dimers and

$$w = \exp(-(\cos 180^\circ - \cos\theta_1))\exp(-(\cos 180^\circ - \cos\theta_2))\exp(-(\cos 180^\circ - \cos\theta_3)) \tag{3.30}$$

for the trimers, where θ_i is the angle between the rings of the two molecules. From Figure 3.19 one can see, that while the low THz mode remains largely unaffected, the high-frequency (4 THz to 6 THz) components are substantially modified (especially for the trimer case, since the dimer configuration already approaches the antiparallel arrangement by itself) towards closer resemblance with the original traces.

3.5. Transient birefringence

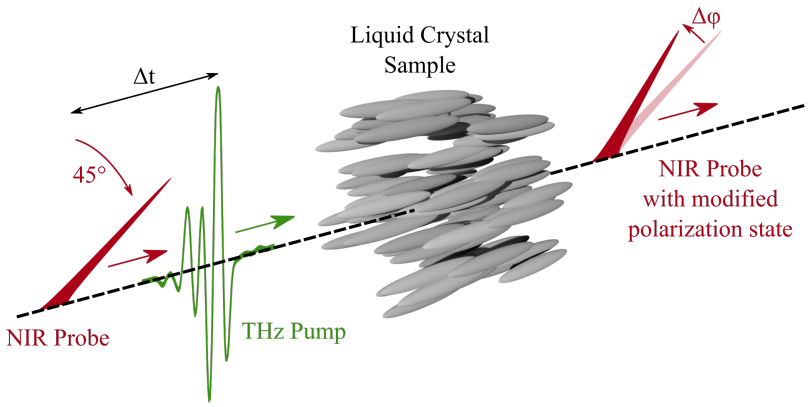

Figure 3.20.: THz transient birefringence scheme. The THz pump and NIR probe beams co-propagate through the LC sample (LC director along the propagation axis, as depicted) with variable time delay Δt. The THz induced birefringence in the sample imprints a phase shift on the initially linearly polarized (45° to the THz polarization) probe, which is detected in balanced detection configuration.

The Transient birefringence scheme is presented in Figure 3.20 and the experimental configuration [21] is shown in Figure 3.21. Here, the role of the THz beam is that of a pump pulse. Its purpose is to act as a strong and resonant drive of the dynamics under investigation. These will then be sampled by the gate, and detected via the same balanced detection line as in the TDS configuration. Hence, bulk changes of the LC material in the interaction region and, specifically, their impact on the polarization state of the NIR probe pulse, are investigated.

In this experimental scheme, the role of the THz pulses propagating through the sample is changed. Where in the case of the TDS experiment, the THz pulse is a weak probe that encodes the spectroscopic information, in this experiment it acts as a strong pump inducing some dynamics in the sample, that is then read out by a probe as a function of time delay. Therefore, conceptually it is a classical pump-probe scheme, where the choice of the probe and its readout dictate what dynamical sample information can be extracted.

Here, the choice is to look at bulk vibrational dynamics, since they are expected to occur at THz frequencies and since it provides a complementary picture to the information extracted form the TDS experiments. With this in mind, the probe is taken from the TDS EOS line via a flip mirror for rerouting and reused here in order to measure the sample dynamics directly. Also, the detection of the probe is the same as in the EOS measurement, where the balanced detection line is used without changes. This allows for very simple changes between measurement schemes within the same setup.

The THz pump and the NIR probe pulses have the following roles in this experimental scheme. The THz pulse interacts with the sample and induces some dynamics of

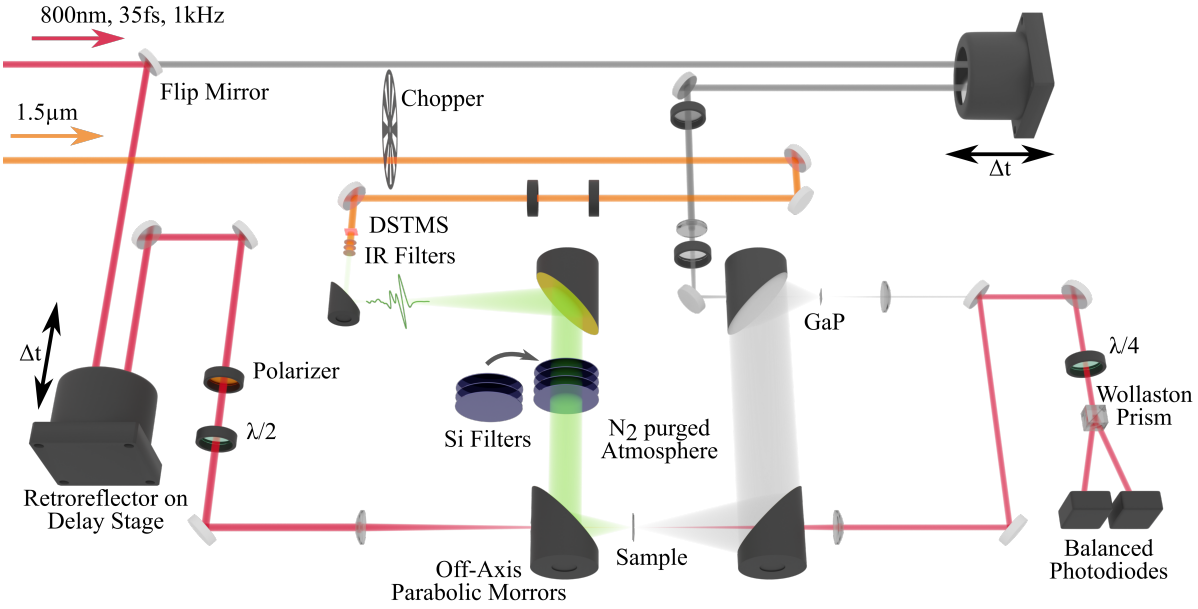

Figure 3.21.: THz Setup for Transient THz Kerr Effect spectroscopy. The optics and beams used for this measurement technique are highlighted in color, while the unused parts are grayed out.

electronic and nuclear nature. Since the target is to investigate the effect of the THz interaction with the molecules on the macroscopic material response, the choice here is to measure the induced birefringence, which is read it out via balanced detection of the probe. In other words, the THz induces transiently a change in the refractive index along its polarization axis that leads to a birefringence Δn referenced to the axis perpendicular to the THz polarization. The probe is most sensitive to this induced birefringence, if its linear polarization is set 45 ° to the THz polarization, which leads to changes in phase $\Delta\varphi$ (hence ellipticity and rotation) of the co-propagating probe, proportional to Δn. The balanced signal ΔI is related to Δn by

$$\frac{\Delta I}{I} = \sin \Delta\varphi = \sin \frac{\Delta n \omega L}{c} \tag{3.31}$$

3.5.1. Rotational diffusion model

In the following, the expected dynamics of these experiments will be discussed in analogy to already existing THz Kerr models for liquid state samples. The response for centrosymmetric systems (the case for the LC alignment imposed in this experiment) can be understood as a third order effect, in which the refractive index is modified by $\Delta n = n_2 I(\omega) = \frac{3\chi^{(3)}(\omega)}{4n_0^2\epsilon_0 c}|E(\omega)|^2$, which is a consequence of the third order nonlinear polarizability $P^{(3)}(t) = \chi^{(3)}E^3(t)$ of equation 3.1 [87]. In solid state systems, this can be

understood as originating purely from nonlinear electronic polarizablity. Liquids, due to their molecular degrees of freedom, can show more complex behavior. Typical models account for electronic and nuclear processes as independent contributions that are both generated by the instantaneous electric THz field [21, 24].

The electronic effects remain of the same form as expressed above. The process is described as a χ^3 process that is proportional to $E^2_{\mathrm{THz}}(t)$, which is supposed to represent the instantaneous electronic polarizability of the system. Here, it is generated from the ensemble molecular polarizability in the bulk.

The nuclear part is assigned in order to account for relaxation processes of the liquid medium on time scales longer than the presence of the THz driving field. Typically, these are related to rotational diffusion processes, in which the molecules are driven out of equilibrium, and then relax back through rotational Brownian motion. Theoretical models are using the Langevin equation as a starting point [118,119] (equation of motion under stochastic forces) to model this behavior, and include dipole and polarizability interactions in order to account for the THz driving. In practice, this process is expressed in the form of an exponential decay that contains the relaxation constant after the THz electric field has driven the system.

The full expression for the induced transient birefringence takes the following form, where equation 3.32 accounts for the electronic part, and equation 3.33 and equation 3.34 account for the nuclear part on two independent timescales, accounting for the strong anisotropy of the molecules under investigation [21].

$$\Delta n(t) = n_2^e E^2_{\mathrm{THz}}(t) \tag{3.32}$$

$$+ \frac{n_2^{o_1}}{\tau_1} \int_{-\infty}^{\tau} E^2_{\mathrm{THz}}(t) e^{-(\tau - t)/\tau_1} d\tau' \tag{3.33}$$

$$+ \frac{n_2^{o_2}}{\tau_2} \int_{-\infty}^{\tau} E^2_{\mathrm{THz}}(t) e^{-(\tau - t)/\tau_2} d\tau' \tag{3.34}$$

In order to separate the individual terms, it is of absolute necessity to know the exact THz wave form in the interaction region, since E^2_{THz} contributes to each term. Here this is accomplished by independent THz EOS measurements using 50 µm thick GaP crystals in the sample position, prior to the THz Kerr effect measurements. The measured traces are then corrected as described in section 3.1.2.

3.5.2. Balanced detection in the context of Kerr geometries

The balanced detection line from the EOS setup is then sufficient to read out the change in polarization. Only one subtle difference to the EOS configuration requires discussion. In the EOS setup the unperturbed probe polarization propagates into the waveplate at vertical or horizontal polarization, which makes the relative settings of the waveplate and Wollaston clear (as discussed in section 3.1.2), and the photodiode values easy to interpret. On the other hand, here a balanced settings of the photodiodes could mean either circular polarization after the waveplate (so 45 ° to the reference frame of the

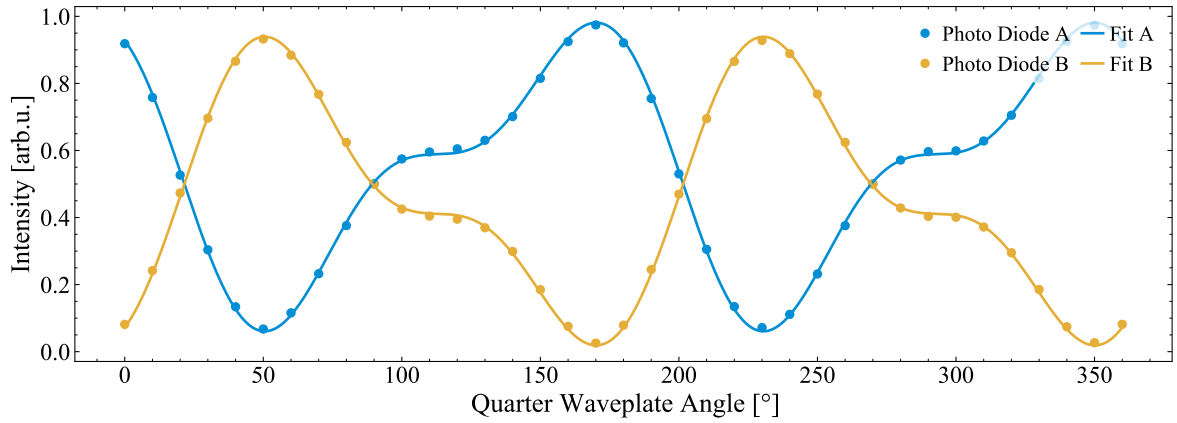

Figure 3.22.: Intensities measured by each photo diode involved in the balanced detection, as function of quarter waveplate angle (dots), and the fit to the data by the Jones matrix formalism (lines). The polarization state is created by a planar aligned 5CB sample in the beam path.

Table 3.2.: Expected and retrieved LC parameters from the ellipsometry fits

Case	Thickness d [µm]	Birefringence Δn	Angle α [°]
expected	23	0.1576	45
fit A	23.966	0.145	30.071
fit B	21.796	0.159	30.071

probe polarization, or horizontal and vertical in the lab frame), or unchanged linear polarization at 45 ° (meaning the waveplate is set to have one of its axis coincide with the polarization direction of the probe, or 45 ° in the lab frame). It would be intuitive to keep the relative angles consistent with the EOS setup. On the other hand, the detector response should be verified. Literature on THz Kerr measurements is often neglecting this subtlety, and in the cases where it is explicitly mentioned, different sources employ different techniques (insertion of additional optical elements for compensation [120] or relying only on the quarter waveplate [121]).

In order to verify the impact of the waveplate setting, the balanced detection scheme is modeled with the Jones matrix formalism [87]. In this framework, the impact of optical elements on the polarization state of propagating light can be modeled using 2 by 2 matrices. The polarization state itself is expressed as a complex 2 component vector P, with each component expressing the x and y direction of the light field. The propagation of the light through one element is expressed by the multiplication of matrix with vector. A sequence of optical elements is a chain of matrix multiplications. In this framework, the balanced detection scheme in its simplest form, is expressed as as propagation through

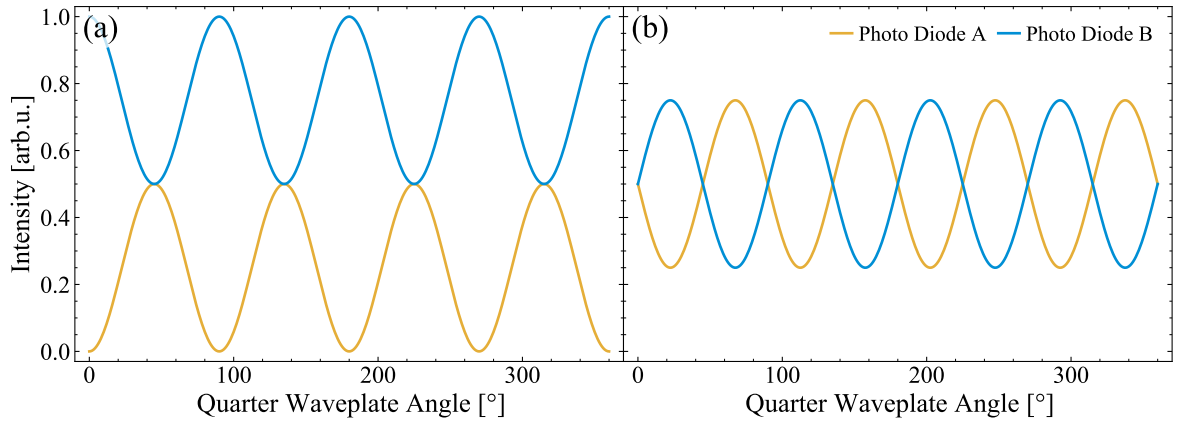

Figure 3.23.: Photo diode intensities modeled for the balanced detection scheme as a function of quarter waveplate rotation, for (a) vertical linearly polarized incoming light, and (b) at linear polarization at 45° angle.

a rotated (Rotation matrix R) quarter waveplate Q, as expressed below.

$$P_{\text{out}} = R(\theta) \cdot Q \cdot R(-\theta) \cdot P_{\text{in}} \tag{3.35}$$

with

$$P_{\text{in/out}} = \begin{pmatrix} E_{\text{x}} \\ E_{\text{y}} \end{pmatrix} \tag{3.36}$$

$$Q = \begin{pmatrix} 1 & 0 \\ 0 & \exp(i\pi/2) \end{pmatrix} \tag{3.37}$$

$$R(\theta) = \begin{pmatrix} \cos(\theta) & \sin(\theta) \\ -\sin(\theta) & \cos(\theta) \end{pmatrix} \tag{3.38}$$

The splitting by the Wollaston Prism is handled by selecting either the x or y component of the calculated polarization vector, and the detection by the photo diodes as taking the square of this complex number. Scanning the rotation angle θ is then equivalent to rotating the waveplate.

In order to test this formulation on the real setup, the polarization state has been set to an arbitrary value, measured as function of waveplate angle, and used as input for a fit of this formalism. The polarization state was set by exploiting the known birefringence of the LC samples. A 23 µm thick cell of planar aligned 5CB was set to roughly 45 ° angle with the incoming polarization. All parameters in the fit were left free. The results are plotted in Figure 3.22, where measured data and fit are matching well, visually and in terms of extracted parameters, as presented in Table 3.2. (note, that the angle of rotation of the sample is the one parameter not fitting well, which is reasonable, since the sample was placed visually.)

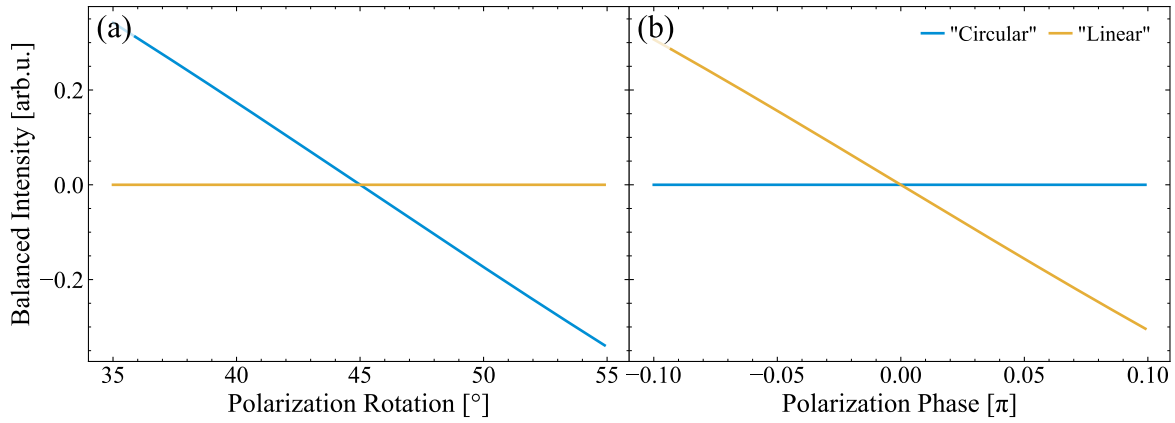

Figure 3.24.: The balanced intensity (difference of the intensities between photo diode A and B) plotted as a function of the polarization state of the light propagating into the quarter wave plate. The "circular" (in blue) condition denotes the cases, in which the quarter wave plate is set to convert the linear 45° state into circularly polarized light. The "linear" (in yellow) condition denotes the cases in which the linearly polarized light is propagating along one of the axis of the birefringent waveplate, in other words it is left unchanged. Panel (a) shows the signal behavior for a change in rotation of the initial polarization, Panel (b) for a change in ellipticity of the initially linearly polarized light. All curves are the numerical solution of the Jones matrix formalism described in the main text.

With the model confirmed to be a sufficient description of the balanced detection scheme, now the focus is on understanding the behavior under different rotation and ellipticity conditions. Figure 3.23 shows the detected intensities for horizontal and 45 ° polarized light, as discussed above. In panel a, every intersection of intensity A and B represent circularly polarized light after the waveplate. In panel b, circular and unaffected 45 ° polarization are alternating at every consecutive intersection. The question is now how the balanced signal scales with a change of the incoming polarization state for each of these two possible settings. In Figure 3.24a, the incoming linear polarization angle is varied, and in panel b the ellipticity is increased.

Therefore, through numerical Jones matrix modeling, the conclusions are the following: Case one is sensitive explicitly to the rotation of the probe polarization, whereas case two is sensitive to the ellipticity of the probe. This realization is valuable, since it allows the explicit measurements of both cases individually only through the setting of the rotation of the waveplate in the beam path.

There is one practical consequence to the relative polarization angles of THz pump and NIR probe in the Kerr geometry. The 45 ° angle means, that for planar LC alignment, always at least one of the two pulses experiences birefringenece when propagating through the sample, as evidenced by the highly elliptical polarization state after a planar 5CB sample shown in Figure 3.22. To mitigate this problem, for the purposes of this work presented here, all samples in the transient birefringence experiments will be

aligned homeotropically, meaning the extraordinary axis is aligned along the propagation direction of both beams. As a result, all polarization angles are accessible, because the sample is optically isotropic, but only the ordinary axis will be investigated, and the extraordinary neglected. The details about the sample delivery will be discussed in the following chapter 4. Furthermore, only the induced ellipticity will be measured, since the rotation measurements give negligibly weak amplitudes.

4. Sample delivery

Liquid Crystals have the special ability to arrange in mesophases with a particular orientational and positional order, depending on the right conditions, such as temperature. For the samples presented here, the static alignment is controllable, a key parameter in the present investigation, as introduced in chapter 2. Since the molecules retain their macroscopic bahavior of liquid flow, they need to be contained in the interaction region and actively forced to align along the desired direction. Hence, custom made cuvettes or cells are needed, fulfilling a number of conditions in order to qualify as suitable. This chapter will give an overview over the different cells deployed, how the samples are aligned within the cells, and how their temperature is controlled. Here, each experiment has different requirements in terms of cell preparation. Both cell types will be discussed separately.

4.1. Window materials

In order to contain liquid state samples, commercial cuvettes are readily available, but only compatible with standard spectral regions, such as the UV-Vis experiments. In order for a window material to be compatible with the intended THz experiments, it must meet the following requirements:

- THz transparency within the working bandwidth, with a preferably high transmission coefficient.
- NIR transparency in the case of the THz Kerr Effect experiment, and should show minimal contribution to the acquired data.
- Resistance to the temperature ranges required to reach all LC mesophases of the samples under investigation.
- Additionally, transparency in the visible range is preferable, because it allows for inspection of the LC alignment via optical microscopy, before performing the experiments.

Typical window materials for THz spectroscopy are quartz, diamond, or Silicon Carbide (SiC) [122]. Quartz, while it is an affordable and commonly available material, does not cover the full bandwidth of the experiments, since it has a dipole active phonon at 4 THz [123], and a non-negligible electro-optic coefficient, making it unsuitable for both experiments. Diamond is prohibitively expensive, rendering it highly incompatible with fabrication in large quantities and iterations of different test cell designs. SiC is a good

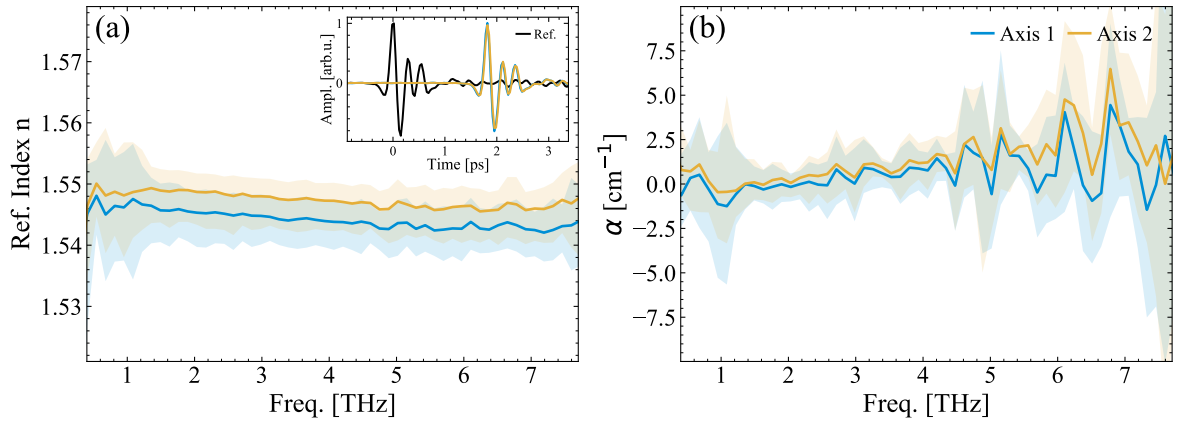

Figure 4.1.: Time Domain Spectroscopy results of an isolated TOPAS window. The measurement has been conducted on two perpendicular axis of the same window, in order to exclude possible birefringence. (Motivated by the appearance under the polarized light optical microscope. The window itself shows optical activity in the visible spectrum. This property probably originates from the injection molding manufacturing [125].) (a) Extracted refractive indices, showing a flat trend at $n = 1.545$. (b) The corresponding absorption coefficients, showing no loss within the uncertainty. The inset in panel (a) shows the raw THz traces, highlighting the high transmission.

candidate, but has only acceptable transmission coefficients, given it's relatively high THz refractive index.

4.1.1. TDS window material choice

The material of choice for the TDS experiments here are low density polymers, with glass-transition temperatures above 100 °C. Possible option are Polymethylpentene (TPX), Polyethylene (PE), Polytetrafluoroethylene (PTFE, Teflon), and Cyclic Olefin Copolymer (COC) [122,124]. The choice is TOPAS, due to its availability in suitable dimensions and surface quality finishes. The windows are bought in wafers of dimensions of 1 mm thickness and 10 cm diameter, and cut into square pieces as needed.

TOPAS (ambiguous with the name TOPAS of the commercial *Light Conversion* OPA system, Chapter 3) is a trade name of a COC polymer. It has a high THz transmission value and a flat refractive index (no dispersion) over the entire available THz spectrum. Furthermore, it is fully transparent in the visible spectral range. Figure 4.1 presents the TDS results of a TOPAS window, showing a flat negligible absorption loss and refractive index.

4.1.2. THz Kerr window material choice

The selection of the window materials for the THz Kerr effect measurements presented challenges, as early measurements with SiC had the signals dominated by the response

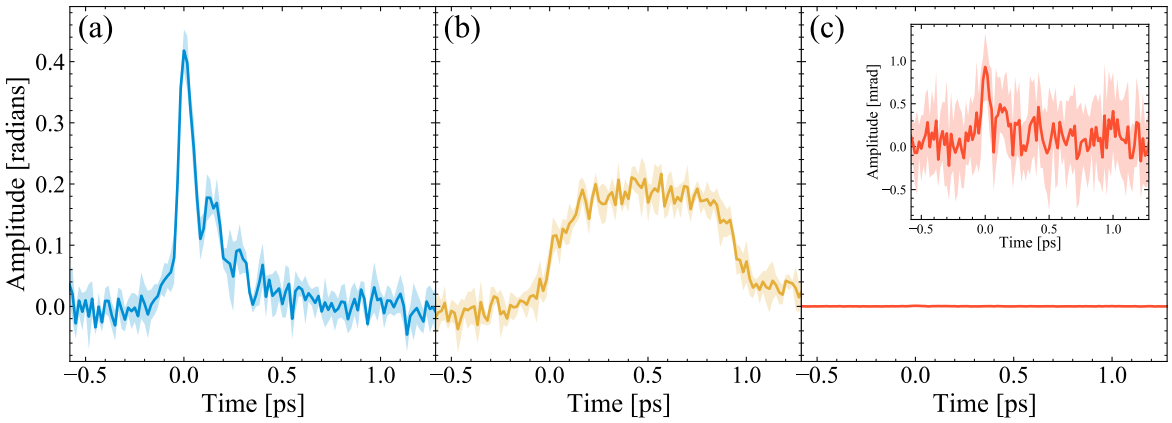

Figure 4.2.: THz Kerr traces for three representative window materials: (a) TOPAS polymer of 1 mm *thickness (b) SiC window of* 0.5 mm *thickness (c) SiN membrane of* 500 nm *thickness. The inset of panel (c) shows the same data on zoomed in scale. (The improved signal to noise in panel c compared to a and b is due to separate measurements with improved snr.)*

of the window itself, mainly due to the larger window thicknesses compared to the LC sample layers. The expected traces fall into two possible categories: (i) a phase matched response, or (ii) response curves generated by large velocity mismatch between THz and probe pulses, systematically characterized by Sajadi *et al.* [124].

(i) In the first case, the expected response follows the square of the THz electric field, and is conceptually equivalent to probing the electronic polarizability of the material. (ii) The second case is probing the same property, but additionally the relative velocity mismatch plays a role. It expresses itself as a cross-correlation of both pulses, and for sufficiently large velocity mismatch, the result is a square shape signal in time, where for every setting of the relative time delay before entering the sample, the probe pulse is integrating over the entire THz pulse.

Figure 4.2 shows three such cases, measured in the same setup as the Liquid Crystal experiment. The TOPAS window material, which is the material of choice for the TDS experiments, a SiC wafer as an alternative option, and a nanometric SiN membrane. These traces represent a replication of the findings by Sajadi *et al.* [124] and confirm the unsuitability of the first two examples. The TOPAS and the SiN traces, which barely rises above the noise floor, are examples of velocity matched responses, while the SiC trace represents the velocity mismatched response. The reason the SiN signal is weak lies in the thickness of the window compared to all other options. With 500 nm in depth, it is 3 orders of magnitude thinner than other options available (minimum 500 µm), or the samples investigated in the experiment itself (100 µm).

SiN membranes are available off the shelf, since they are standard consumables in TEM microscopy applications. These materials have remarkable strength given their dimensions, which allows for cell fabrication. They are manufactured by deposition of nanometric layers of SiN on a silicon wafer, which is locally removed by etching, leaving

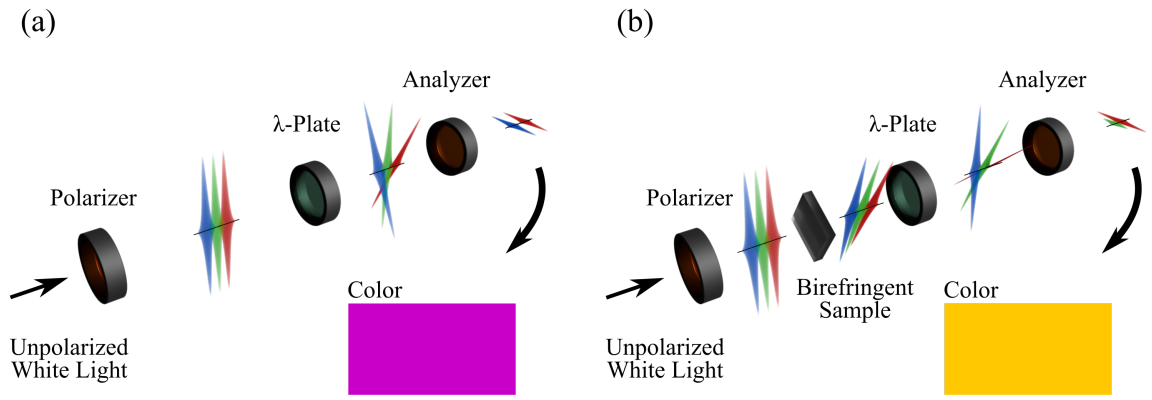

Figure 4.3.: Polarized light optical microscopy working principle, consisting of polarizer, λ-plate, and analyzer. For simplicity only the red, green, and blue component of the visible spectrum and only linearly polarized beams are depicted. (a) POM without birefringent sample, where the green part of the spectrum is fully filtered out, making the output appear magenta. (b) A birefringent sample adds phase to the beams, shifting the color spectrum after the analyzer.

a free standing window of solely SiN. This way, they come on a helpful solid and large Si frame with a small window area, allowing robust handling and processing without danger of damage to the membrane [126–128].

4.2. LC alignment

In the present experiments, large and aligned mono-domains are desired. Multiple pathways are available to achieve this goal. For practical reasons that will be elaborated in the appropriate sections, in each of the two experiments the alignment is achieved differently. In the TDS experiments, field alignment is preferred. In the THz Kerr experiments the choice is surface anchoring. In order to characterize the manufactured samples and alignment, polarized light optical microscopy is performed, and each cell is checked visually before it is used in the experiments.

4.2.1. Polarized light optical microscopy

Polarized light optical microscopy (POM) is a standard technique for birefringence analysis (such as for LCs or geology). It is based on a normal transmission microscope design but includes additional polarizing optical elements along the beam path. The recorded images reveal the birefringence of the sample by the color of the light transmitted through the optical system [129].

The general working principle is outlined in the scheme depicted in Figure 4.3. Polarizing microscopes include a polarizer before the sample and an analyzer (polarizer in

extinction orientation to the first polarizer) after the sample, leading to zero transmission across the visible spectrum in case no birefringent sample is placed in the path. Secondly, between sample and analyzer, a λ-plate is mounted with its optic axis oriented 45° to the polarized light. This optical element is a wave retarder of exactly one wavelength for only the green component of the visible spectrum, and slightly detuned in the remaining spectrum. As a consequence, the green light remains unaffected by the λ-plate and is blocked by the analyzer. All other components experience leakage through the analyzer, depending on their exact retardation. The light exiting the analyzer will thus appear magenta, indicating no birefringence. In the case a birefingent sample is mounted in the light path, the retardance of the sample is added to the one of λ-plate, and the total accumulated phase dictates the new color appearing after the analyzer. In simple terms, the color encodes the birefringence of the sample if the thickness is known, or the other way around. In order to make quantitative statements, an interference color chart (also known as Michel-Levy chart) can be consulted.

Here, a quantitative description of the samples in terms of static birefringence is not of interest. Instead, the quality of the alignment (in terms of direction and homogeneity) of the samples is checked before placing into the interaction region of the THz setup. Magenta indicates unchanged polarization, meaning isotropic sample, or sample mounted with one of it's principle axes along the polarization direction. If the sample is turned from these initial conditions, the transmitted color spectrum shifts towards yellow or blue, depending on the direction.

4.2.2. Field effect alignment

Aligning the LCs with electric fields has the advantage that no additional polymer alignment layers are introduced in the beam paths. Nonetheless, in order to accommodate the tighly focused and strongly diverging THz beams, the electrodes need to be rather far apart. As a consequence, the required applied electric field strength scales up accordingly.

The alignment conditions for the LC cells used in the TDS experiments are the following: An AC sine voltage at one 1 kHz is applied over electrode distances of roughly 2 mm. Thus, the electric field strength is on the order of 1 V/µm. The electrodes are standard wires of defined 0.5 mm diameter and placed parallel to each other. The beam is passing through the electrode gap, perpendicular to the applied electric field lines. Since the electric field lines define the LC director axis, the THz beam is propagating always perpendicular to the long axis of the molecules. The polarization state of the THz beam is one of the degrees of freedom in this configuration, and allows access to the ordinary and extraordinary refractive indices, depending on the relative cell and polarization orientations.

4.2.3. Surface anchoring

Imposing bulk alignment through surface anchoring is a standard technique in LC applications. Once the surface layer is aligned, the collective ordering propagates into the

bulk via nearest-neighbor interactions. The drawback is in the achievable thicknesses, since it is not infinitely scalable and alignment can turn out to be rather loose in the center of particularly thick samples. In the experiments performed here, the cells which have been treated in this way are 100 µm thick, which still gives reliable alignment as checked under the polarizing microscope.

Two alignment configurations are possible, planar and homeotropic. For reasons outlined in section 3.5, the measurements reported here. which rely on surface anchoring, are only measured in homeotropic configuration in which the LC director is pointing perpendicular to the window plane. The procedure for homeotropic LC alignment is based on the deposition of DMOAP (N,N-dimethyl-n-octadecyl-3-aminopropyltrimethoxysilyl chloride). The cell windows are treated in a step wise fashion:

1. UV-ozone treatment: A 15 + 30 minute (UV on, then off) cleaning in a UV-ozone oven of the SiN cell windows as received from the manufacturer.

2. DMOAP bath: 10 min under constant gentle stirring in 2 wt.% solution of DMOAP in milli-Q water (DMOAP from *Sigma Aldrich* comes as 42 wt.% solution in methanol. Therefore 10 g are dissolved in 200 g milli-Q water).

3. Removal from the bath and cleaning of residual DMOAP solution by dipping in pure milli-Q water. Careful attention is paid to not leave any wetted surface intended for the THz investigations when removing from the water bath.

4. Baking for 10 min at 120 ° C.

4.3. Polymer cell for TDS

The sample cells for the TDS investigation are build from TOPAS polymer, and aligned through application of AC electric fields. Their diameter, and therefore the sample thickness, is chosen to be 500 µm, exploiting the dynamic range of the THz spectrometer. The detailed steps for cell construction are outlined below. First, the substrates undergo thorough cleaning, in order to avoid contamination. In detail, the cleaning steps are listed below.

1. Sonication in Alconox soap solution (10 g/L) for 30 min.

2. Rinsing in deionized water.

3. Potassium hydroxide (KOH) Base bath for minimum 2 hours (60 g KOH in 200 g milli-Q water and 800 g ethanol).

4. Sonication in milli-Q water 3 times for 5 min.

5. Sonication in acetone for 10 min.

6. Blow drying with nitrogen.

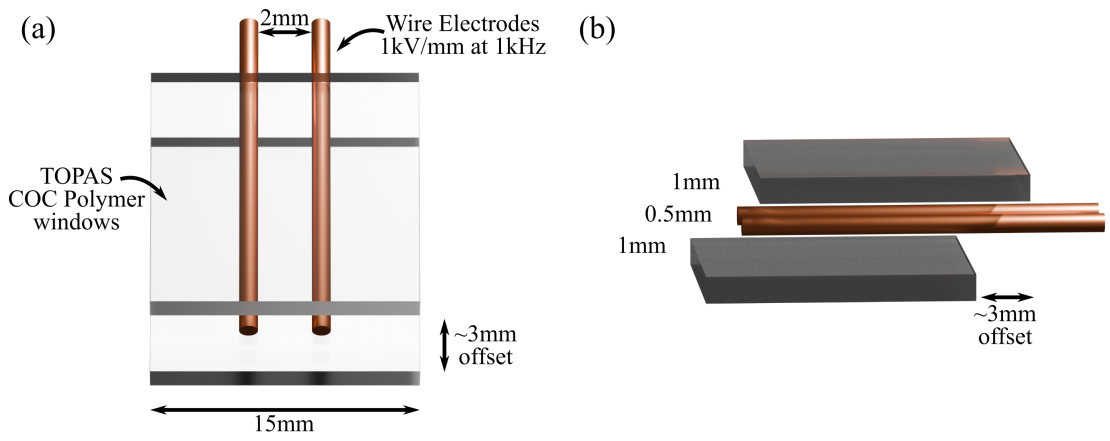

Figure 4.4.: Schematic representation of the TOPAS polymer cell design, in (a) top down view, and (b) side view.

7. Sonication in isopropanol for 10 min.

8. Blow drying with nitrogen.

Once all materials have undergone these steps, the electrode cells are build as described in the following list. In addition, Figure 4.4 depicts a schematic representation of the overall geometry as presented in the text.

1. Cleaning of the electrodes (sonication in isopropanol and wiping with isopropanol drenched tissue).

2. Placing of the electrodes on top of window 1 in the geometry described in section 4.2.2.

3. Placing of window 2 on top of the electrodes with a few mm offset along the long axis of the electrodes. This geometry forms a staircase-like step at the entrance of the cell, which assists cell filling later on.

4. Clamping of the structure into fixed position.

5. Gluing of the structure. Two-component resin is used to fill the empty space formed between the windows outside of the electrodes. Capillarity makes the resin fill the entire volume easily, fixing the relative positions permanently.

6. Soldering of insulated connectors/wires to the exposed electrodes, in order to apply the electric fields.

7. Filling of the cell with the sample material. The LC is heated to its isotropic phase, and picked up with a clean glass capillary. Meanwhile, the cell is heated as well on a hot plate. The material is deposited at the cell opening, and it enters the cell through capillarity.

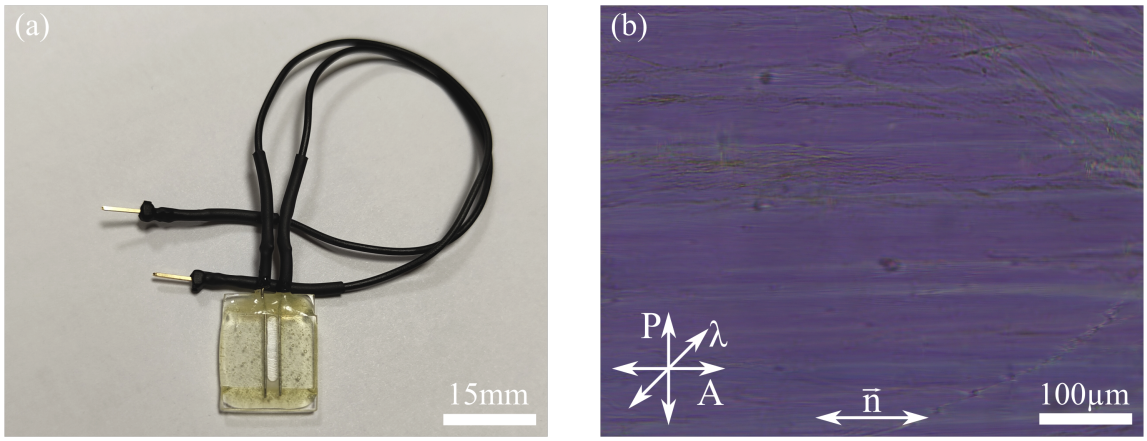

Figure 4.5.: (a) Photograph of a final TOPAS cell, and (b) A POM image of a smectic sample contained within the SiN cell.

8. Sealing of the cell. The cell is taken off the hot plate, and once the LC has thermalized back to room temperature the cell is closed with the same glue that was used previously.

Figure 4.5 provides photographs of a real life example in panel (a) and a representative POM image in panel (b) showing the aligned mono-domain nature of the sample in smectic A phase.

4.4. SiN cell for THz Kerr spectroscopy

The cells, as presented in this section, are optimized for the THz Kerr effect measurements with their negligible window response under the experimental conditions. The Liquid Crystals are aligned through surface anchoring with DMOAP application as discussed in section 4.2.3. Figure 4.6 gives a schematic depiction of the cell design, and contextualizes the cell building description presented here.

In terms of cleaning procedure before construction, no additional steps are taken beyond the UV-ozone treatment outlined in section 4.2.3, in order to minimize the risk of damage, given the fragility of the membranes[1]. The cell construction follows the outline below.

1. Cutting spacers, intended to define the cell gap or sample thickness, out of polymer foil of known thickness. In this case it is Mylar, with thicknesses available from 6 µm to 250 µm, with the experiments here conducted using 100 µm, unless specified differently.

[1]Construction of planar aligned cells has been tried as well. This procedure requires spin coating at 6000 rpm, and rubbing of the surface across a cloth. Nevertheless, the survival rate of theses membranes was remarkably high at about two in three, in the few tests conducted.

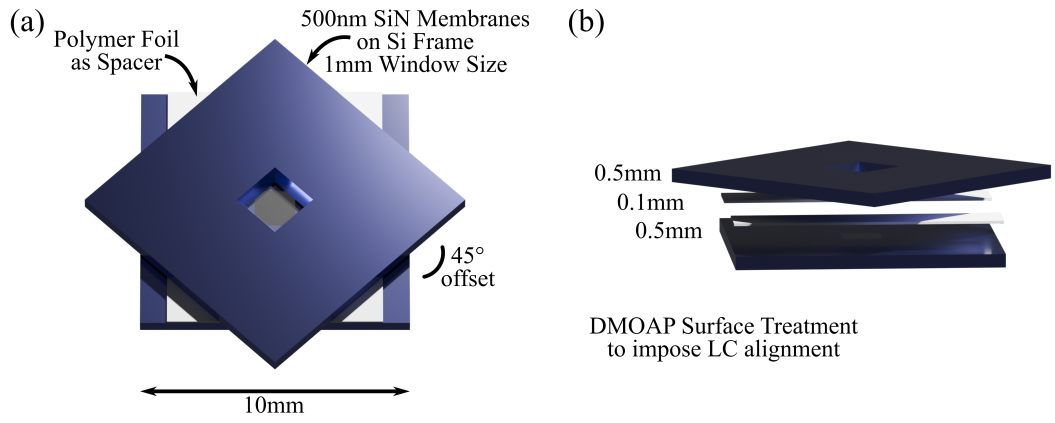

Figure 4.6.: Schematic representation of the SiN membrane cell design, in (a) top down view, and (b) side view.

2. Placing the spacers either side of the SiN window 1, with the gap in between defining the sample volume.

3. Placing window 2 on top of the spacers, rotated 45° around the normal axis of the window. Since the window is centered on the frame, this rotation is intended to create the same stair step offset at the cell entrance, as in the TOPAS cell.

4. Application of a light weight. Clamping is not an option, since this type of stress makes the membranes break easily, even though in any other processing step they show high resistance.

5. Gluing of the construction from all exposed sides, except the two cell entrances, with two-component resin.

6. Filling of the cell with the sample material. The LC is heated to its isotropic phase, and picked up with a clean glass capillary. Meanwhile, the cell is heated as well on a hot plate. The material is deposited at the cell opening, and it enters the cell through capillary forces.

7. Sealing of the cell. The cell is taken off the hot plate, and once the LC has thermalized back to room temperature the cell is closed with the same glue that was used previously.

Figure 4.7 provides photographs of a real life example in panel (a) and a representative POM image in panel (b) showing the aligned mono-domain nature of the sample in nematic phase.

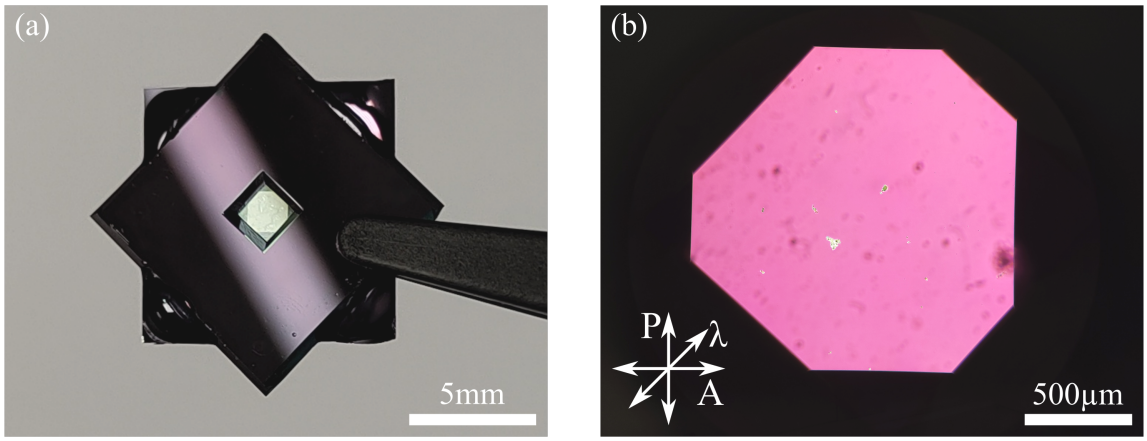

Figure 4.7.: (a) Photograph of a final SiN cell, and (b) A POM image of a nematic sample contained within the SiN cell.

4.5. Temperature and voltage control

One of the key properties under investigation are the behavior of the measured observables, when the order on a molecular level is tuned. This property is accessible via temperature dependent phase transitions. Therefore, in addition to sample confinement and alignment, the sample temperature is controlled over the course of the measurement. For this purpose, the sample cells are mounted within a temperature controlled sample stage. This device used here, is commercially available from *Linkam* as a temperature stage to be mounted in transmission microscopes [130–132]. On one hand, this intended function is also used here to characterize the samples in the polarizing microscope, on the other hand it is additionally mounted vertical in the THz setup, in order to tune the temperature in the experiment. The probe beam, and especially the THz beam, pass through the sample and the few mm hole of the heating stage without clipping.

The Peltier plate in the Linkam stage LTS120E is tunable from $-25\,^\circ$C to $120\,^\circ$C with a stated stability of $0.01\,^\circ$C. The front and back windows are replaceable in principle, but have been removed completely for the THz experiments. All transitions are checked for every sample via POM before measuring. Every time the temperature was set to a new value during the experiment, the sample was given sufficient time to thermalize (minimum 5 min).

This commercial stage comes with electrical feed throughs, but all components are not rated for the fields required here. Therefore, a custom solution has been implemented. The original Lemo connector was removed, and HV-BNC cable inserted. Inside, the connections have been split and terminated at easily attachable connection points for the cell wires. This solution has been tested up to 2.5 kV, well outside the range required. The entire sample assembly is electrically grounded during operation. Figure 4.8a shows the sample stage mounted vertically on a manual 3D translation stage on the optical table, as it is placed inside the THz setup. Panel b shows the inside with a TOPAS cell

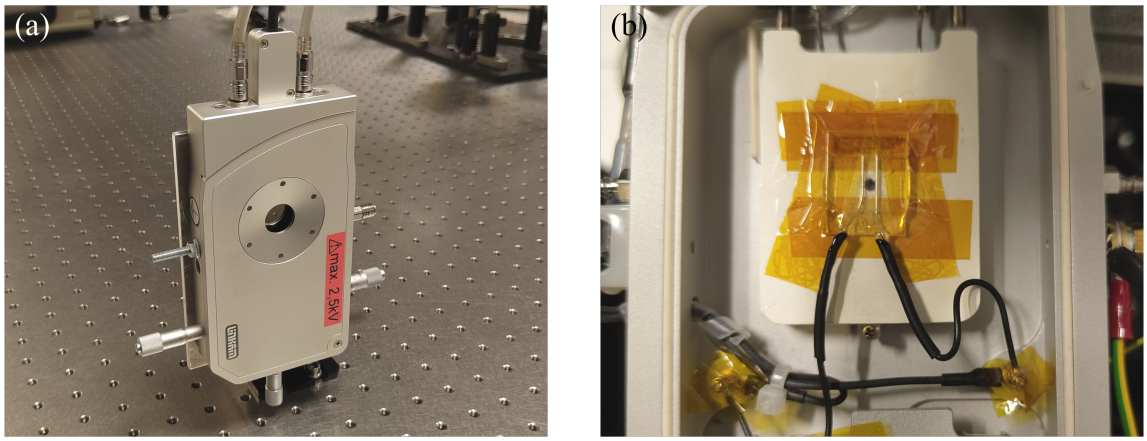

Figure 4.8.: Temperature controlled Linkam stage (a) mounted vertically on the optical table, and (b) inside view with a mounted sample.

wired to the connectors and mounted over the through hole.

5. Results & discussion

In this chapter, the main results will be presented and discussed. the first part of this chapter covers the TDS investigation on the LC samples, and is accompanied by interpretation based on gas phase molecular DFT calculations. Part two discusses the transient THz Kerr effect measurements in terms of two aspects: the standard Kerr response and an additional coherently driven response of the material. A Lorentz oscillator model is providing a conceptual bridge between this driven signal and some of the spectroscopic features seen in the first part of this section.

5.1. Time domain spectroscopy

THz-TDS encodes information of the dielectric properties of the samples under investigation and allows for the extraction of the refractive indices and the absorption coefficients, as outlined in Section 3.3. Here, the samples of interest are 8CB, 8OCB, and PCH5, which share structural similarities, as shown in Figure 2.5. With the sample cell design, as outlined in Section 4.3, both the extraordinary axis (polarization along the long molecular backbone) and the ordinary axis (polarization perpendicular) are accessible.

5.1.1. THz refractive indices

The refractive indices spanning the available THz spectrum of 8CB, 8OCB, and PCH5 are reported in Figure 5.1 for both ordinary and extraordinary conditions within the same panel. The traces are measured for different temperatures, spanning all liquid crystal phases that each sample possesses. Extraordinary (dashed lines) and ordinary (bold lines) indices are plotted in the same color, with the extraordinary result lying at the higher value of both options. The measured conditions are isotropic (red), where both measurements are equal within the uncertainty as expected, the nematic (yellow) and smectic (green) LC phases, and a measurement at a temperature corresponding to the crystalline phase (blue). This temperature setting represents the crystallized system, although crystallization was not observed under the optical microscope, except for 8OCB, where the crystal was strongly non-uniform and therefore no measurement was possible due to scattering.

The retrieved refractive indices are on the order expected for low-density organic materials, such as polymers like the TOPAS window material of the sample cell. Other materials can show significantly higher values, such as silicon with $n = 3.5$. The measured values fall in the range between $n = 1.5$ to 1.8, depending on the sample, temperature and axis. The associated birefringence values fall within the range of $\Delta n = 0.1$ and 0.2,

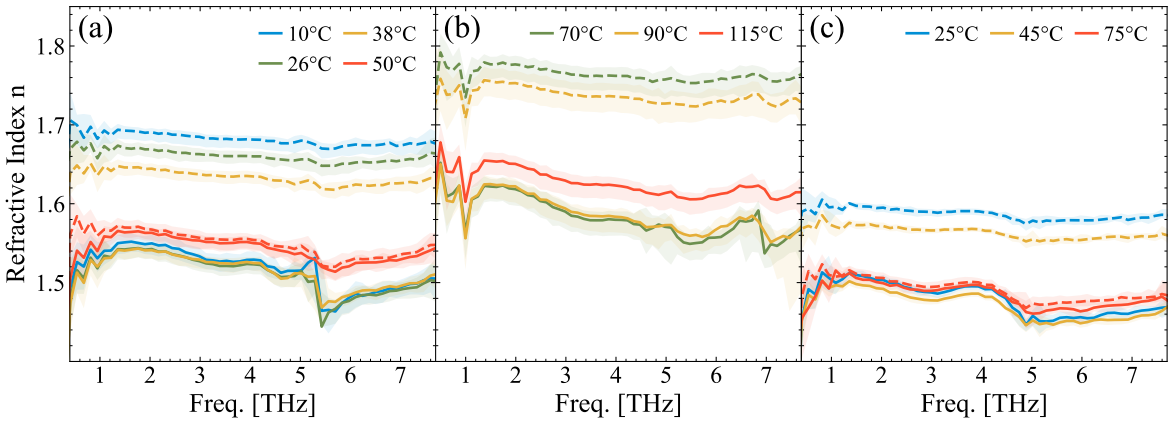

Figure 5.1.: Refractive indices of (a) 8CB, (b) 8OCB, and (c) PCH5 as a function of THz frequency and temperature covering all phases each molecular species shows. The bold line is the ordinary response, while the dashed line the extraordinary.

which is comparable to the values found in the visible regime. As expected from the well known visible behavior, the birefingence grows with sinking temperature, reflecting the change in density and order parameter S induced by thermal disorder.

5.1.2. THz absorption

This section will discuss the absorption spectra for all three molecular species in detail, as they are the main point of interest here. Particular focus is put on 8CB (and 5CB) as they represent benchmark system both experimentally and computationally. 8OCB and PCH5 receive a shorter discussion on the basis of the analysis performed on the nCBs. The end of this section will provide a global picture concerning the molecular structure and its impact on the absorption spectra [93, 111].

5.1.2.1. Molecular species

In Figure 5.2a, the isotropic phase of the nCB series is under consideration, where the system is in a disordered state and behaves liquid-like for the nCB family. Given the different phase behavior among the nCBs, the isotropic phase is the state all have in common (see section 2.6), allowing for comparison across the widest range in chain length. The first thing to notice is that by increasing the chain length, a steady decrease in absorbance for the whole 1 THz to 7.5 THz region is seen. This is not surprising, considering that the intensity is measured per unit volume, and a decrease in the number of molecules per unit volume is expected with increasing chain length due to the pure steric effect [133, 134]. However, the trend is not equal for all the spectral features. To explain this, the first factor one should consider is that the modes have different origins, as will be discussed in detail for the computed spectra.

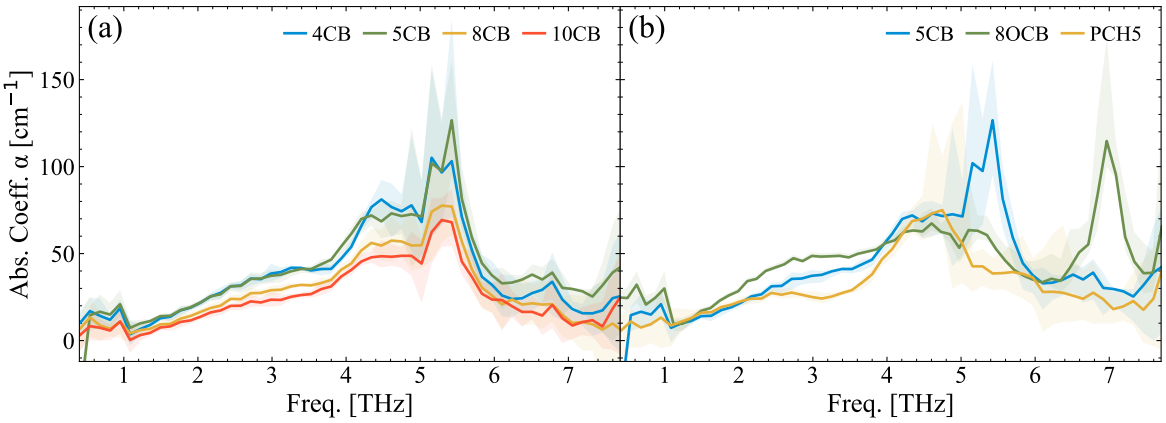

Figure 5.2.: (a) Absorption spectra of selected members of the nCB series in isotropic phase measured by TDS. Since the chosen molecules show different phase behavior, the isotropic phase is the only one they have in common. The temperatures are set to 10° C – 20° C above the phase transition. The comparison allows for investigation of the effect of the alkyl chain length. (b) Absorption spectra of 5CB and PCH5 in the isotropic phase. The comparison allows to identify the contribution of the core towards the molecules THz activity while the alkyl chain length is held constant.

Increasing the chain length, the number of CN per unit volume decreases, bringing a decrease in intensity for those spectral features dominated by the cyano group, thus between 4 THz to 6 THz. At the same time, the number of CH_2 groups per unit volume increases with the chain length, partially counteracting the decreased density, especially below 3.5 THz, where skeleton modes of the alkyl chains are massively involved. Therefore, modification of the chain length mainly serves as a tunable parameter affecting the overall amplitude of the response in the region under investigation. The density of the material and the number of CH_2 compete to determine the final integrated intensity.

In the next step, 8OCB and PCH5 are compared to the nCBs, yielding information on the effect on the absorbance when the molecular core structure is modified. For 8OCB one oxygen atom is inserted between the bi-phenyl core and the alkyl chain, while for PCH5 one phenyl ring is exchanged with a cyclohexane group. A direct comparison of all three species is shown in Figure 5.2b in the isotropic phase, where strong changes in the spectroscopic character are evident. In general terms, the results of all molecules point to a behavior in which a smooth monotonic increase in the absoption strength is a universal feature in the low frequency wing of the available THz spectrum, that then, above roughly 3 THz, reveals distinct features. Each molecules absorptive behavior with reference to the benchmark nCB series receives a detailed discussion in the following sections.

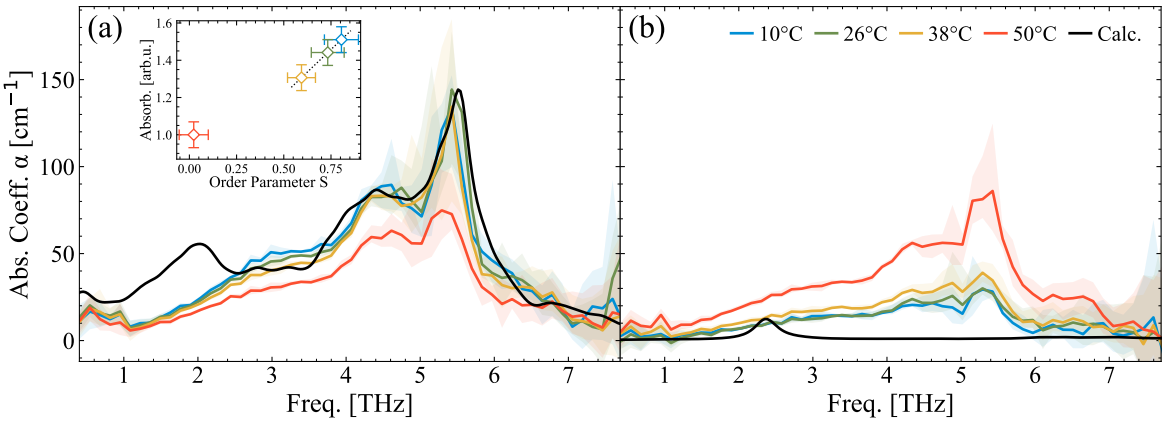

Figure 5.3.: Absorption spectra of 8CB obtained by TDS along (a) the ordinary and (b) the extraordinary axis. The spectra (colored traces) have been measured for sample temperatures of 10 °C, 26 °C, 38 °C, and 50 °C, corresponding to crystalline, smectic A, nematic, and isotropic phases. Inset in (a): Estimation of the degree of order S compared to the intensity of the lowest absorption band. Black line: Harmonic gas-phase computed spectra. To help the comparison with the experimental data, the computed frequencies have been scaled by a factor of 1.075 and the intensities normalized on the 5.5 THz *peak.*

5.1.2.2. 8CB

Figure 5.3 shows the absorption spectra measured in the TDS setup (section 3.3) for 8CB with the THz polarization oriented along the ordinary (a) and extraordinary (b) LC axis. The traces are measured for different temperatures (colored lines) spanning all condensed phases presented by the compound. 8CB is of particular interest since it is the shortest nCB showing both smectic A (21.5 °C - 33 °C, green solid line) and nematic (33 °C - 40.5 °C, orange solid line) phases. Hence, it allows to measure any possible impact of the molecular ordering on the spectral absorbance. When looking at the spectra as a function of temperature one can see that the TDS spectra are nearly identical for the smectic and nematic phases, i.e., where the molecules are in the aligned LC mesophases. A more substantial difference can be spotted in the isotropic phase (red solid line), i.e., when the molecules are not aligned.

Looking now at the 8CB extraordinary spectra, one can first observe how it decreases with sinking temperature, whereas the total intensity between 2 THz to 8 THz increases in the ordinary absorbance. Given the typical order parameter S of LC below one (for nematic and smectic phases S 0.3 - 0.8), as previously introduced [135], the THz pulses are most likely probing projections of the ordinary axis of molecules slightly misaligned with the director, giving contributions to the extraordinary absorbance. Compatible with this, little difference is seen in the lowest temperature extraordinary traces, associated with the highest order phases (blue and green solid line in Figure 5.3b), and then an increase for the nematic case (orange solid line). It has been shown extensively that the smectic phase forms ordered bilayer structures [58], which could possibly contribute

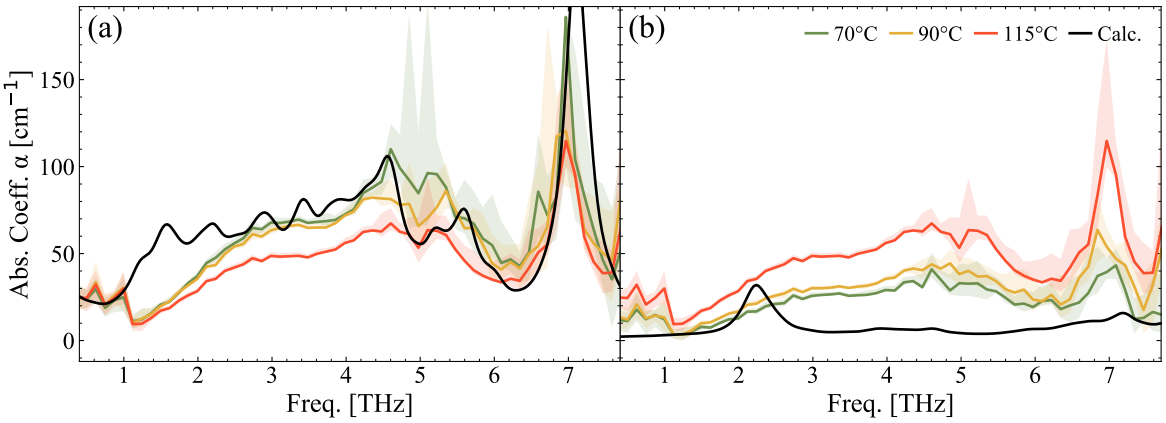

Figure 5.4.: Absorption spectra of 8OCB obtained by TDS along (a) the ordinary and (b) the extraordinary axis.

to damping the rotational degrees of freedom. Inside the smectic A phase ordered arrangement, where the biphenyl structures are stacked next to each other, the rotational modes are more hindered compared to the nematic phase, where there is also the freedom for the molecules to be randomly translated with respect to each other along their long axis.

5.1.2.3. 8OCB

The measured TDS absorption spectra are presented in Figure 5.4, with panel (a) presenting the ordinary results as function of temperature, and panel (b) the extraordinary results. Since the LC phases are relatively high above ambient temperature, it is easy to get this compound to crystallize. Unfortunately, it was not possible to get it to form a uniform mono-crystal. In fact, any result was highly amorphous, as evidenced by it's opaque nature when inspected visually. Therefore, only the smectic A (green), nematic (yellow), and isotropic phases are reported (red, this phase has been measured only once, and included in both plots).

The spectral behavior is significantly modified compared to the nCB benchmark systems. In the ordinary case the low frequency band is stronger, the distinct absorption bands at 4.5 and 5.5 THz are affected, and a sharp peak at 7 THz appears. It has to be noted that relative comparison of the amplitude of this strong 7 THz mode to the rest of the spectral response in the experimental traces should be done with caution, since it already exceeds the dynamic range of the TDS setup.

5.1.2.4. PCH5

Figure 5.5 shows the full spectroscopic data set for the PCH5 sample, where it is split into the ordinary traces in panel (a) and the extraordinary traces in panel (b). Each panel contains TDS spectra for different temperatures. The isotropic phases at 75 °C

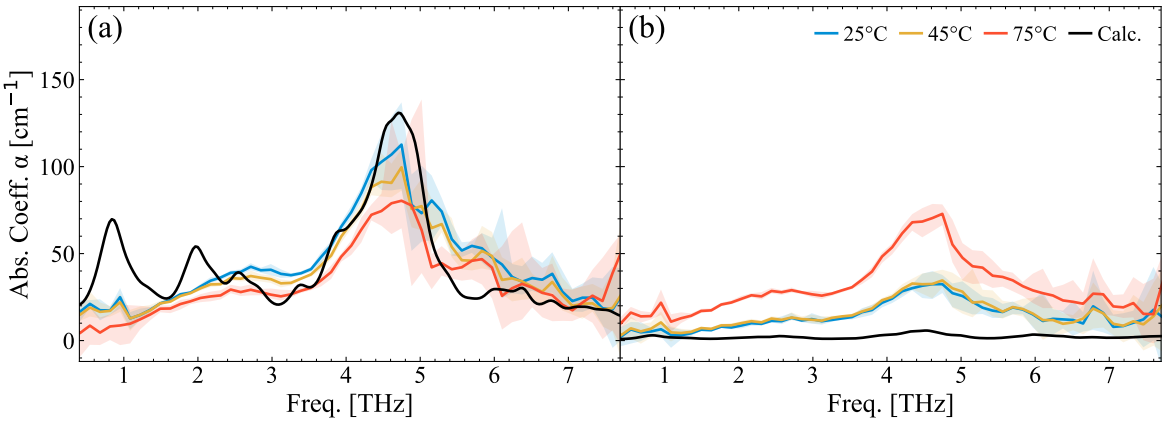

Figure 5.5.: Absorption spectra of PCH5 obtained by TDS along (a) the ordinary and (b) the extraordinary axis.

(red bold lines) match within the uncertainty as expected for this uniaxial state, and the absorption grows with the ordered nematic phase measurements at 45 and 25 °C in the ordinary condition, and shrinks in the extraordinary condition accordingly.

5.1.3. Molecular DFT interpretation

Based on single molecule gas phase DFT calculations, a first interpretation of the measured spectra is possible. The DFT results, as outlined in Section 3.4.2, are laid over the experimental results in bold black lines for 8CB, 8OCB, and PCH5 in the respective Figures 5.3, 5.4, and 5.5. In the following, each case will be discussed in detail separately.

5.1.3.1. 8CB

The computed frequencies have been scaled by a factor 1.075, and the intensities normalized on the strongest mode (5.5 THz of 8CB) to help the comparison with the experiment. Looking at the experimental spectra obtained in 8CB with THz polarization along the ordinary axis shown in Figure 5.3a, one can recognize four regions that have been assigned to specific modes thanks to the computational support.

Below 3.5 THz the 8CB molecules show mainly (NCPhe)-Phe-alkyl skeleton modes, i.e., the CN group is not vibrating. To support this statement, the atom mass of selected groups of the 8CB molecule is computationally increased to 100 amu (atomic mass units) and the impact on the absorption spectrum is depicted in Figure 5.6a. When the atoms with increased mass are contained to the CN group, the corresponding absorption spectrum below 3.5 THz is almost identical to the unmodified 8CB response (see solid orange line compared to black). The small shift and change of intensities are due to the small variation of the modes reduced mass. On the other hand, the spectrum completely lacks all modes above 3.5 THz, where the CN group plays a dominant role. Further increasing the number of atoms with heavier mass, like in the cases of CCN (light purple

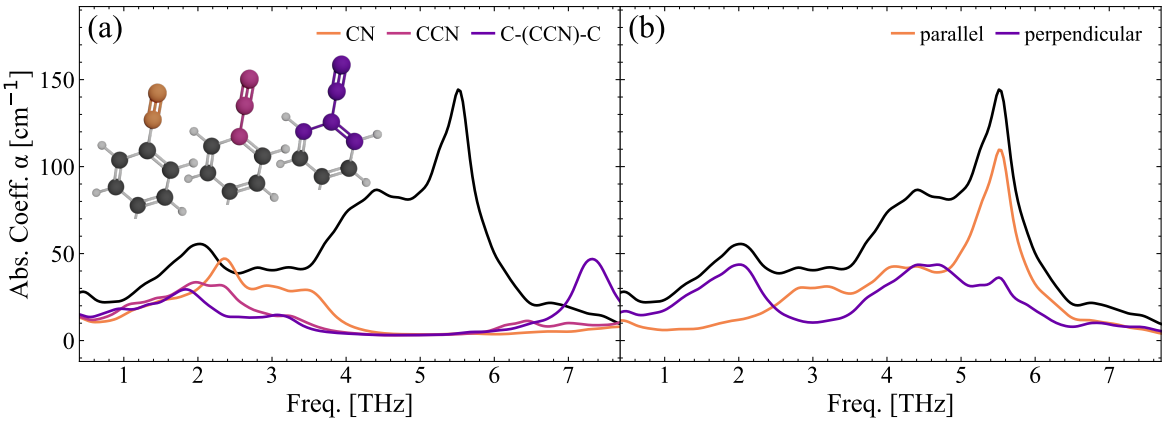

Figure 5.6.: (a) Computational deuteration of isolated components of the molecule and the resulting response when increasing the atomic mass (100 amu), effectively killing their contributions. When the heavy atoms are contained to the CN group (orange) the remaining response resembles the low frequency modes. Further increasing the heavy region to CCN (light purple) and C-(CCN)-C (dark purple) starts to modify also those modes. (b) Calculated ordinary response (black) and its contributions when polarized parallel (orange) and perpendicular (purple) to the phenyl rings.

line) and C-(CCN)-C (dark purple line), affects the entire spectrum, including below 3.5 THz, showing the delocalized and collective nature of this mode.

Between 4 THz to 6 THz, the CN group takes part in the vibration. The alkyl chain skeleton modes are now coupled with the CCN bending and the biphenyl (Phe-Phe) bending modes. The out-of-plane bending modes tendentially are located at lower frequencies (4 THz to 5 THz) compared to the in-plane bending modes (5 THz to 6 THz) as indicated by the computed polarized spectra in Figure 5.6b on the direction parallel (orange curve) and perpendicular (purple curve) to the phenyl rings. Finally, between 6 THz to 8 THz mainly (NCPhe)-Phe-alkyl skeleton modes (no vibrations of the CN group) can be found.

The comparison between the experimental and the calculated single molecule spectra shows very good agreement above 3.5 THz. At the same time, the ordered phase experimental spectra above 3.5 THz show only negligible differences (within the experimental uncertainty), and the differences with the isotropic phase originate from the substantially different alignment, in which all molecules (now pointing in random directions) contribute according to the projection of their short axis onto the polarization direction of the THz pulses. Therefore the absorption can be attributed to the ensemble of individual vibrating molecules, in other words, mainly an intramolecular response.

The situation changes at and below 3.5 THz. One observes a clear reduction in total intensity with increasing temperature. As presented in section 2.2, the commonly used orientational order parameter [135] quantifying the degree of alignment is decreasing with rising thermal energy in the LC systems. Here, a linear trend (excluding the isotropic phase) is found on the integrated intensity of the lowest ordinary mode with

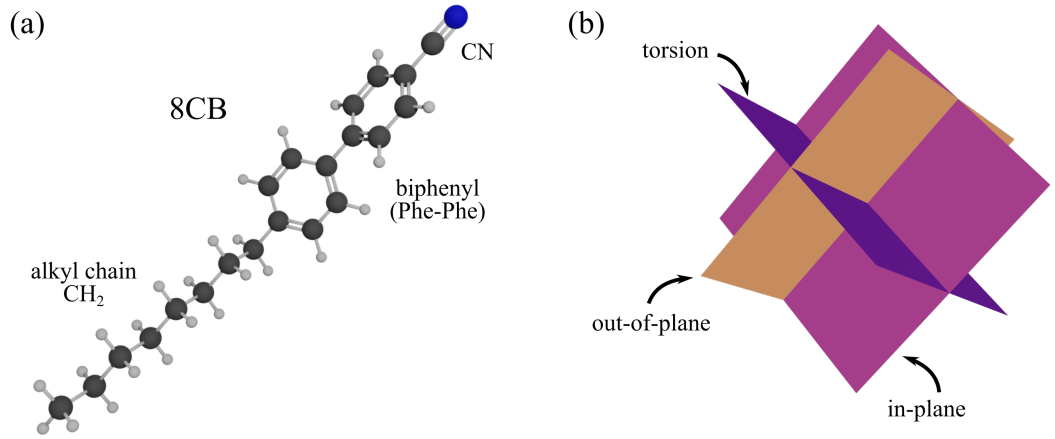

Figure 5.7.: Terminology used in the discussion. (a) Functional groups of 8CB, and (b) the planes defined by the biphenyl backbone.

the experimentally-derived order parameter S (see inset in Figure 5.3a). For the experimental extraction of S, we follow the procedure outlined by Vieweg *et al.* [136], with further reference to [137, 138]: The order parameter S can be expressed as

$$S = \frac{n_\mathrm{e}^2 - n_\mathrm{o}^2}{\bar{n}^2 - 1} \frac{\bar{\alpha}}{\Delta\gamma} \tag{5.1}$$

where $n_{\mathrm{o/e}}$ are the ordinary and extraordinary refractive indices, $\bar{n}^2 = \frac{1}{3}n_\mathrm{e}^2 + \frac{2}{3}n_\mathrm{o}^2$, $\bar{\alpha}$ is the mean polarizability, and $\Delta\gamma$ is the difference between longitudinal and transverse polarizability components of perfectly ordered molecules. The refractive indices are a natural result of the TDS measurements presented in section 5.1.1 and are averaged over the region form 2.8 - 3.5 THz, which is the region of interest for this comparison. The ratio $\frac{\Delta\gamma}{\bar{\alpha}}$ can be extracted by extrapolation in temperature to 0 K of a finely sampled data set. Here, the data does not allow for this approach. Therefore, values reported by Vieweg *et al.* [136] for 5CB, 6CB, and 7CB are extrapolated to 8CB. This approach is inherently limited in precision, but sufficient for the purpose of establishing a general trend in S. For 8CB, $\frac{\Delta\gamma}{\bar{\alpha}} = 0.4 \pm 0.025$ is chosen, with the error accounting for the uncertainty in the extrapolation. The error of S has been computed by standard error propagation. Furthermore, it must be stated that this approach has been developed for the nematic liquid crystals phase, while here it is applied across all mesophases.

This linear trend established in collective order in the lowest frequency mode is accompanied by general discrepancies between measurement and gas phase calculation, as evidenced by the experimental and theoretical traces in Figure 5.3. This points towards an effect of the intermolecular interactions. Interestingly, the peak found at 2 THz in the computed spectra is almost completely explained by modes pointing out of the plane of the ring (purple curve in Figure 5.6d). Given the preferential co-facial arrangement of neighboring molecules, in which the biphenyl structures face each other in an anti-parallel manner [58] to maximize both the dipole-dipole interactions and the π-π

stacking, it is reasonable that these modes are most sensitive to intermolecular interactions and that they are modulated by this kind of packing in a condensed phase. This assumption is qualitatively tested using dimer and trimer calculations at the end of this section.

Interestingly, for the extraordinary axis the calculations barely predict any absorption, while the measurements show a clear response. In particular, below 3.5 THz the calculations predict only one vibrational mode generating dipole fluctuations parallel to the molecular axis, i.e., active along the extraordinary axis. This mismatch between experiments and calculations is explained by considering the molecules non-perfect alignment in the LC cell ($S \neq 0$), even in the presence of an aligning AC field.

5.1.3.2. 8OCB

Analogously to the discussion for 8CB, in the extraordinary axis the calculations predict negligible activity. All behavior can be attributed to molecules misaligned with the average director due to thermal noise. Hence, all molecular dynamics will be discussed in terms of the ordinary axis.

In the case of the 8CB, the cyano group was not taking part in the vibration in the region between 6 THz to 8 THz. On the other hand, in the case of 8OCB the cyano group is heavily involved. The strong peak around 7 THz is in fact a CCN bending coupled with torsions around the oxygen and the biphenyl bending mode. These modes are mainly polarized perpendicularly to the phenyl rings. The region between 4 THz to 5.5 THz presents still CCN bending coupled with torsions around the oxygen and the Phe-Phe bending modes. However they are mostly polarized parallel to the rings. The region below 3.5 THz is dominated by (NCPhe)-Phe-Alkyl skeleton modes as in 8CB, from a gas phase DFT perspective.

5.1.3.3. PCH5

Just as in the cases above, the DFT calculation predicts hardly any absorption along the extraordinary axis, and all measured intensity is attributed to projections of the ordinary axis, due to the order parameter. The ordinary axis contains the direct spectroscopic information and can be assigned to the molecular dynamics with the computational input.

While in the case of the nCB series, the two phenyl rings almost lie in the same plane, in the case of PCH5 they lie at 90 ° with respect to each other. One observes clear modification of the absorption behavior in this region. The cyclohexane ring is much less structurally rigid compared to a phenyl ring, leading to more degrees of freedom for the molecular skeleton to move. As a consequence, a strong modification of the 5.5 THz mode and the creation of a valley at 3.2 THz within the broad low-frequency band are seen. Both of the effects are already well modeled by the isolated molecule calculations, pointing to the dominant role of the intramolecular interactions. However, especially in the case of the 3.2 THz band, it is not excluded that also intermolecular effects can play a role in determining the exact band shape. The mode at 4.5 THz is instead largely

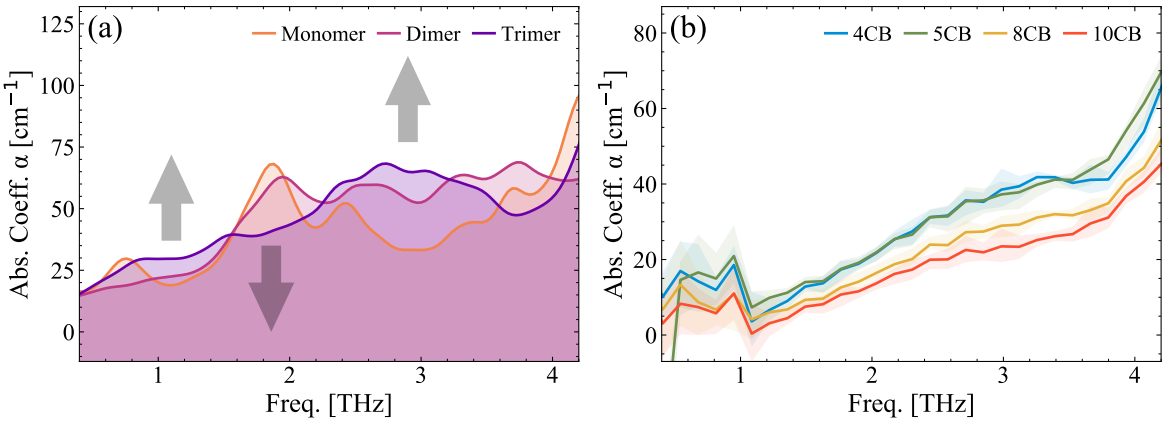

Figure 5.8.: (a) Calculated spectra for monomer (orange), dimer (light purple), and trimer (dark purple) of 5CB at BLYP level. A clear shift of the pronounced low frequency peak towards higher frequency and broader width with increasing molecule number is visible, indicating an intermolecular response. (b) The low frequency response of selected members of the nCB series at isotropic phase for comparison with (a)

unaffected within the measurement uncertainty, with a small narrowing as the only noticeable change. The calculations show that this is due to the balance between two opposite effects: (i) The missing coupling between the two rings bending modes red shift the in-plane bending to 4 THz to 5 THz, i.e., the in-plane and out-of-plane modes are almost degenerate. (ii) The absolute intensity of each mode on average decreases, possibly, because the missing coupling between the two rings reduces the charge fluxes responsible for the IR intensity.

5.1.4. Cluster DFT calculations

Lastly, the discrepancy between measurement and calculation below 3.5 THz is under discussion by comparing calculations with an increasing number of molecules. Past work attributed the low THz mode to Poley absorption, [28–30] and later to the Ioffe-Regel crossover [41] in relation to disordered systems. Here, a much simpler explanation, based on conventional intermolecular interactions, is presented. 5CB is used as a test molecule, because it comes with reduced computational cost compared to 8CB, meaning only 27 possible single conformations in 5CB compared to 264 in 3.5 kcal/mol for 8CB.

The computed data show that the intermolecular interactions are responsible for the blue-shift of the 2 THz modes in the clusters (dimers and trimers) with respect to the gas phase. These blue shifted modes compare favorably on qualitative terms with the measured responses shown in Figure 5.8b. While this model is a simplification of the molecular packing in the condensed mesophases and does not allow quantification of the extent of the delocalization of the mode and the impact of long-range interactions, it gives clear indications of the intermolecular character of the mode on display.

5.1.5. Summary

The THz spectra for all three molecular species investigated are characterized by two aspects. Firstly, at higher frequencies the spectra are well described by gas phase DFT calculations and their vibrational modes can be assigned. Therefore, these modes are interpreted as intramolecular modes. Secondly, the low-frequency mode is deviating from the calculations for every sample, hinting at its intermolecular nature, which is supported by the cluster calculations.

Within the context of the research question, the changes in molecular arrangement have little influence on the overall shape of the observed spectra. At higher frequencies the modes remain a response of individual molecules, and at lower frequencies the broad intermolecular peak shows weak modification in amplitude only, most likely related to changes in density. Overall the samples behave like disordered molecular fluids, with a broad intermolecular band and intramolecular modes present simultaneously in the available bandwidth.

5.2. Transient birefringence

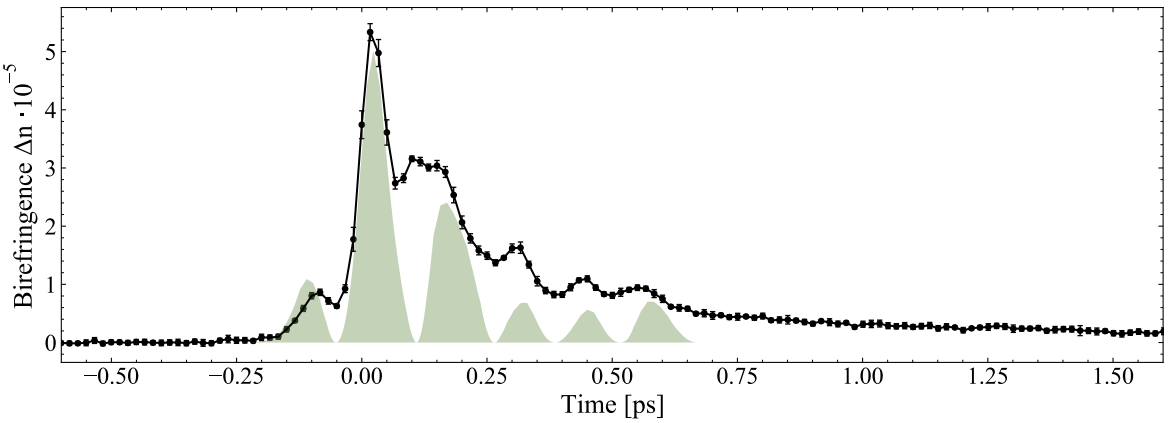

*Figure 5.9.: Representative trace as measured in the transient Kerr experiments. The x-axis represents the time delay between the THz pulse and the ultrashort probe pulse. The y-axis stands for the ellipticity acquired by the probe, which encodes the transiently induced birefringence of the sample. The resulting sub-*ps *transients show oscillatory behavior, followed by a long range relaxation (note that the response has not yet reached base line by the end of the plot). For reference, the square of the THz electric field, as measured in the interaction region, is plotted as a shaded area.*

The transient birefringence experiments yield traces that qualitatively appear as the trace shown in Figure 5.9. They are uni-polar sub-picosecond transients with a well-resolved oscillation and a long range relaxation tail. The maxima of the oscillation coincide with the points of maximum intensity of the driving THz pulse. In other words, the maxima found in the transiently induced birefringence are generated by the square of the THz electric field, as indicated by the green shaded area in Figure 5.9, and expected from typical THz Kerr experiments [21]. Upon closer inspection, the acquired traces show a further oscillation superimposed and out of phase with the expected beat nodes right after the global peak, which will be subject to further discussion in the concluding parts of this chapter. To complete this qualitative description, the clearly visible exponential relaxation tail on picosecond time scale following the presence of the driving field is accompanied by another fast relaxation that is responsible for smearing out the response between consecutive THz beat nodes. This behavior is qualitatively true for measurements performed under varying conditions, and in the following, a detailed discussion of all contributing terms will be presented, and the influence of any scanning parameters discussed.

5.2.1. Scaling properties

It is instructive to look at the scaling properties of these traces with different tuning parameters. An overview over the scaling behavior can often lead to intuition about

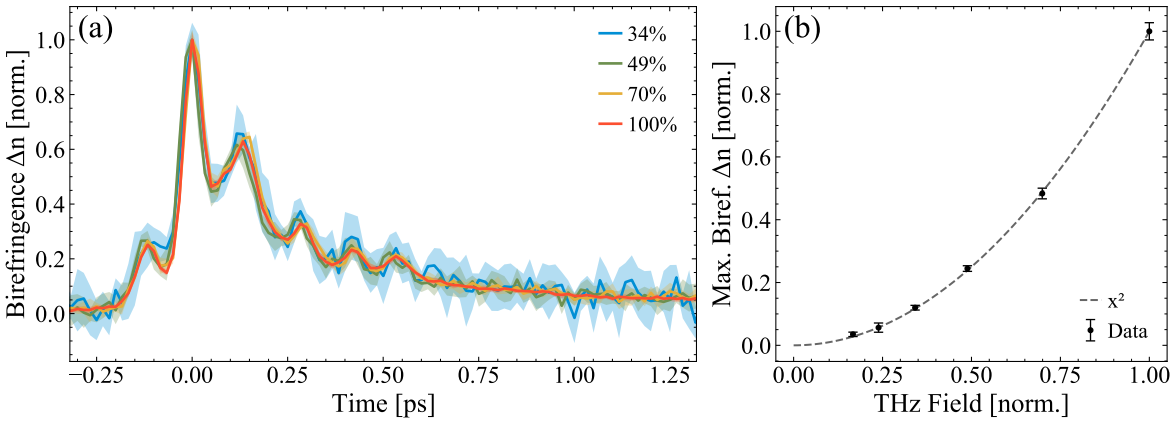

Figure 5.10.: Transient THz Kerr response as a function of the driving field strength. The field strength is controlled incrementally by insertion of Si wafers acting as broadband transmission filters. (a) Normalized traces of the full time resolved response for the first four transmission settings, showing the uniform amplitude scaling. (b) Peak value of the THz Kerr response as function of the peak THz field strength. Both axes are normalized, and an ideal parabola is drawn in dashed lines as guide to the eye.

the underlying physics from a purely experimental perspective. This is the goal of the following subsections. The dynamics will be evaluated from three angles. Once, how does it behave with a change in the driving THz field. Here the natural choice is to look at scaling with the electric field strength of the pulses inducing the dynamics. Then, from a macroscopic properties perspective, the unique arrangement of the LC samples are the ideal platform for material tunability, with the mesophase representing a change in collective molecular order. And lastly, to gain insight into the microscopic aspects, changing the molecular species will help elucidate the impact of the molecular composition and properties on the THz induced dynamics.

5.2.1.1. Scaling with THz field strength

Here, the focus lies on the impact of the driving field on the dynamics. Using Si wafers as broadband intensity filters (see section 3.1.4), the driving field strength can be attenuated incrementally by 70% (in $\mathrm{V\,m^{-1}}$, or 50% in intensity) per inserted wafer.

The results presented in Figure 5.10 are measured in the isotropic phase of 8CB, but the conclusions are representative for all samples and their phases. Figure 5.10a shows the full traces in time for the four highest electric field settings in a normalized fashion. (Lower field traces have been omitted in order to maintain readability, since the relative uncertainty becomes graphically dominating. The conclusions hold, regardless.) The purpose of Figure 5.10a is to show the uniform amplitude scaling at all times during the evolution. Within the experimental uncertainty, all curves match.

Figure 5.10b completes the picture by presenting the peak of each measured trace (normalized to the peak of the strongest driven trace) against the normalized THz field

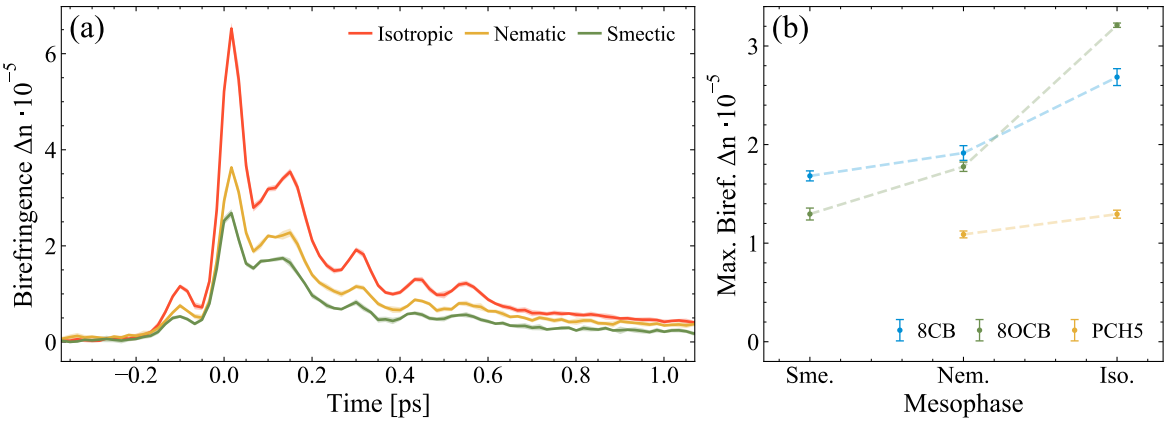

Figure 5.11.: (a) THz Kerr traces for the three mesophases of 8OCB, and (b) the peak of the response plotted against mesophase for each molecule for a fixed THz field strength. The dashed line is a guide to the eye.

strength achieved by the Si attenuators (field transmission of the stack of Si wafers). As a guide to the eye, an ideal square response is added to the plot. Within the error bars, the measured values match the quadratic behavior, proving the χ^3 nature that would be expected from a Kerr excitation. (In the follwing discussions, the 100% electric field setting for 8CB are missing for the nematic and smectic mesophases. At 2 MV cm^{-1}, the sample showed accumulation effects in terms of full reorientation. All other settings were not affected.)

5.2.1.2. Scaling with LC phase

As discussed throughout this work, the tuning of the collective order is a key feature of the LCs under investigation. In an LC medium, this collective order can be tuned via phase transitions, here as function of temperature.

In Figure 5.11a the responses for the same THz electric field setting are given for all mesophases of the 8OCB sample under investigation. In general terms, the amplitude of the response decreases with the more ordered phases and the decrease from isotropic to nematic is larger than the decrease from nematic to smectic. This holds for all samples under investigation, as can be seen from Figure 5.11b, where the peak of the response for a fixed field strength is plotted against the mesophase for each sample.

5.2.1.3. Scaling with molecular structure

Lastly, the molecular composition is also expected to impact the macroscopic Kerr response. The three samples introduced in Chapter 2.2 were chosen for their similarity, making it easier to identify how each structural component impacts on the dynamics under THz radiation.

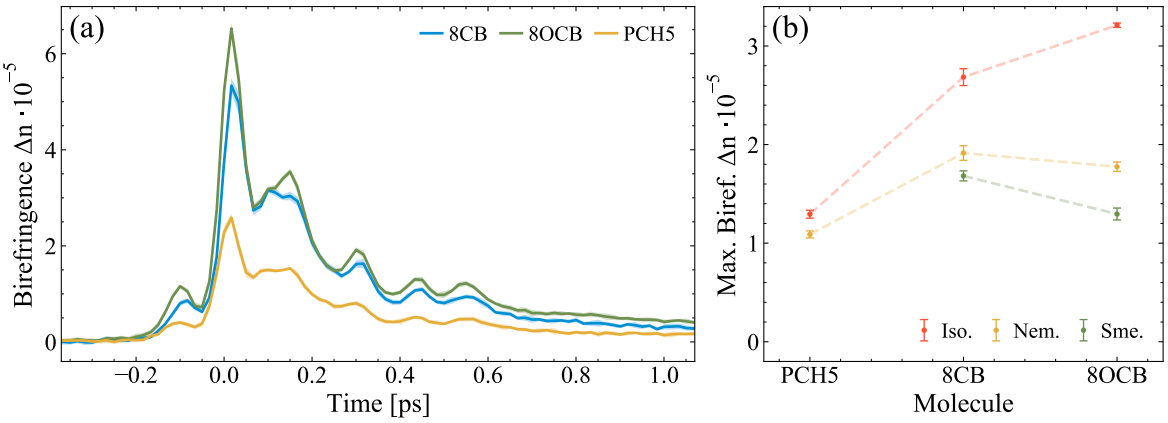

Figure 5.12.: (a) THz Kerr traces for all three molecular species under investigation for a given THz peak field strength in isotropic phase, and (b) the peak of the response for each phase against the molecule under investigation. Panel b contains the same information as Figure 5.11b plotted differently. The dashed line is a guide to the eye.

Figure 5.12a shows the isotropic response plotted in absolute units of induced birefringence Δn. It is noteworthy, that the dynamics are affected predominantly in the amplitude scaling and show similar amplitude for 8CB and 8OCB, while PCH5 is driven with half the ampitude. Therefore, it is reasonable to pinpoint the phenyl group as a major contributor to the amplitude, either in electronic terms (delocalized π electrons versus localized) or in nuclear terms (rigid versus flexible ring). Panel b of Figure 5.12 summarizes this behavior for all phases, by plotting the peak of the response.

5.2.2. Rotational diffusion model

The measured THz Kerr traces are understood within the model of rotational diffusion, as introduced in section 3.5.1. Figure 5.13 shows a qualitative example, with all three contributions to the total expression highlighted individually to show their impact on the dynamics. While the electronic and short lived nuclear processes define the behavior of the oscillatory response during the presence of the THz electric field, the long lived response on picosecond scales mainly defines the exponential tail to the dynamics. To test it's validity for LC systems, the model in the form of equation 3.32 is fitted against the experimental data. The $E^2_{\mathrm{THz}}(t)$ trace is measured prior to the Kerr experiment and used as input, together with the EOS detection efficiency correction, as described in section 3.1.2. The traces are scaled in time axis by a factor 0.965[1], the necessity of which can be seen by the mismatch in overlap of the oscillation peaks in the Kerr data

[1] Adjusted manually. The exact value would require a more refined correction of the THz traces. Furthermore, it only accounts for propagation effects in Gap, and not the LC sample. The phase matching in the LC sample is significantly better compared to GaP, justifying its omission. Leaving the scaling as a free parameter in the fits leads to optimizations into local minima, that don't describe the data properly.

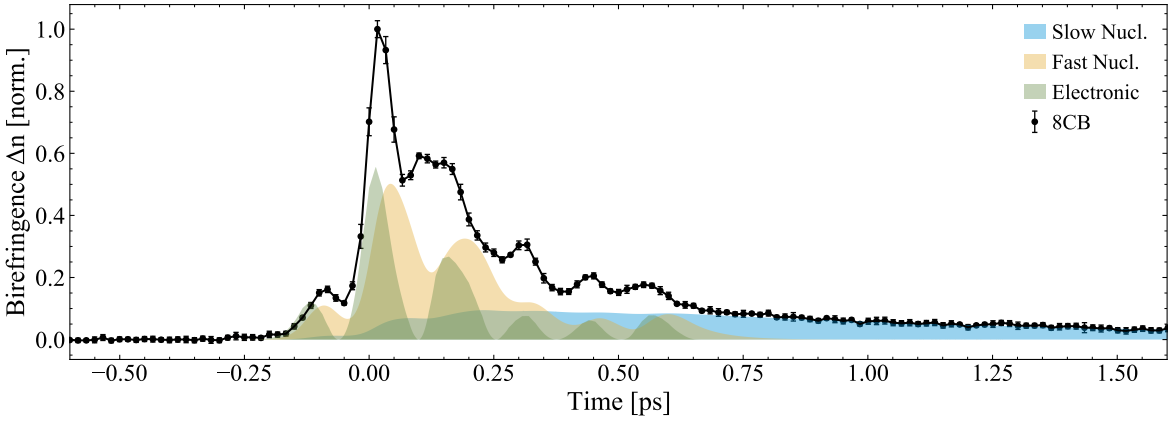

Figure 5.13.: qualitative response of the THz Kerr model, including the individual terms of electronic and nuclear responses.

and the unscaled $E^2_{\mathrm{THz}}(t)$ trace in Figure 5.9. Furthermore, the data in Figure 5.9 has been plotted with both traces set to time zero in their maximum. For the fits, the THz trace is shifted by 0.015 ps forward.[2]

The final fits of the model consist of five free parameters: three amplitudes, describing the strength of the electronic and the two nuclear terms in Δn, and two relaxation time constants, associated with the nuclear (molecular) response. The full fitting function reads as equation 5.2. Unfortunately, the parameters are not fully independent, and exhibit some covariance between the parameters, making the fits dependent on the initial conditions.

$$\Delta n(t) = A_{\mathrm{el.}} E^2_{\mathrm{THz}}(t) + A^{(1)}_{\mathrm{nucl.}} \int_{-\infty}^{\tau} E^2_{\mathrm{THz}}(t) e^{-(\tau - t)/\tau_1} d\tau' + A^{(2)}_{\mathrm{nucl.}} \int_{-\infty}^{\tau} E^2_{\mathrm{THz}}(t) e^{-(\tau - t)/\tau_2} d\tau' \tag{5.2}$$

The additional peak identified as out of phase with the expected $E^2_{\mathrm{THz}}(t)$ generated peaks is not accounted for by the model. Therefore, fitting the entire curve would lead to unreliable results. In order to address this problem, this part of the trace has been excluded from the optimization. The missing data points are identifiable in the plots by the lack of plotted error bars. For the same fitting procedure with all points taken into account, the reader is referred to Appendix A. The final fits are accompanied by he residuals and reduced $\chi^2_{\mathrm{red.}}$ values. The extracted parameters are reported in table form. For each molecular species, all LC mesophases are fitted independently for the highest THz field strength and compared against each other. The fitted data is normalized to one for each case, so that the amplitudes in the fit represent the relative strength of each term in the model contributing to the overall response.

The results for 8CB are plotted in Figure 5.14 and summarized in Table 5.1, for 8OCB in Figure 5.15 and Table 5.2, and for PCH5 in Figure 5.16 and Table 5.3. In quantitative

[2] Adjusted manually. Leaving the shift as free parameter has led to unstable results.

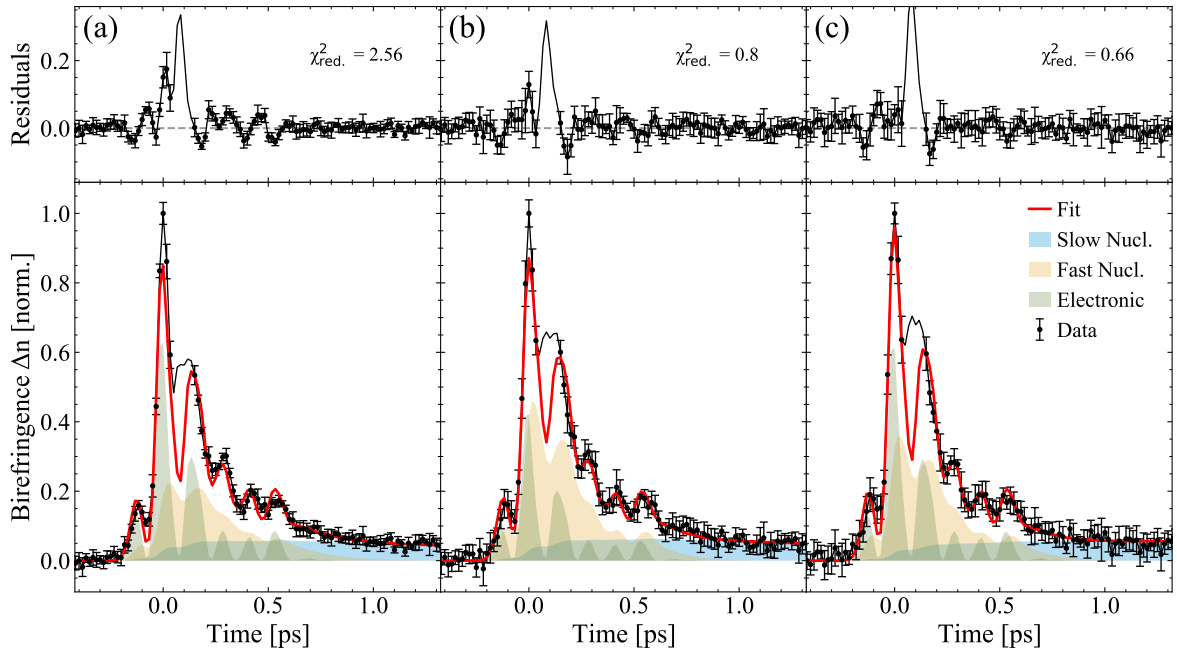

Figure 5.14.: Rotational diffusion fits to the 8CB THz Kerr data, for (a) isotropic, (b) nematic, and (c) smectic mesophases. The top panel reports the residuals and the reduced $\chi^2_{red.}$. The bottom panel contains the experimental data (black) and the full fit (red). Additionally, the three individual terms of the model are plotted as shaded areas. Here, the identified peak out of phase with the THz peaks are excluded from the fits, and marked by missing error bars.

Table 5.1.: Fit parameters extracted for 8CB for each mesophase.

Mesophase	τ_1 [ps]	τ_2 [ps]	$A_{el.}$	$A^{(1)}_{nucl.}$	$A^{(2)}_{nucl.}$
Isotropic	0.157±0.041	2.3 ± 3.0	0.653±0.036	0.223±0.023	0.058±0.020
Nematic	0.092±0.011	3.0 ± 2.3	0.440±0.050	0.461±0.041	0.063±0.008
Smectic	0.106±0.010	2×10^6	0.639±0.041	0.361±0.037	0.056±0.003

terms, the model describes the experimental traces quite well, disregarding the excluded range. The residuals show some remaining systemic deviations of the model within the fitted range, which is reflected in the $\chi^2_{red.}$ values. It can be partly explained by the way the underlying THz data is corrected for the GaP detection efficiency. Furthermore, it is likely that the excluded out-of-phase response extends further in time than reflected by the data selection, skewing the fit results. Furthermore, some fitted values (especially τ_2) are either meaninglessly large or have large error values.

The slow relaxation term, which gives the least reliable results in the model fit, can be quantified independently. Since the THz driving field is only present for a limited amount of time, the decay afterwards takes place completely field-free. Therefore, the time

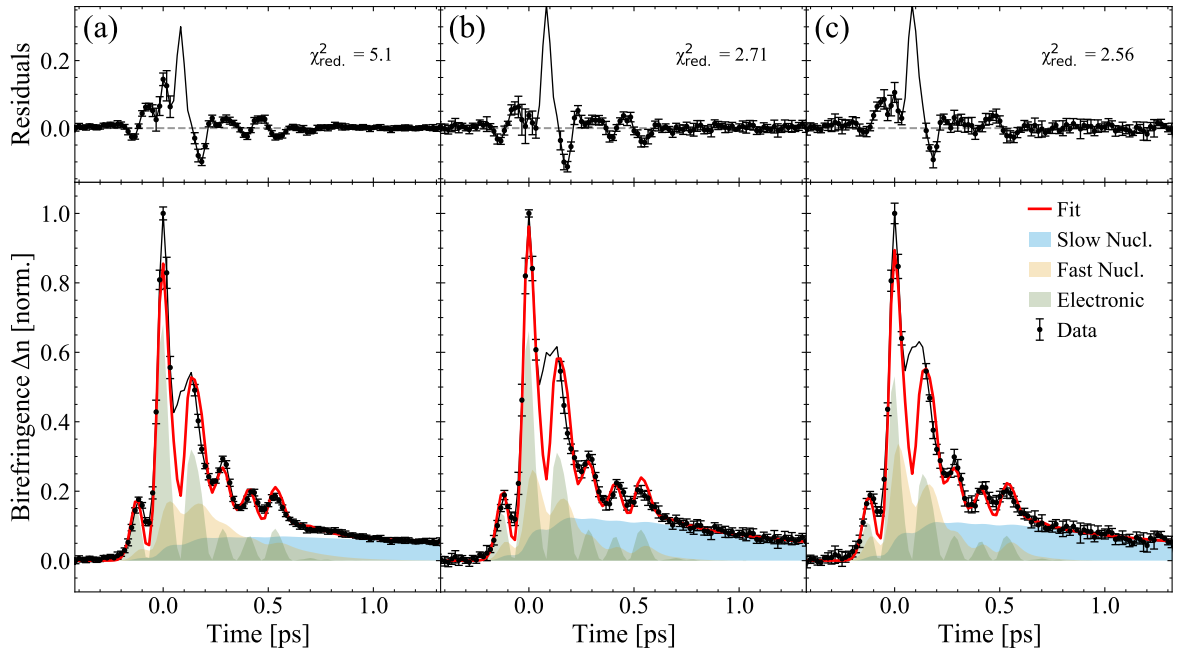

Figure 5.15.: Rotational diffusion fits to the 8OCB THz Kerr data, for (a) isotropic, (b) nematic, and (c) smectic mesophases. The top panel reports the residuals and the reduced $\chi^2_{red.}$. The bottom panel contains the experimental data (black) and the full fit (red). Additionally, the three individual terms of the model are plotted as shaded areas. Here, the identified peak out of phase with the THz peaks are excluded from the fits, and marked by missing error bars.

Table 5.2.: Fit parameters extracted for 8OCB for each mesophase.

Mesophase	τ_1 [ps]	τ_2 [ps]	$A_{el.}$	$A^{(1)}_{nucl.}$	$A^{(2)}_{nucl.}$
Isotropic	0.162±0.043	2.4 ± 2.0	0.704±0.036	0.171±0.020	0.070±0.015
Nematic	0.071±0.017	1.02 ± 0.19	0.684±0.053	0.262±0.046	0.123±0.015
Smectic	0.064±0.011	1.16 ± 0.23	0.549±0.055	0.337±0.045	0.111±0.012

constant τ_2 is extracted by a fit of the purely exponential function $f(t) = A\exp(-t/\tau_2)$. The results are summarized in Table 5.4 and plotted in Figure 5.17. Here, the results are consistent with a 1 ps decay for 8CB and 8OCB across mesophases, and 1.2 ps for PCH5.

Overall, within the uncertainty the dynamics of all molecules are described by similar constants within this model. A clear trend universal for all samples is difficult to identify, other than possibly a decrease of τ_1 with decreased temperature which could be interpreted as a stronger damping of this relaxation path. Otherwise, the general picture is one in which the electronic response is responsible for 60% to 70% of the total amplitude, while the fast and and slow nuclear response share the rest with roughly 25%

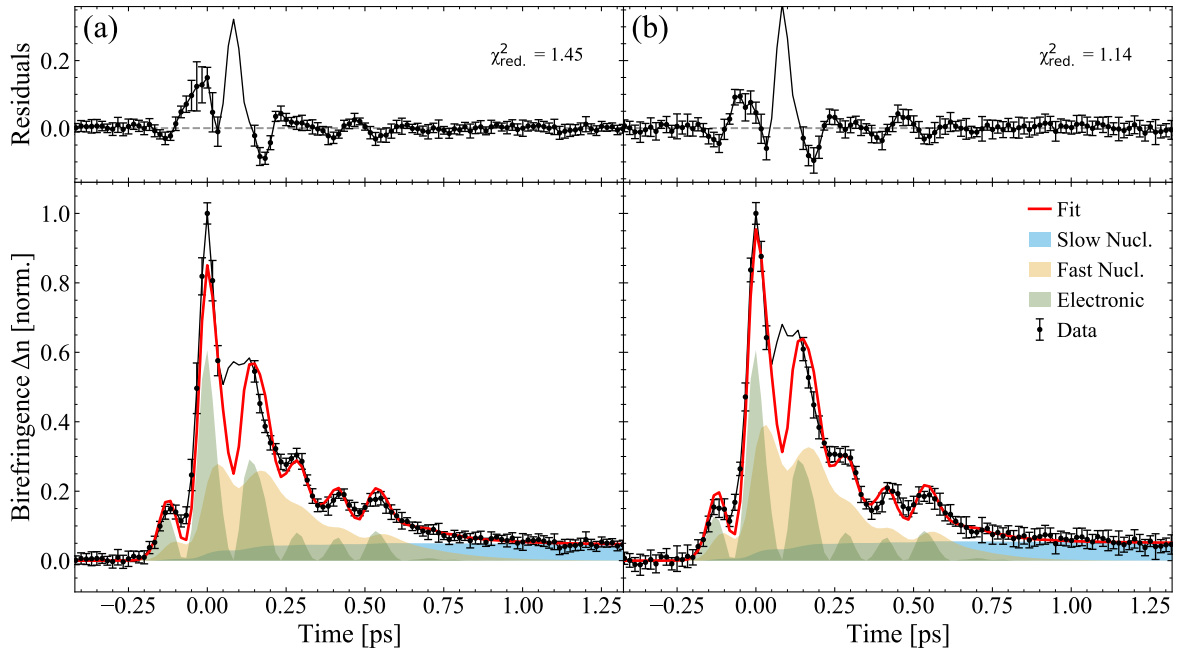

Figure 5.16.: Rotational diffusion fits to the PCH5 THz Kerr data, for (a) isotropic and (b) nematic mesophases. The top panel reports the residuals and the reduced $\chi^2_{red.}$. The bottom panel contains the experimental data (black) and the full fit (red). Additionally, the three individual terms of the model are plotted as shaded areas. Here, the identified peak out of phase with the THz peaks are excluded from the fits, and marked by missing error bars.

Table 5.3.: Fit parameters extracted for PCH5 for each mesophase.

Mesophase	τ_1 [ps]	τ_2 [ps]	$A_{el.}$	$A^{(1)}_{nucl.}$	$A^{(2)}_{nucl.}$
Isotropic	0.147±0.024	8.9 ± 32.9	0.622±0.038	0.279±0.024	0.051±0.013
Nematic	0.110±0.014	8.0 ± 23.0	0.622±0.039	0.391±0.029	0.056±0.010

to 35% and 5% to 10%. The fast nuclear relaxation takes place on 100 fs scales, while the slow relaxation on roughly 1 ps scales.

5.2.3. Discussion of the overall Kerr response

Any interpretation must reconcile the dynamical behavior of the THz Kerr traces with the scaling behavior for mesophase and molecular composition. Isolated dipoles interacting with the electric field alone are not sufficient to explain the observed dynamics, neither the amplitude between samples, since these values are not scaling as the Kerr traces. From the DFT analysis also permanent dipole moments are accessible, which give similar values of 6.22D for 8CB, 7.18D for 8OCB, and 5.94D for PCH5. The rota-

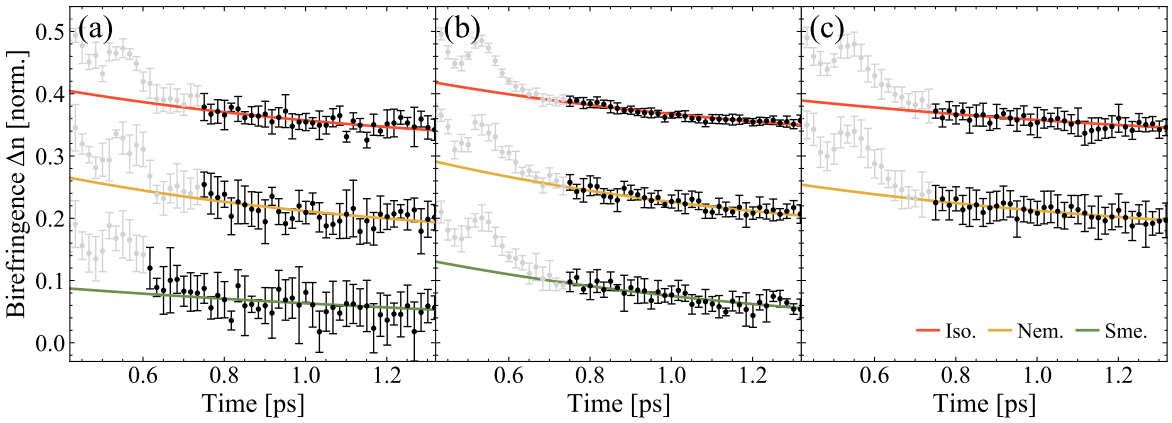

Figure 5.17.: Exponential fits to the THz field free decay for estimation of τ_2, for (a) 8CB, (b) 8OCB, and (c) PCH5. The data for each mesophase has been offset by a constant value of 0.15.

Table 5.4.: Slow relaxation constants τ_2, extracted from exponential fits to the THz free region after the main Kerr transients.

Mesophase	8CB τ_2 [ps]	8OCB τ_2 [ps]	PCH5 τ_2 [ps]
Isotropic	0.97 ± 0.15	1.044 ± 0.045	1.34 ± 0.15
Nematic	0.92 ± 0.20	0.942 ± 0.078	1.13 ± 0.12
Smectic	1.82 ± 0.63	1.05 ± 0.13	

tional diffusion model fitted to the data implies that related quantities are responsible for the observed behavior. Considering rotational viscosity (inversely proportional to the diffusion constant) one finds that the viscosity decreases with rising temperature for PCH5 [139], potentially explaining the scaling with mesophase. But comparing different species, the relationship is reversed, where PCH5 (80 mPa s [140]) is roughly half the value for 8CB (150 mPa s [141]).

The dominance of the electronic contribution identified by the fits, and the fast sub-picosecond time scales strongly hint at electronic effects as the major driver. Even though the electronic contribution has been discussed in terms of polarizability α, and even though the halving of the Kerr signal for PCH5 is strongly hinting at the lack of delocalized π electrons of the missing phenyl ring, this property alone cannot explain the observed behavior. Comparing the polarizabilities for all three species, one finds similar values (40 Å^3 for PCH5 [40] compared to about 45 Å^3 for 5CB [39] and 5OCB [40]). In fact, THz Kerr studies on water have identified the polarizability anisotropy (the difference in polarizability along the main axis against the polarizability perpendicular) as an important factor proportional to $\Delta n \propto \Delta\alpha$ [22, 24]. This could be seen as analogous to the Lorentz-Lorentz equation from classical electrodynamics, which relates the polarizability of a system, consisting of a number N of molecules, to its refractive index [39].

At 1.5 THz, polarizability anisotropies $\Delta\alpha$ have been reported from static TDS experiments (only in the nematic phase) of $0.7 \times 10^{-24}\,\mathrm{cm}^3$ [40] for PCH5, $0.77 \times 10^{-24}\,\mathrm{cm}^3$ [39] for 5CB, and $0.85 \times 10^{-24}\,\mathrm{cm}^3$ [40] for 5OCB. Furthermore, for the nCB series, a rising trend with chain length has been reported, where 6CB has a $\Delta\alpha$ of $0.72 \times 10^{-24}\,\mathrm{cm}^3$, and 7CB $0.88 \times 10^{-24}\,\mathrm{cm}^3$. On the other hand, the $\Delta n \propto \Delta\alpha$ relationship from static TDS birefringence implies a decrease in polarizability anisotropy with rising temperature, as reported in [39] and as expected from the same analysis performed on the refractive index data plotted in Figure 5.1. For the Kerr traces here, it is rising for mesophases located at higher temperatures.

The aligned exposure of the samples must play a role when discussing anisotropies. In the LC mesophases, the alignment director is pointing along the beam propagation direction. This means, all contributions of the long axis are given by projections due of thermal disorder, quantified by the order parameter S. This quantity shrinks with temperature in the mesophases, meaning larger projections of the long axis of the molecules are exposed to the beams. Finally, the isotropic phase, which consistently shows highest response, could be understood in terms of a rotational average over all molecular orientations. For this phase, all molecular axes are equally accessible on average, whereas in the aligned mesophases, the LC director is pointing along the beam propagation, effectively hiding the long molecular axis. Also the larger spread of peak values reported in Figure 5.12b for 8OCB compared to 8CB could be consistent with this picture, given the higher overall temperatures required to reach the 8OCB mesophases. For perfect alignment, the anisotropy seen by the beams would originate not from the backbone of the elongated molecules, but purely from the difference in in-plane polarizability, defined by the biphenyl plane, and the out-of-plane contribution.

Most likely, the full response is a combination of many effects. On short time scales electronic polarizabilities dominate, and the long term tail is defined by molecular rotational diffusion processes. The time scale for the fast nuclear relaxation of on the order of 100 fs, as modeled by the fits, stands out as significantly faster than other relaxation times reported for this class of experiments (typically picoseconds), hinting at the need for more sophisticated understanding.

5.2.4. Driven response

In the following, attention will be paid to the out of phase beat node within the oscillating part of the Kerr response. In principle, this response can have its origin in the sample dynamics, or in systematic effects in the measurement apparatus. The three most immediate explanations are multiple internal reflection of one of the pulses, possible cell window responses, and propagation effects, each of which will be discussed individually in the next paragraphs.

5.2.4.1. Possible technical origins

Internal reflections
Since the experiment is performed in transmission geometry at normal incidence, multiple internal reflections naturally occur. In principle, two distinct pulses can bounce within two interfaced layers through Fresnel reflection, either the cell window or the sample layer itself, and accumulate signal. Using the peak of the Kerr response and the THz pulse trace as arbitrary time zero references, the possible artifact shows up in the data at approximately 70 fs. Using the refractive indices for the NIR and THz pulses in the sample and SiN membranes and the nominal thicknesses, the artifact is expected to appear at the relative times listed in Table 5.5. From these estimations in comparisons with the real data, it is justified to exclude multiple internal reflections as the culprit generating the signal.

Table 5.5.: Estimated internal reflection time delays. Values taken from literature are accompanied by the reference. The time delay is calculated by $\Delta t = \frac{2dn}{c}$.

Interaction	Thickness d [µm]	Ref. index n	Time Delay Δt [fs]
IR probe in SiN	0.5	2.0 [142]	6.7
IR probe in LC	100	1.55	1030
THz in SiN	0.5	2.7 [124, 143]	9.0
THz in LC	100	1.55	1030

Propagation effects
Lastly, propagation effects require discussion. Here, one should distinguish two possibilities. Firstly, velocity mismatch between pump and probe pulses, and secondly, change of the pump pulse shape as it propagates through the sample. Velocity mismatch can be quickly discarded, because, as seen in Chapter 4, it leads to a smearing out of the full oscillatory response, up to a fully washed out square signal in the most extreme cases. Furthermore, the coherence length $l_c = c/(2\nu_{\mathrm{THz}}|n_{\mathrm{group}}^{\mathrm{probe}} - n_{\mathrm{THz}}|)$ over which both pulses can be considered to be in phase [73] is orders of magnitude larger than the sample thickness. For PCH5, for which $n_{\mathrm{group}}^{\mathrm{probe}} = 1.51$ is easily accessible [65], the coherence length is $l_c = 1.67\,\mathrm{mm}$.

On the other hand, a change in driving pulse shape has to be taken seriously. Not because nonlinear effects, such as self phase modulation (SPM) or wave mixing processes

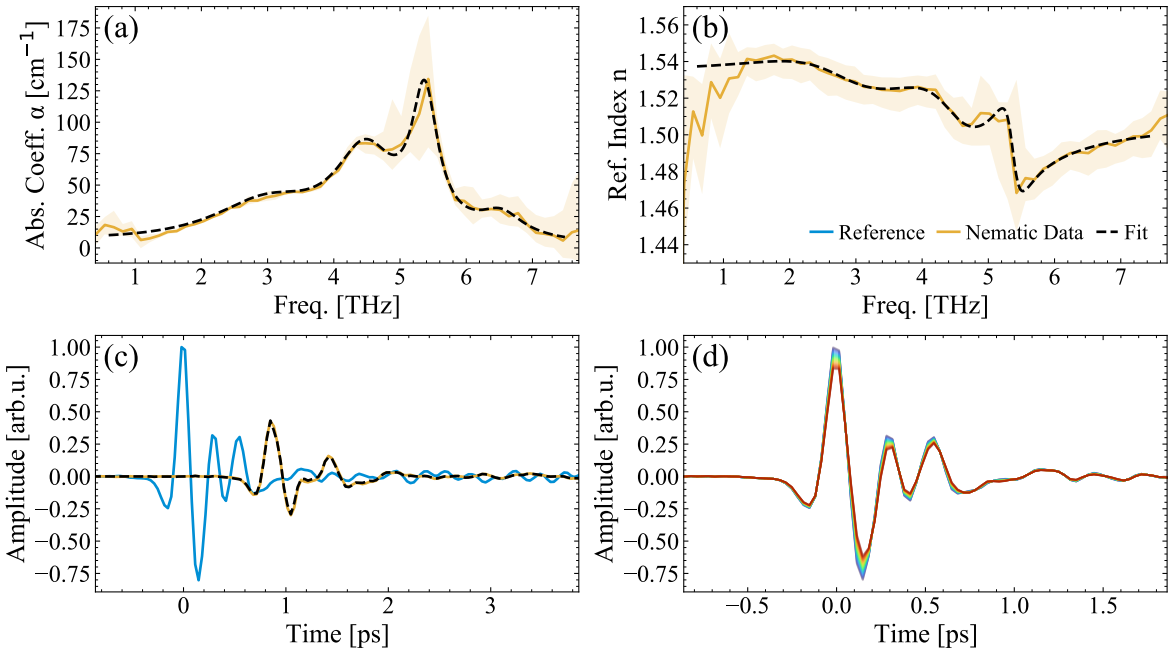

Figure 5.18.: Measured and fitted (a) absorption coefficient and (b) refractive index for the nematic phase of 8CB as input into the propagation tests. (c) Reference, sample, and predicted THz traces after a thick TDS cell. (d) Set of predicted traces as propagated through the thin Kerr cell from blue (before the sample) to red (after the sample). In a thin cell the THz pulse shape is negligibly affected.

are expected to be present, since the field strengths are still too weak, but linear absorption takes place. The sample is oriented with its ordinary axis to the THz polarization plane, therefore, as described in detail in Chapter 3.3, with depleted frequency content over the propagation distance, the THz pulse shape can change significantly.

THz time domain techniques are powerful, because they give straightforward access to absorbance and phase, as discussed in Chapter 3.1.2. This information, extracted from the TDS analysis, can be exploited in this analysis by using it to model the THz pulse shape for every propagation step through the sample numerically. This numerical modeling is based on empirical fits to the absorption curves and the refractive index data, extracted from the TDS analysis. The absorption is modeled by a sum of four Lorentz absorption lines, while the refractive index is modeled with the associated dispersion curves (although with its own free fitting parameters), as shown in Figure 5.18a and b. The reference and sample THz traces are the perfect test cases for this approach. (Even though it's following circular logic, where the time traces are used to extract absorbance and refractive index, and those are then used here to calculate back the trace propagated through the sample. Strictly speaking, this approach is testing for the quality of the empirical fits.) The sample thickness in the TDS experiments is 500 µm, while in the THz Kerr measurements it is 100 µm, hence it is possible to reconstruct the traces after propagation (which have not been measured in parallel), and all positions

within. The propagation is done numerically, in the following sequence of steps: (i) FFT into frequency domain, (ii) application of propagation step for absorption and phase via Lambert-Beer, (iii) FFT back into time domain. In order to produce an average driving field that would be seen by the probe pulse after the propagation through the sample, all modeled time traces within the propagation distance are averaged (with appropriate fine sampling, and global delay removed via subtraction of the linear phase in frequency domain, because the THz pulse is velocity matched with the probe pulse propagation.). The resulting traces after 100 µm sample thickness are only weakly different to the input traces, as seen in Figure 5.18d. Hence, propagation cannot account for the artifact, and for the THz Kerr effect analysis the input traces are deemed sufficient.

Cell window response
As discussed in Chapter 4, careful attention was paid on minimizing the response of the cell window material relative to the desired sample response. While the design based on SiN membranes has been a good path forward, it is not strictly speaking true that SiN shows zero response, and should be checked by placing an empty reference cell in the setup. The measured response is barely rising beyond the noise level, as seen in Figure 4.2. Additionally, given the solid state nature of the SiN window, it is not expected to accumulate any delay compared to the THz time trace, that could explain the out of phase nature of the measurement artifact.

5.2.4.2. Origin in sample dynamics

Since possible technical artifacts are excluded, the response is assumed to be genuine sample dynamics. The main indication lies in the relative scaling with the LC mesophase. While the global response is shrinking in amplitude with the lower lying mesophases (higher order), the out of phase peak is growing comparatively, as is evident from Figure 5.19 and 5.20, in which the normalized traces are overlaid. This behavior is consistent for all three molecular species under investigation, which means it is reproducible over multiple days of measurement and different hand build sample cells. Furthermore, within each sample measurement run, the beam alignment has not been affected, since only the temperature was adjusted.

The hypothesis for this behavior reads as follows: The resonant driving field is activating an IR active vibrational mode when the associated transition dipole moment has the right orientation with respect to the excitation polarization, as has been discussed in section 5.1. Therefore, the more ordered mesophases possess a higher fraction of excited active units. The associated vibrational mode has to influence the birefringence properties of the sample, otherwise it wouldn't show up in the Kerr traces, and, if it is intermolecular, it will involve only a limited number of molecules within a driven unit, since the response is present (although less strong) in the isotropic phase, where long range correlations are significantly shorter compared to the ordered LC phases. The following assumption is that this vibrational mode is primarily associated with the lowest lying frequency mode found in the TDS absorption spectra, where simple gas phase assignment has not been possible. If true, this would be a clear demonstration

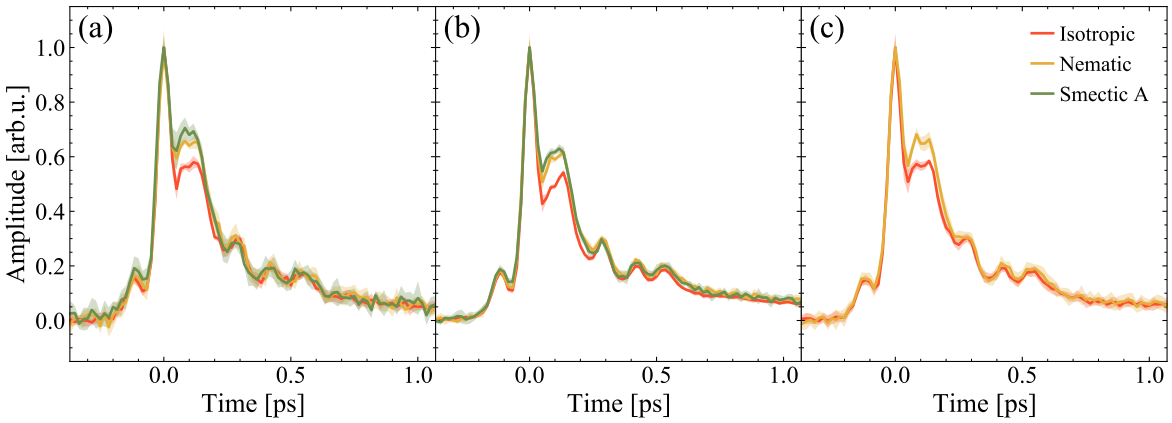

Figure 5.19.: The THz Kerr traces for the different thermodynamic phases (isotropic red, nematic yellow, smectic A green) at the same THz field strength, normalized and overlapped. The shaded area represents the experimental uncertainty in the form of the standard deviation of the measurements. (a) 8CB, (b) 8OCB, and (c) PCH5

that macroscopic material properties can be controlled on ultrashort time scales though vibrational excitation on the molecular level.

5.2.5. Lorentz oscillator picture of the driven response

The goal is to establish a conceptual bridge between the assigned intermolecular mode in the TDS spectra, and the coherent bulk response in the resonantly pumped case, in order to validate the hypothesis stated above. In the following, the signal needs to be isolated from the rest of the understood Kerr response, modeled in a simplified framework, and tested by prediction of the response under new conditions.

5.2.5.1. Signal isolation

Since the response is composed of mainly one oscillation, meaning since it is heavily damped, working with Fourier analytical methods is less practical than in cases where oscillations are sustained for multiple periods. Instead, in a first order approach, one can take advantage of the less efficient excitation in the isotropic mesophase and use it as a pseudo-reference for the two ordered phases. Here, the isolated signal is extracted from subtraction with the isotropic pseudo-reference. The results for all three tested molecular species are transient signals as shown in Figure 5.21.

5.2.5.2. Modeled response

The goal is to describe the system in terms of the known absorption spectrum from the TDS measurements and to drive it with the THz traces measured in the experimental setup. The simplest yet powerful approach towards this goal is through a Lorentz

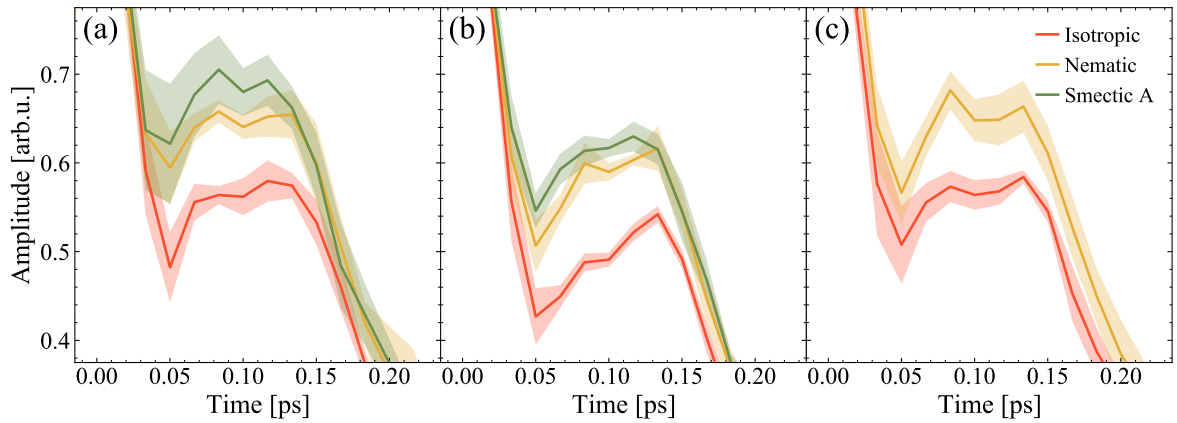

Figure 5.20.: The same data as shown in Fig. 5.19, with a zoom into the region of interest, highlighting the increased driving of the response under investigation with the more ordered states. (a) 8CB, (b) 8OCB, and (c) PCH5

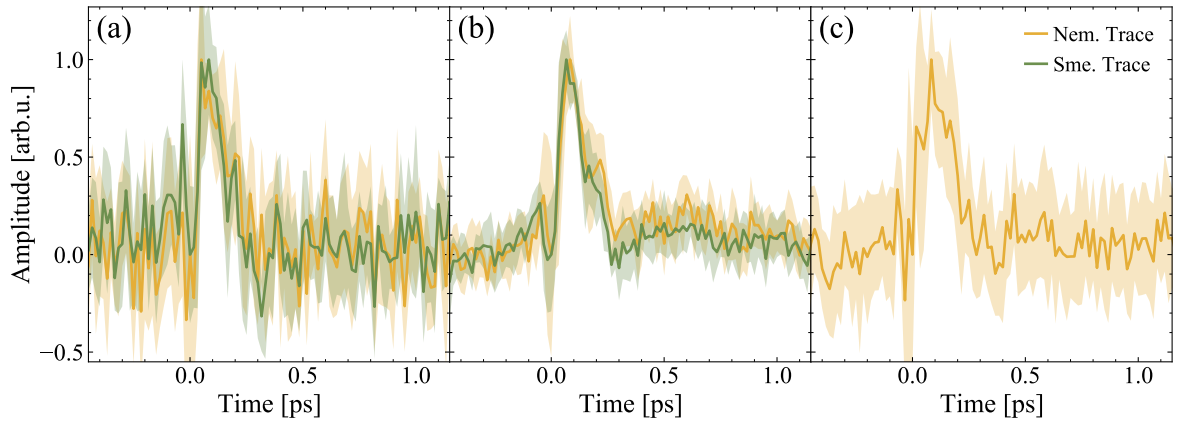

Figure 5.21.: The isolated coherently driven responses, extracted from the traces shown in 5.19 by subtraction of the ordered LC phases with the isotropic reference for (a) 8CB, (b) 8OCB, and (c) PCH5. The traces are isolated for both LC phases individually and normalized to show the dynamics. The shaded are represents the uncertainty as the standard deviation.

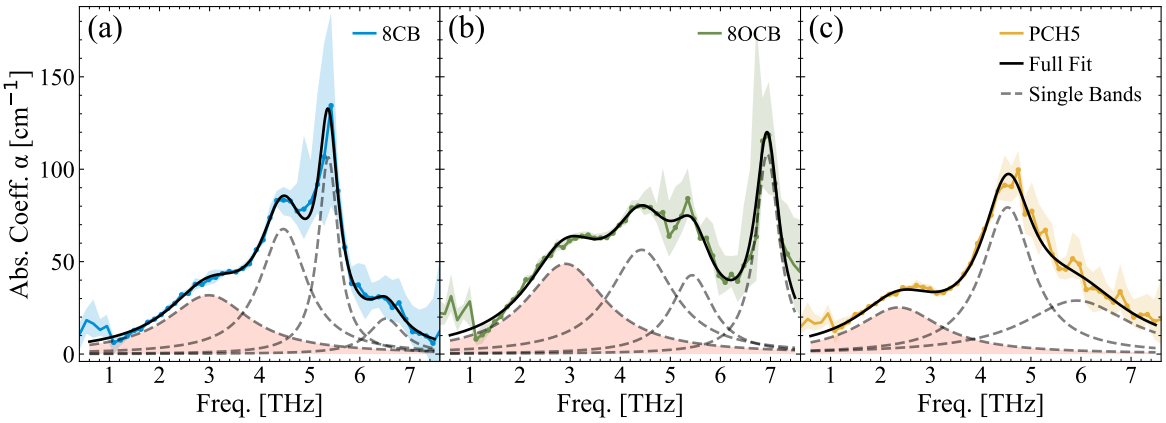

Figure 5.22.: Fit to the TDS spectra of (a) 8CB, (b) 8OCB, and (c) PCH5 from section 5.1. As an empirical description, a sum of Lorentzian line shapes is fitted to the absorption spectra (bold black line), as a guide to the eye the individual line shapes are plotted in gray dashed lines. The lowest lying line (in red highlight) is used as input into the model with its fitted position and width.

oscillator description, in which the system is assumed as a damped driven classical harmonic oscillator. While the ordinary absorption in the sample is quite complex, here it is constrained to the lowest lying band, with the justification that it is the most clearly intermolecular mode.[3] The natural frequencies and the damping ratios are taken from the Lorentz fits associated with this band, which are presented in Figure 5.22. On the other side of the equation is the driving force, which in principle is proportional to the electric field, when thinking of a dipole active mode. Given the geometry of the pulse polarizations with respect to the homeotropic sample alignment, the sample appears centrosymmetric. Therfore, only higher order terms of the potential energy surface will be probed, which is accounted for by a square excitation in the driving term. The full model description is given by equation 5.3.

$$\frac{d^2x}{dt^2} + 2\xi\omega_0\frac{dx}{dt} + \omega_0^2 x = E_{\mathrm{THz}}^2(t) \tag{5.3}$$

In this damped and driven harmonic oscillator equation, ξ stands for the damping ratio, which is related to the width Γ of the resonance by $\Gamma/2\omega_0$, and ω_0 is the natural frequency of the undamped, undriven system. The right hand side of the equation represents the force term in the form of quadratic driving $\frac{F(t)}{m} = E_{\mathrm{THz}}^2(t)$, and the differential equation is solved numerically.

The justification for the force term set to be proportional to $E_{\mathrm{THz}}^2(t)$ derives from the general solution of anharmonic oscillator equations with third order terms in the potential energy surface $U(x) = \frac{1}{2}m\omega_0 x^2 + \frac{1}{3}m\alpha x^3$ (with α small) that leads to the

[3]Note: Such a clear distinction is a poor description of reality in this frequency range. Yet, for this simplified picture, it is a sufficient approximation.

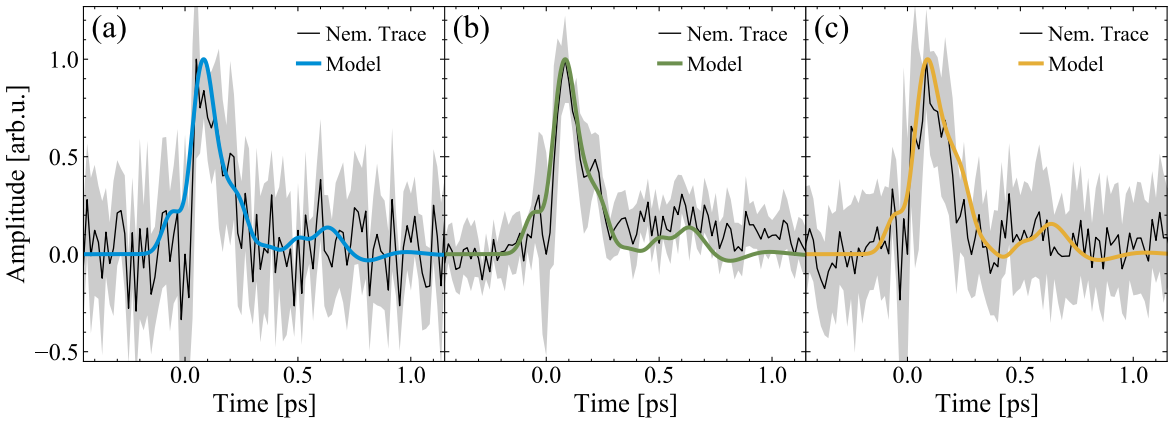

Figure 5.23.: The prediction of the oscillator model, using the lowest absorption band as input, overlayed on the data presented in Fig. 5.21

following generalized from with arbitrary driving force $F(t)$ in equation 5.4.

$$\frac{d^2x}{dt^2} + 2\xi\omega_0\frac{dx}{dt} + \omega_0^2 x + \alpha x^2 = \frac{F(t)}{m} \tag{5.4}$$

One way to solve this differential equation is to perturbatively expand the solution $x(t) = \sum_{n=1}^{\infty} \epsilon^n x_n(t)$ and insert into equation 5.4. The result is a set of hierarchical differential equations, with the first and second orders reading as [73]:

$$\frac{d^2x_1}{dt^2} + 2\xi\omega_0\frac{dx_1}{dt} + \omega_0^2 x_1 = \frac{F(t)}{m} \tag{5.5}$$

$$\frac{d^2x_2}{dt^2} + 2\xi\omega_0\frac{dx_2}{dt} + \omega_0^2 x_2 = -\alpha x_1^2 \tag{5.6}$$

The first equation 5.5 is the well known unperturbed damped driven harmonic oscillator with its known solution that depends on $F(t)$ and an amplitude depending on ω, ω_0, and $\xi = \Gamma/2\omega_0$. The second equation 5.6 takes the same shape, with the difference lying in the force term, which is now dependent on the square of the solution $x_1(t)$ of equation 5.5, meaning it's proportional to $E^2_{\mathrm{THz}}(t)$.

The results for the three LC systems under investigation are the traces shown in Figure 5.23. It shows the same experimentally isolated traces as in Figure 5.21 overlapped with modeled responses (including normalization), and within the uncertainty the behavior is reproduced. Note, that no scaling or shifting along the time axis is applied. The modeled traces capture the dynamics very well, which are a consequence of the resonant driving of the intermolacular modes assigned from the TDS results.

5.2.5.3. Pulse shape variation

In order to test this model, it is instructive to categorize the inputs to the oscillator model. On one side of equation 5.3 is the harmonic oscillator term with its natural

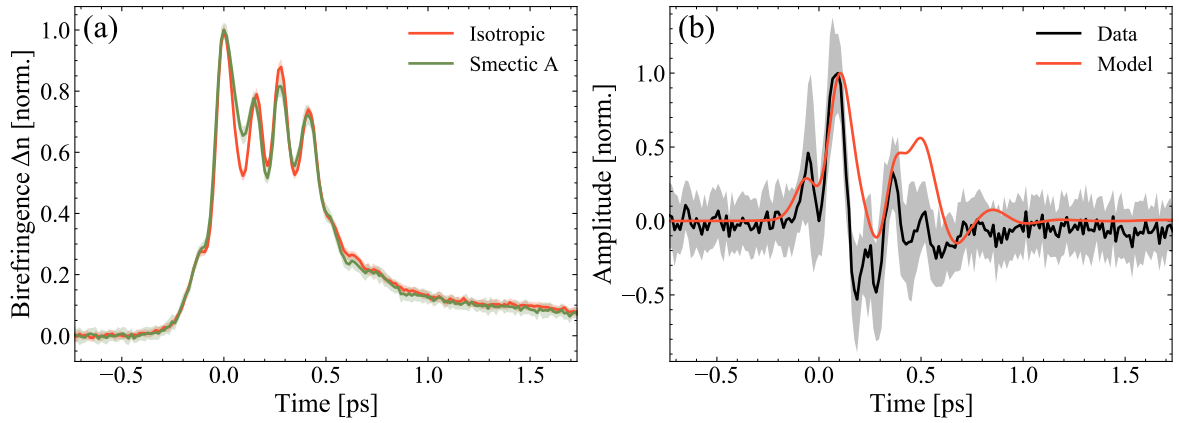

Figure 5.24.: (a) Full PNPA driven THz Kerr responses for isotropic and smectic phases of 8OCB. (b) The isolated coherently driven response and the model prediction as normalized traces for comparison.

frequency and damping term. This part is a simplified description of the material parameters inherent to the LC samples under investigation. On the other side is the external force term, given by the THz pulses, as generated in the setup. In the cases above, the same force terms has been used, and the material parameters could only be varied by exchange of LC sample. The validity of this model hinges on the question, whether for a given material it can predict its behavior under different resonant driving conditions.

Applying pure and filtered PNPA driving fields as presented in section 3.2.1 to one LC system, here confined for simplicity to 8OCB, the measured results are significantly different, allowing for a reliable test of this model. The strong modification between driving fields comes from the strong sensitivity of the ideal harmonic oscillators to different resonance conditions of the force term. Furthermore, only the isotropic (as the pseudo-reference) and the smectic A phases are measured (most ordered, strongest driven signal), and the nematic phase is disregarded in favor of larger statistics in the measured phases. Figures 5.24 and 5.25 show the total measured responses in panel (a) and the isolated driven response with the modeled response overlayed in panel (b) for all three tested driving fields.

Looking at the full PNPA driving first, the overall shape of the total Kerr response is different, as expected for the changed driving field, and the driven response is significantly altered. It is extended longer in time, and undergoes stronger oscillations, as will be quantified below. It's worth noting that this difference between isotropic and smectic A response is the largest effect recorded among all parameters investigated. The isolated response from subtraction and the results of the driven model are capturing comparable overall dynamics, even though larger discrapancies remain than in the DSTMS cases. Similar conclusions hold for the two narrowband cases using bandpass filters to further shape the driving field.

The 3.75 THz and 1.5 THz responses required significantly more statistics in order to

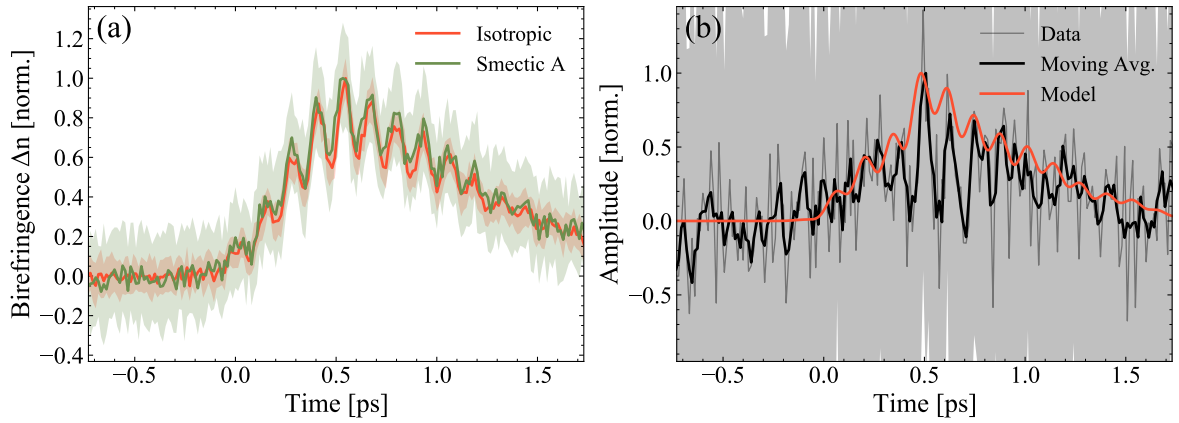

Figure 5.25.: (a) 3.75 THz *Kerr responses for isotropic and smectic phases of 8OCB. (b) The isolated coherently driven response and the model prediction as normalized traces for comparison. Note: given the large uncertainty, a moving average has been applied on the isolated trace for improved readability.*

make statements about the differences, as reflected in the confidence bands. Yet for the higher frequency experiment (with higher electric field strengths), a noisy response could be isolated. The lower frequency response, on the other hand, would require unfeasibly more statistics, and is just reported "for completeness" in Appendix B. These two cases are instructive, since they reflect in one case a resonant driving over many oscillation periods, and once an off resonant driving (at roughly the FWHM point of the modeled Lorentz oscillator absorption curve). Focusing the discussion only on the higher frequency case, one can see subtle changes between the mesophases, mostly in the out of phase parts of the oscillations.

A few aspects in this analysis deserve discussion. Firstly, the comparison between experiment and model strictly speaking does not hold. The model is supposed to give the pure driven response of the system, while the isolated response is extracted from subtraction with the isotropic phase, which is not free from driven signal. This low level extraction is a defensible approach, as long as the response only scales in amplitude. From the analysis of the DSTMS driven experiments, this behavior appears to be a valid assumption. Furthermore, the subtraction of two normalized traces at time zero leads to the traces clamped to zero in this point in time. This approach explains both the subtle offset seen in some of the traces after the response, and a part of the high frequency modulation in the PNPA driven trace.

One should not overstate the amount of information one can extract from this model. It's main purpose is to establish a conceptual bridge between the resonantly driven response seen in the transient Kerr measurements and the lowest absorption band in the TDS spectra, which was assigned to mainly intermolecular vibrational modes.

It would be instructive to drive these modes completely off-resonantly, in order to kill this response, and leave only the typical Kerr traces. For instance, from broadband THz spectroscopy, these samples are known to have a transparency window between 8 THz to

12 THz. Performing the same experiment there should not yield any additional driven features, if the picture presented here is (empirically) valid.

5.2.6. In summary

When the THz acts as a strong pump on these systems, it responds with transient modulation of the macroscopic refractive index on sub-picosecond time scales, as measured in the THz-Kerr measurement scheme. Overall, the traces follow a rotational diffusion model, but include additional effects stemming from the resonant nature of the THz driving pulses with the intermolecular modes.

Between samples and mesophases, the dynamics remain universal and only differ in amplitude. This is a reflection of the electronic properties of the systems, which are expected to dominate on these short time scales. Particularly the electronic polarizability and its anisotropy are connected with the observations. The scaling of these traces is thought to be a consequence of the alignment with respect to the beam propagation, and the orientational order. The two relaxation terms contributing to the measured response are consistent with the rotational diffusion model. Although 100 fs time scales are fast for nuclear movement, it is reasonable to expect two constants, reflecting the strong anisotropic shape of the molecules.

The additional effect seen within the THz Kerr trace appears out of phase with the expected modulations. Within the Lorentz oscillator model, this response is connected to the intermolecular modes identified in the TDS spectra, and therefore interpreted as a coherent driving of these dynamics with macroscopic impact. The underlying dynamics must involve a small number of neighboring molecules, since the effect remains measurable in the isotropic phase.

6. Conclusions & outlook

The research question motivating this work revolves around the interplay between collective molecular order and the vibrational response of the system. On one hand, how does the molecular arrangement impact on the THz spectra, which are expected to be sensitive to intermolecular effects? And on the other hand, does the molecular structure impact on this relationship? Furthermore, can these long-range intermolecular vibration be driven resonantly, in order to modify macroscopic bulk properties transiently?

The THz spectra for all three molecular species investigated are characterized by two aspects. Firstly, at higher frequencies the spectra are well described by gas phase DFT calculations and their vibrational modes can be assigned. Therefore, these modes are interpreted as intramolecular modes. Secondly, the low-frequency mode is deviating from the calculations for every sample, hinting at its intermolecular nature. The low-frequency trend seen in the cluster calculations supports this assignment.

Within the context of the research questions, the changes in molecular arrangement have little influence over the overall shape of the observed spectra. At higher frequencies, the modes remain dictated by the response of individual molecules, and at lower frequencies the broad intermolecular peak shows weak modification in amplitude only, most likely related to trends in density and order parameter. Overall, the samples behave like disordered molecular fluids, with a broad intermolecular vibrational band and intramolecular modes present simultaneously in the accessible bandwidth of the TDS experiment. Particularly the lack of distinct change for the smectic phase along the extraordinary axis (along the layering) is surprising, but most likely an expression of the inherently disordered arrangement within the layers.

When the THz acts as a strong pump on these systems, it responds with transient modulation of the macroscopic refractive index on sub-picosecond time scales, as measured in the THz-Kerr measurement scheme. Overall, the traces follow a rotational diffusion model, but include additional effects stemming from the resonant nature of the THz driving pulses with the intermolecular modes.

In terms of the modeled response, the dynamics remain unchanged for different samples and mesophases, and only differ in amplitude. This is a reflection of the electronic properties of the systems, which are expected to dominate on these short time scales. Particularly the electronic polarizability and its anisotropy are connected with the observations. The scaling of these traces is thought to be a consequence of the alignment with respect to the beam propagation, and the orientational order. The two relaxation terms contributing to the measured traces represent rotational diffusion effects of the model. While the relaxation on 100 fs time scales is fast, the presence of a slow and fast one is reasonable, given the strong anisotropy of the molecules. These dynamics are known effects in liquids and don't seem to be connected to the molecular arrangement,

as presented in the LC mesophases.

The additional effect seen within the THz Kerr trace appears out of phase with the expected modulations, and importantly increases in relative strength with the more ordered mesophases. This response is connected to the intermolecular vibrational mode in the TDS spectra with the Lorentz oscillator model, and therefore interpreted as a coherent driving of these dynamics with macroscopic impact. A change of driving pulse leads to responses similar to the toy model prediction, supporting the interpretation as a real response of the sample. The report of a strongly damped 3 THz oscillation seen in Raman induced Kerr spectroscopy [33], as mentioned in the introductory chapter, could have the same origin and supports this observation.

Given the presence of this signal in all mesophases including the isotropic one, with stronger relative amplitude for more ordered states, the underlying dynamics are thought to involve a small number of neighboring molecules. The transition dipole moment of the mode is oriented along the THz polarization direction and the LC mesophases contain a higher fraction of these units with the correct orientation.

It remains difficult to make definitive statements about the microscopic nature of the intermolecular modes at THz frequencies. The microscopic descriptions of these broad low frequency bands depends on the nature of the sample. From a liquid perspective, Poley absorption or librational modes are generating similar absorption features. Amorphous solids on the other hand are described in terms of the VDOS where phonon modes cannot be sustained over large coherence lengths. In any case, condensed phase molecular dynamics calculations are needed to make definitive assignments. Unfortunately, in such disordered or loosely ordered systems, such simulations are computationally expensive.

A full simulation would provide two advantages. Firstly, it would confirm the high-frequency assignment of the intramolecular modes. Secondly, it would guide the interpretation of the low-frequency intermolecular absorption band. This, in turn, will give insights into the microscopic nature of the driven response seen in the THz Kerr experiments. While the transient modification of the birefringence on these time scales is promising, the goal remains to extend this work into more complex systems.

The molecules investigated within this thesis represent LC benchmark systems. They are well studied, easily available off the shelf, and mostly used as tunable phase shifters due to their static birefringence. But, beyond these LC systems, there exists a broad range of more complex molecules presenting different LC mesophase behavior, and therefore different collective arrangement. Some have been shown to possess considerable charge transport properties, along specific directions. While these low frequency modes often disrupt these properties (dynamic disorder), there are studies reporting enhanced transport driven by low frequency modes [144]. Identification and exploitation of these dynamics to create organic ultrafast switchable charge transport materials represents the ideal outcome of this line of work.

On the path towards this goal, a number of options are available, both in terms of verification and extension. The connection of the driven nonlinear response, seen under strong THz fields, to the intermolcular mode implies that a field dependent TDS study should reveal changes in the absorption line shape with increasing field strength.

Initial test measurements have been performed which have shown systematic changes in amplitude, but they remain inconclusive. So far, reproducibility has not been possible, due to saturation issues in the detection. These are a technicality, and are solvable within the existing setup.

From the THz Kerr experiment perspective, driving these modes in fully narrowband condition would provide mode selectivity. Hence, the toy model could be tested against specific resonant and offresonant driving conditions. Furthermore, the intramolecular modes could be specifically targeted, in order to confirm their (lack of) response. Accelerator based facilities are able to provide such bright CEP stable, narrowband, and tunable THz radiation, such as the TELBE/FELBE accelerators at the Helmholtz Zentrum Dresden Rossendorf (HZDR) [83, 84].

Structural (nuclear) effects can be isolated from time resolved X-ray diffraction studies. While Synchrotron sources can provide picosecond pulse durations, Free Electron Laser (FEL) facilities can reach femtoseconds, making them suitable for such experiments. The experimental scheme would involve a THz pump pulse, followed by a delayed X-ray pulse, and its diffracted photons are detected. Depending on the sample, different diffraction geometries can be chosen, such as the diffusive scattering in transmission or the Bragg reflection condition, both depicted in Figure 2.4. Here, the challenge lies in sample delivery, since X-ray radiation leads to photodissociation. this is especially true for the hard X-rays, if vacuum environments are avoided, since soft X-rays don't travel in atmosphere. Typically, samples are refreshed, either through flow or raster sampling. In any case, the static cell design taken within this work is inadequate and requires new solutions.

Coupling between vibrational modes leads to energy dissipation in a system. Such coupling pathways are investigated though two dimensional spectroscopy schemes [145]. A 2D-THz experiment could give information, if energy is transferred from an intramolecular mode to the collective mode, or the other way around. Furthermore, different combinations of different central frequencies and bandwidths allow to sample a wide range of modes, including localized MidIR vibrations (compare Figure 3.16). Still within the original research question, one could ask how the collective molecular arrangement influences these pathways, and if the branching ratios remain constant for different molecular order, or if certain arrangements favor different paths.

Alternatively, time resolved THz spectroscopy is used to investigate excited state dynamics and its influence on THz frequency properties. One class of such experiments fits into the outlook toward charge transport modification, and would act as a stepping stone towards this goal. Using ultrafast UV-Vis excitation as a pump, which injects charges into the system, the THz-TDS spectrum is monitored as function of relative time delay. By tracking the spectral amplitudes and decay times (or sometimes simply the peak of the transmitted pulse in time domain), one can infer the complex conductivity of the system, in an all-optical and contact-free experiment. These types of measurements have been performed on solid state [146] and liquid samples [147].

The results of the work presented within this thesis are promising, but challenges remain in the exact interpretation of the intermolecular dynamics on a microscopic level. Nevertheless, it does represent a stepping stone towards THz control of molecular

collective dynamics and their macroscopic material properties.

Bibliography

[1] P. G. De Gennes and J. Prost. *The Physics of Liquid Crystals*. Oxford University PressOxford, 1993.

[2] D. Andrienko. Introduction to liquid crystals. *Journal of Molecular Liquids*, 267:520–541, 2018.

[3] M. T. Ruggiero. Invited review: Modern methods for accurately simulating the terahertz spectra of solids. *Journal of Infrared, Millimeter, and Terahertz Waves*, 41(5):491–528, 2020.

[4] T. Huber, M. Ranke, A. Ferrer, L. Huber, and S. L. Johnson. Coherent phonon spectroscopy of non-fully symmetric modes using resonant terahertz excitation. *Applied Physics Letters*, 107(9), 2015.

[5] M. T. Ruggiero, J. Sibik, J. A. Zeitler, and T. M. Korter. Examination of L-glutamic acid polymorphs by solid-state density functional theory and terahertz spectroscopy. *The Journal of Physical Chemistry A*, 120(38):7490–7495, 2016.

[6] M. Witko, E and T. M. Korter. Investigation of the low-frequency vibrations of crystalline tartaric acid using terahertz spectroscopy and solid-state density functional theory. *The Journal of Physical Chemistry A*, 115(35):10052–10058, 2011.

[7] C. J. Strachan, P. F. Taday, D. A. Newnham, K. C. Gordon, J. A. Zeitler, M. Pepper, and T. Rades. Using terahertz pulsed spectroscopy to quantify pharmaceutical polymorphism and crystallinity. *Journal of Pharmaceutical Sciences*, 94(4):837–846, 2005.

[8] J. A. Zeitler, D. A. Newnham, P. F. Taday, T. L. Threlfall, R. W. Lancaster, R. W. Berg, C. J. Strachan, M. Pepper, K. C. Gordon, and T. Rades. Characterization of temperature-induced phase transitions in five polymorphic forms of sulfathiazole by terahertz pulsed spectroscopy and differential scanning calorimetry. *Journal of Pharmaceutical Sciences*, 95(11):2486–2498, 2006.

[9] N. Juneja, J. L. Hastings, W. B. Stoll, W. W. Brennessel, S. Zarrella, P. Sornberger, L. Catalano, T. M. Korter, and M. T. Ruggiero. Fundamentally intertwined: anharmonic intermolecular interactions dictate both thermal expansion and terahertz lattice dynamics in molecular crystals. *Chemical Communications*, 60(84):12169–12172, 2024.

[10] M. D. King, W. D. Buchanan, and T. M. Korter. Understanding the terahertz spectra of crystalline pharmaceuticals: Terahertz spectroscopy and solid-state density functional theory study of (s)-(+)-ibuprofen and (rs)-ibuprofen. *Journal of Pharmaceutical Sciences*, 100(3):1116–1129, 2011.

[11] P. A. Banks, A. M. Dyer, A. C. Whalley, and M. T. Ruggiero. Side-chain torsional dynamics strongly influence charge transport in organic semiconductors. *Chemical Communications*, 58(92):12803–12806, 2022.

[12] P. A. Banks, G. D'Avino, G. Schweicher, J. Armstrong, C. Ruzié, J. W. Chung, J.-I. Park, C. Sawabe, T. Okamoto, J. Takeya, H. Sirringhaus, and M. T. Ruggiero. Untangling the fundamental electronic origins of non-local electron–phonon coupling in organic semiconductors. *Advanced Functional Materials*, 33(38), 2023.

[13] B. M. T. C. Peluzo, R. Meena, L. Catalano, G. Schweicher, and M. T. Ruggiero. Exploring the interplay of lattice dynamics and charge transport in organic semiconductors: Progress toward rational phonon engineering. *Angewandte Chemie International Edition*, 64(26), 2025.

[14] J. Sibik, K. Löbmann, T. Rades, and J. A. Zeitler. Predicting crystallization of amorphous drugs with terahertz spectroscopy. *Molecular Pharmaceutics*, 12(8):3062–3068, 2015.

[15] J. Sibik and J. A. Zeitler. Terahertz response of organic amorphous systems: experimental concerns and perspectives. *Philosophical Magazine*, 96(7–9):842–853, 2015.

[16] P. Bawuah and J. A. Zeitler. Advances in terahertz time-domain spectroscopy of pharmaceutical solids: A review. *TrAC Trends in Analytical Chemistry*, 139:116272, 2021.

[17] E. P.J. Parrott and J. A. Zeitler. Terahertz time-domain and low-frequency raman spectroscopy of organic materials. *Applied Spectroscopy*, 69(1):1–25, 2015.

[18] J. Kölbel, W. Schirmacher, E. Shalaev, and J. A. Zeitler. Terahertz dynamics in the glycerol-water system. *Physical Review B*, 107(10):104203, 2023.

[19] H. Elgabarty, T. Kampfrath, D. J. Bonthuis, V. Balos, N. K. Kaliannan, P. Loche, R. R. Netz, M. Wolf, T. D. Kühne, and M. Sajadi. Energy transfer within the hydrogen bonding network of water following resonant terahertz excitation. *Science Advances*, 6(17), 2020.

[20] J. P. Poley. Microwave dispersion of some polar liquids. *Applied Scientific Research, Section B*, 4(1):337–387, 1955.

[21] M. C. Hoffmann, N. C. Brandt, H. Y. Hwang, K.-L. Yeh, and K. A. Nelson. Terahertz kerr effect. *Applied Physics Letters*, 95(23), 2009.

[22] M. Sajadi, M. Wolf, and T. Kampfrath. Transient birefringence of liquids induced by terahertz electric-field torque on permanent molecular dipoles. *Nature Communications*, 8(1), 2017.

[23] T. Kampfrath, R. K. Campen, M. Wolf, and M. Sajadi. The nature of the dielectric response of methanol revealed by the terahertz kerr effect. *The Journal of Physical Chemistry Letters*, 9(6):1279–1283, 2018.

[24] P. Zalden, L. Song, X. Wu, H. Huang, F. Ahr, O D. Mücke, J. Reichert, M. Thorwart, P. K. Mishra, R. Welsch, R. Santra, F. X. Kärtner, and C. Bressler. Molecular polarizability anisotropy of liquid water revealed by terahertz-induced transient orientation. *Nature Communications*, 9(1), 2018.

[25] T. Kampfrath, M. Wolf, and M. Sajadi. The sign of the polarizability anisotropy of polar molecules is obtained from the terahertz kerr effect. *Chemical Physics Letters*, 692:319–323, 2018.

[26] M. Evans, M. Davies, and I. Larkin. Molecular motion and molecular interaction in the nematic and isotropic phases of a liquid crystal compound. *Journal of the Chemical Society, Faraday Transactions 2*, 69:1011, 1973.

[27] G. J. Evans and M. Evans. High and low frequency torsional absorptions in nematic k21. *Journal of the Chemical Society, Faraday Transactions 2*, 73(2):285, 1977.

[28] C. J. Reid and M. W. Evans. Assignment of far infrared absorptions in liquid crystalline 4-n-heptyl-4′-cyanobiphenyl. *Molecular Physics*, 40(6):1523–1526, 1980.

[29] G. J. Evans, J. K. Moscicki, and M. W. Evans. The poley absorption in liquid crystals. *Journal of Molecular Liquids*, 32(2):149–160, 1986.

[30] U. M. S. Murthy and J. K. Vij. Submillimetre wave spectroscopy of 4-n-alkyl-4′-cyano biphenyl liquid crystals. *Liquid Crystals*, 4(5):529–542, 1989.

[31] F. W. Deeg and M. D. Fayer. Analysis of complex molecular dynamics in an organic liquid by polarization selective subpicosecond transient grating experiments. *The Journal of Chemical Physics*, 91(4):2269–2279, 1989.

[32] F. W. Deeg, J. J. Stankus, S. R. Greenfield, V. J. Newell, and M. D. Fayer. Anisotropic reorientational relaxation of biphenyl: Transient grating optical kerr effect measurements. *The Journal of Chemical Physics*, 90(12):6893–6902, 1989.

[33] B.-R. Hyun and E. L. Quitevis. Low-frequency spectrum of homeotropically aligned liquid crystals: optical heterodyne-detected raman-induced kerr effect spectroscopy of 4-octyl-4′-cyanobiphenyl. *Chemical Physics Letters*, 370(5–6):725–732, 2003.

[34] L. Cattaneo, M. Savoini, I. Muševič, A. Kimel, and T. Rasing. Ultrafast all-optical response of a nematic liquid crystal. *Optics Express*, 23(11):14010, 2015.

[35] R. Wilk, N. Vieweg, O. Kopschinski, T. Hasek, and M. Koch. THz spectroscopy of liquid crystals from the CB family. *Journal of Infrared, Millimeter, and Terahertz Waves*, 30(11):1139–1147, 2009.

[36] N. Vieweg, M. K. Shakfa, and M. Koch. BL037: A nematic mixture with high terahertz birefringence. *Optics Communications*, 284(7):1887–1889, 2011.

[37] N. Vieweg and M. Koch. Terahertz properties of liquid crystals with negative dielectric anisotropy. *Applied Optics*, 49(30):5764, 2010.

[38] N. Vieweg, M. K. Shakfa, B. Scherger, M. Mikulics, and M. Koch. THz properties of nematic liquid crystals. *Journal of Infrared, Millimeter, and Terahertz Waves*, 31(11):1312–1320, 2010.

[39] N. Vieweg, C. Jansen, M. K. Shakfa, M. Scheller, N. Krumbholz, R. Wilk, M. Mikulics, and M. Koch. Molecular properties of liquid crystals in the terahertz frequency range. *Optics Express*, 18(6):6097, 2010.

[40] N. Vieweg, M. K. Shakfa, and M. Koch. Molecular terahertz polarizability of PCH5, PCH7, and 5ocb. *Journal of Infrared, Millimeter, and Terahertz Waves*, 32(12):1367–1370, 2011.

[41] N. Vieweg, B. M. Fischer, M. Reuter, P. Kula, R. Dabrowski, M. A. Celik, G. Frenking, M. Koch, and P. U. Jepsen. Ultrabroadband terahertz spectroscopy of a liquid crystal. *Optics Express*, 20(27):28249, 2012.

[42] N. Vieweg, M. A. Celik, S. Zakel, V. Gupta, G. Frenking, and M. Koch. Terahertz absorption of nematic liquid crystals. *Journal of Infrared, Millimeter, and Terahertz Waves*, 35(5):478–485, 2014.

[43] F. Reinitzer. Beiträge zur kenntniss des cholesterins. *Monatshefte für Chemie - Chemical Monthly*, 9(1):421–441, 1888.

[44] S. Kumar. *Liquid Crystals*. Cambridge University Press, 2000.

[45] X. Chen, E. Korblova, D. Dong, X. Wei, R. Shao, L. Radzihovsky, M. A. Glaser, J. E. Maclennan, D. Bedrov, D. M. Walba, and N. A. Clark. First-principles experimental demonstration of ferroelectricity in a thermotropic nematic liquid crystal: Polar domains and striking electro-optics. *Proceedings of the National Academy of Sciences*, 117(25):14021–14031, 2020.

[46] W. Helfrich. Molecular theory of flow alignment of nematic liquid crystals. *The Journal of Chemical Physics*, 50(1):100–106, 1969.

[47] F. J. Kahn. The molecular physics of liquid-crystal devices. *Physics Today*, 35(5):66–74, 1982.

[48] I. C. Khoo and Y. R. Shen. Liquid crystals: Nonlinear optical properties and processes. *Optical Engineering*, 24(4), 1985.

[49] S.-T. Wu. Infrared properties of nematic liquid crystals: An overview. *Optical Engineering*, 26(2):262120, 1987.

[50] H. de Vries. Rotatory power and other optical properties of certain liquid crystals. *Acta Crystallographica*, 4(3):219–226, 1951.

[51] J.-I. Hanna. *Charge Carrier Transport in Liquid Crystalline Semiconductors*, pages 39–64. Springer Netherlands, 2012.

[52] S. Varytimiadou, D. Revignas, F. Giesselmann, and A. Ferrarini. Elasticity of lyotropic nematic liquid crystals: a review of experiments, theory and simulation. *Liquid Crystals Reviews*, 12(1):57–104, 2024.

[53] V. Luzzati, H. Mustacchi, and A. Skoulios. Structure of the liquid-crystal phases of the soap–water system: Middle soap and neat soap. *Nature*, 180(4586):600–601, 1957.

[54] J. W. McBain. Liquid crystals—soap solutions and x-rays. *Nature*, 114(2854):49–49, 1924.

[55] M. Kleman and O. D. Lavrentovich. *Soft Matter Physics: An Introduction*. Springer New York, 2003.

[56] C. S. Rosenblatt, R. Pindak, N. A. Clark, and R. B. Meyer. The parabolic focal conic: a new smectic a defect. *Journal de Physique*, 38(9):1105–1115, 1977.

[57] W. Chen and H. Yokoyama. Rapid thickness mapping of free-standing smectic films using colour information of reflected light. *Liquid Crystals*, 48(6):873–887, 2020.

[58] M. F. Palermo, L. Muccioli, and C. Zannoni. Molecular organization in freely suspended nano-thick 8cb smectic films. an atomistic simulation. *Physical Chemistry Chemical Physics*, 17(39):26149–26159, 2015.

[59] K. P. Gueu, E. Megnassan, and A. Proutiere. Dipole moments of 4-n alkyl-4′-cyanobiphenyl molecules (from ocb to 12cb) measurement in four solvents and theoretical calculations. *Molecular Crystals and Liquid Crystals*, 132(3–4):303–323, 1986.

[60] X. Wei, J. B. Hooper, and D. Bedrov. Influence of electrostatic interactions on the properties of cyanobiphenyl liquid crystals predicted from atomistic molecular dynamics simulations. *Liquid Crystals*, pages 1–16, 2016.

[61] A. Selevou, G. Papamokos, M. Steinhart, and G. Floudas. 8ocb and 8cb liquid crystals confined in nanoporous alumina: Effect of confinement on the structure and dynamics. *The Journal of Physical Chemistry B*, 121(30):7382–7394, 2017.

[62] Synthon chemicals webshop: https://shop.synthon-chemicals.com/en/liquid-crystals/, 2022. Accessed: 2025-06-30.

[63] A. Selevou, G. Papamokos, T. Yildirim, H. Duran, M. Steinhart, and G. Floudas. Eutectic liquid crystal mixture e7 in nanoporous alumina. effects of confinement on the thermal and concentration fluctuations. *RSC Advances*, 9(65):37846–37857, 2019.

[64] S.-T. Wu. Refractive index dispersions of liquid crystals. *Optical Engineering*, 32(8):1775, 1993.

[65] J. Li, C.-H. Wen, S. Gauza, R. Lu, and S.-T. Wu. Refractive indices of liquid crystals for display applications. *Journal of Display Technology*, 1(1):51–61, 2005.

[66] V. Tkachenko, G. Abbate, A. Marino, F. Vita, M. Giocondo, A. Mazzulla, F. Ciuchi, and L. D. Stefano. Nematic liquid crystal optical dispersion in the visible-near infrared range. *Molecular Crystals and Liquid Crystals*, 454(1):263/[665]–271/[673], 2006.

[67] S. Keiber, S. Sederberg, A. Schwarz, M. Trubetskov, V. Pervak, F. Krausz, and N. Karpowicz. Electro-optic sampling of near-infrared waveforms. *Nature Photonics*, 10(3):159–162, 2016.

[68] M. Tonouchi. Cutting-edge terahertz technology. *Nature Photonics*, 1(2):97–105, 2007.

[69] P. U. Jepsen, D. G. Cooke, and M. Koch. Terahertz spectroscopy and imaging – modern techniques and applications. *Laser &; Photonics Reviews*, 5(1):124–166, 2010.

[70] J. Neu and C. A. Schmuttenmaer. Tutorial: An introduction to terahertz time domain spectroscopy (thz-tds). *Journal of Applied Physics*, 124(23), 2018.

[71] A. Leitenstorfer, A. S. Moskalenko, T. Kampfrath, J. Kono, E. Castro-Camus, K. Peng, N. Qureshi, D. Turchinovich, K. Tanaka, A. G. Markelz, M. Havenith, C. Hough, H. J. Joyce, W. J. Padilla, B. Zhou, K.-Y. Kim, X.-C. Zhang, P. U. Jepsen, S. Dhillon, M. Vitiello, E. Linfield, A. G. Davies, M. C. Hoffmann, R. Lewis, M. Tonouchi, P. Klarskov, T. S. Seifert, Y. A. Gerasimenko, D. Mihailovic, R. Huber, J. L. Boland, O. Mitrofanov, P. Dean, B. N. Ellison, P. G. Huggard, S. P. Rea, C. Walker, D. T. Leisawitz, J. R. Gao, C. Li, Q. Chen, G. Valušis, V. P. Wallace, E. Pickwell-MacPherson, X. Shang, J. Hesler, N. Ridler, C. C. Renaud, I. Kallfass, T. Nagatsuma, J. A. Zeitler, D. Arnone, M. B. Johnston, and J. Cunningham. The 2023 terahertz science and technology roadmap. *Journal of Physics D: Applied Physics*, 56(22):223001, 2023.

[72] M. Koch, D. M. Mittleman, J. Ornik, and E. Castro-Camus. Terahertz time-domain spectroscopy. *Nature Reviews Methods Primers*, 3(1), 2023.

[73] Y.-S. Lee. *Principles of Terahertz Science and Technology*. Springer Publishing Company, Incorporated, 1st edition, 2008.

[74] N. M. Burford and M. O. El-Shenawee. Review of terahertz photoconductive antenna technology. *Optical Engineering*, 56(1):010901, 2017.

[75] A. Valavanis, P. Dean, Y. L. Lim, R. Alhathlool, M. Nikolic, R. Kliese, S. P. Khanna, D. Indjin, S. J. Wilson, A. D. Rakic, E. H. Linfield, and G. Davies. Self-mixing interferometry with terahertz quantum cascade lasers. *IEEE Sensors Journal*, 13(1):37–43, 2013.

[76] D. J. Cook and R. M. Hochstrasser. Intense terahertz pulses by four-wave rectification in air. *Optics Letters*, 25(16):1210, 2000.

[77] M. Kress, T. Löffler, S. Eden, M. Thomson, and H. G. Roskos. Terahertz-pulse generation by photoionization of air with laser pulses composed of both fundamental and second-harmonic waves. *Optics Letters*, 29(10):1120, 2004.

[78] C. Bull, S. M. Hewett, R. Ji, C.-H. Lin, T. Thomson, D. M. Graham, and P. W. Nutter. Spintronic terahertz emitters: Status and prospects from a materials perspective. *APL Materials*, 9(9), 2021.

[79] D. W. Faries, K. A. Gehring, P. L. Richards, and Y. R. Shen. Tunable far-infrared radiation generated from the difference frequency between two ruby lasers. *Physical Review*, 180(2):363–365, 1969.

[80] J. R. Danielson, J. D. Wetzel, K. L. Vodopyanov, and Y.-S. Lee. Tunable narrowband thz generation by type-ii dfg with linearly chirped optical pulses in znte. In *2007 Conference on Lasers and Electro-Optics - Pacific Rim*, pages 1–2. IEEE, 2007.

[81] Y.-S. Lee, T. Meade, V. Perlin, H. Winful, T. B. Norris, and A. Galvanauskas. Generation of narrow-band terahertz radiation via optical rectification of femtosecond pulses in periodically poled lithium niobate. *Applied Physics Letters*, 76(18):2505–2507, 2000.

[82] R. T. Jongma, W. J. van der Zande, A. F. G. van der Meer, U. Lehnert, P. Michel, R. Wünsch, C. A. J. van der Geer, K. Dunkel, C. Piel, and P. J. M. van der Slot. Design of the nijmegen high-resolution thz-fel. In *Proceedings 30th Annual International Free Electron Laser Conference*, pages 200–203. Pohang Accelerator Laboratory, 2009. 30th International Free Electron Laser Conference, FEL 2008, FEL ; Conference date: 24-08-2008 Through 29-08-2008.

[83] W. Seidel, O. Drachenko, M. Gensch, M. Helm, M. Kuntzsch, M. Justus, U. Lehnert, P. Michel, M. Mittendorff, H. Schneider, R. Schurig, M. Teich, and S. Winnerl. The thz user facility felbe at the radiation source elbe of helmholtz-zentrum dresden-rossendorf. In *2013 38th International Conference on Infrared, Millimeter, and Terahertz Waves (IRMMW-THz)*, pages 1–1. IEEE, 2013.

[84] B. Green, S. Kovalev, V. Asgekar, G. Geloni, U. Lehnert, T. Golz, M. Kuntzsch, C. Bauer, J. Hauser, J. Voigtlaender, B. Wustmann, I. Koesterke, M. Schwarz, M. Freitag, A. Arnold, J. Teichert, M. Justus, W. Seidel, C. Ilgner, N. Awari, D. Nicoletti, S. Kaiser, Y. Laplace, S. Rajasekaran, L. Zhang, S. Winnerl, H. Schneider, G. Schay, I. Lorincz, A. A. Rauscher, I. Radu, S. Mährlein, T. H. Kim, J. S. Lee, T. Kampfrath, S. Wall, J. Heberle, A. Malnasi-Csizmadia, A. Steiger, A. S. Müller, M. Helm, U. Schramm, T. Cowan, P. Michel, A. Cavalleri, A. S. Fisher, N. Stojanovic, and M. Gensch. High-field high-repetition-rate sources for the coherent thz control of matter. *Scientific Reports*, 6(1), 2016.

[85] M. Bass, P. A. Franken, J. F. Ward, and G. Weinreich. Optical rectification. *Physical Review Letters*, 9(11):446–448, 1962.

[86] K. H. Yang, P. L. Richards, and Y. R. Shen. Generation of far-infrared radiation by picosecond light pulses in linbo3. *Applied Physics Letters*, 19(9):320–323, 1971.

[87] B. E. A. Saleh and M. C. Teich. *Fundamentals of Photonics*. Wiley & Sons, Incorporated, John, 2013.

[88] C. Vicario, M. Jazbinsek, A. V. Ovchinnikov, O. V. Chefonov, S. I. Ashitkov, M. B. Agranat, and C. P. Hauri. High efficiency thz generation in dstms, dast and oh1 pumped by cr:forsterite laser. *Optics Express*, 23(4):4573, 2015.

[89] S. Mansourzadeh, T. Vogel, A. Omar, T. O. Buchmann, E. J. R. Kelleher, P. U. Jepsen, and C. J. Saraceno. Towards intense ultra-broadband high repetition rate terahertz sources based on organic crystals [invited]. *Optical Materials Express*, 13(11):3287, 2023.

[90] M. Tani, M. Herrmann, and K. Sakai. Generation and detection of terahertz pulsed radiation with photoconductive antennas and its application to imaging. *Measurement Science and Technology*, 13(11):1739–1745, 2002.

[91] J. A. Valdmanis, G. Mourou, and C. W. Gabel. Picosecond electro-optic sampling system. *Applied Physics Letters*, 41(3):211–212, 1982.

[92] Q. Wu and X.-C. Zhang. Free-space electro-optic sampling of terahertz beams. *Applied Physics Letters*, 67(24):3523–3525, 1995.

[93] M. H. M. Schmitt. Investigation of low-frequency vibrational modes in representative thermotropic liquid crystals. Bachelor thesis, Heidelberg University, 2024.

[94] B. R. Steffen. *Electro-Optic Methods for Longitudinal Bunch Diagnostics at FLASH*. Phd thesis, Hamburg University, 2007.

[95] A. Leitenstorfer, S. Hunsche, J. Shah, M. C. Nuss, and W. H. Knox. Detectors and sources for ultrabroadband electro-optic sampling: Experiment and theory. *Applied Physics Letters*, 74(11):1516–1518, 1999.

[96] R. Mankowsky, M. Sander, S. Zerdane, J. Vonka, M. Bartkowiak, Y. Deng, R. Winkler, F. Giorgianni, G. Matmon, S. Gerber, P. Beaud, and H. T. Lemke. New insights into correlated materials in the time domain—combining far-infrared excitation with x-ray probes at cryogenic temperatures. *Journal of Physics: Condensed Matter*, 33(37):374001, 2021.

[97] W. L. Faust and Charles H. Henry. Mixing of visible and near-resonance infrared light in gap. *Physical Review Letters*, 17(25):1265–1268, 1966.

[98] Q. Wu and X.-C. Zhang. 7 terahertz broadband gap electro-optic sensor. *Applied Physics Letters*, 70(14):1784–1786, 1997.

[99] K. J. Kaltenecker, E. J. R. Kelleher, B. Zhou, and P. U. Jepsen. Attenuation of thz beams: A "how to" tutorial. *Journal of Infrared, Millimeter, and Terahertz Waves*, 40(8):878–904, 2019.

[100] W. Withayachumnankul and M. Naftaly. Fundamentals of measurement in terahertz time-domain spectroscopy. *Journal of Infrared, Millimeter, and Terahertz Waves*, 35(8):610–637, 2013.

[101] E. Hack, I. Shorubalko, J. Graf, P. Zolliker, and E. Mavrona. Fabrication of freestanding photonic devices combining polymer films with microfabrication techniques and 3d printing. *Optics Express*, 31(18):29968, 2023.

[102] L. Mutter, F. D. Brunner, Z. Yang, M. Jazbinšek, and P. Günter. Linear and nonlinear optical properties of the organic crystal dstms. *Journal of the Optical Society of America B*, 24(9):2556, 2007.

[103] I. E. Gordon, L. S. Rothman, R. J. Hargreaves, R. Hashemi, E. V. Karlovets, F. M. Skinner, E. K. Conway, C. Hill, R. V. Kochanov, Y. Tan, P. Wcisło, A. A. Finenko, K. Nelson, P. F. Bernath, M. Birk, V. Boudon, A. Campargue, K. V. Chance, A. Coustenis, B. J. Drouin, J.–M. Flaud, R. R. Gamache, J. T. Hodges, D. Jacquemart, E. J. Mlawer, A. V. Nikitin, V. I. Perevalov, M. Rotger, J. Tennyson, G. C. Toon, H. Tran, V. G. Tyuterev, E. M. Adkins, A. Baker, A. Barbe, E. Canè, A. G. Császár, A. Dudaryonok, O. Egorov, A. J. Fleisher, H. Fleurbaey, A. Foltynowicz, T. Furtenbacher, J. J. Harrison, J.–M. Hartmann, V.–M. Horneman, X. Huang, T. Karman, J. Karns, S. Kassi, I. Kleiner, V. Kofman, F. Kwabia–Tchana, N. N. Lavrentieva, T. J. Lee, D. A. Long, A. A. Lukashevskaya, O. M. Lyulin, V. Yu. Makhnev, W. Matt, S. T. Massie, M. Melosso, S. N. Mikhailenko, D. Mondelain, H. S. P. Müller, O. V. Naumenko, A. Perrin, O. L. Polyansky, E. Raddaoui, P. L. Raston, Z. D. Reed, M. Rey, C. Richard, R. Tóbiás, I. Sadiek, D. W. Schwenke, E. Starikova, K. Sung, F. Tamassia, S. A. Tashkun, J. Vander Auwera, I. A. Vasilenko, A. A. Vigasin, G. L. Villanueva, B. Vispoel, G. Wagner, A. Yachmenev, and S. N. Yurchenko. The hitran2020 molecular spectroscopic database. *Journal of Quantitative Spectroscopy and Radiative Transfer*, 277:107949, 2022.

[104] P. U. Jepsen. Phase retrieval in terahertz time-domain measurements: a "how to" tutorial. *Journal of Infrared, Millimeter, and Terahertz Waves*, 40(4):395–411, 2019.

[105] J. M. Fornies-Marquina, J. Letosa, M. Garcia-Gracia, and J. M. Artacho. Error propagation for the transformation of time domain into frequency domain. *IEEE Transactions on Magnetics*, 33(2):1456–1459, 1997.

[106] E. Denakpo, T. Hannotte, N. Osseiran, F. Orieux, and R. Peretti. Signal estimation and uncertainties extraction in terahertz time-domain spectroscopy. *IEEE Transactions on Instrumentation and Measurement*, 74:1–13, 2025.

[107] P. U. Jepsen and B. M. Fischer. Dynamic range in terahertz time-domain transmission and reflection spectroscopy. *Optics Letters*, 30(1):29, 2005.

[108] M. F. Palermo, A. Pizzirusso, L. Muccioli, and C. Zannoni. An atomistic description of the nematic and smectic phases of 4-n-octyl-4′ cyanobiphenyl (8cb). *The Journal of Chemical Physics*, 138(20), 2013.

[109] J. G. Vilhena, L. Greff da Silveira, P. R. Livotto, I. Cacelli, and G. Prampolini. Automated parameterization of quantum mechanically derived force fields for soft materials and complex fluids: Development and validation. *Journal of Chemical Theory and Computation*, 17(7):4449–4464, 2021.

[110] F. Jensen. *Introduction to Computational Chemistry*. Wiley.

[111] P. Friebel, D. R. Galimberti, M. Savoini, and L. Cattaneo. Unveiling low thz dynamics of liquid crystals: Identification of intermolecular interaction among intramolecular modes. *The Journal of Physical Chemistry B*, 128(2):596–602, 2024.

[112] M. J. Frisch, G. W. Trucks, H. B. Schlegel, G. E. Scuseria, M. A. Robb, J. R. Cheeseman, G. Scalmani, V. Barone, G. A. Petersson, H. Nakatsuji, X. Li, M. Caricato, A. V. Marenich, J. Bloino, B. G. Janesko, R. Gomperts, B. Mennucci, H. P. Hratchian, J. V. Ortiz, A. F. Izmaylov, J. L. Sonnenberg, Williams, F. Ding, F. Lipparini, F. Egidi, J. Goings, B. Peng, A. Petrone, T. Henderson, D. Ranasinghe, V. G. Zakrzewski, J. Gao, N. Rega, G. Zheng, W. Liang, M. Hada, M. Ehara, K. Toyota, R. Fukuda, J. Hasegawa, M. Ishida, T. Nakajima, Y. Honda, O. Kitao, H. Nakai, T. Vreven, K. Throssell, J. A. Montgomery Jr., J. E. Peralta, F. Ogliaro, M. J. Bearpark, J. J. Heyd, E. N. Brothers, K. N. Kudin, V. N. Staroverov, T. A. Keith, R. Kobayashi, J. Normand, K. Raghavachari, A. P. Rendell, J. C. Burant, S. S. Iyengar, J. Tomasi, M. Cossi, J. M. Millam, M. Klene, C. Adamo, R. Cammi, J. W. Ochterski, R. L. Martin, K. Morokuma, O. Farkas, J. B. Foresman, and D. J. Fox. Gaussian 16 rev. c.01, 2016.

[113] R. Dennington, T. A. Keith, and J. M. Millam. Gaussview Version 6.1, 2016. Semichem Inc. Shawnee Mission KS.

[114] C. Lee, W. Yang, and R. G. Parr. Development of the colle-salvetti correlation-energy formula into a functional of the electron density. *Physical Review B*, 37(2):785–789, 1988.

[115] A. D. Becke. Density-functional thermochemistry. III. the role of exact exchange. *The Journal of Chemical Physics*, 98(7):5648–5652, 1993.

[116] S. Grimme, J. Antony, S. Ehrlich, and H. Krieg. A consistent and accurate ab initio parametrization of density functional dispersion correction (dft-d) for the 94 elements h-pu. *The Journal of Chemical Physics*, 132(15), 2010.

[117] S. Takabatake and T. Shikata. Evidence of anti-parallel dimer formation of 4-cyano-4′-alkyl biphenyls in isotropic cyclohexane solution. *Physical Chemistry Chemical Physics*, 17(3):1934–1942, 2015.

[118] U. Häberle and G. Diezemann. Dynamic kerr effect responses in the terahertz range. *The Journal of Chemical Physics*, 122(18), 2005.

[119] Y. P. Kalmykov. Matrix method calculation of the kerr effect transient and ac stationary responses of arbitrary shaped macromolecules. *The Journal of Chemical Physics*, 131(7), 2009.

[120] M. Cherasse. *Ultrafast dynamics in hybrid perovskites*. Theses, Institut Polytechnique de Paris, 2022.

[121] M. Zalkovskij, A. C. Strikwerda, K. Iwaszczuk, A. Popescu, D. Savastru, R. Malureanu, A. V. Lavrinenko, and P. U. Jepsen. Terahertz-induced kerr effect in amorphous chalcogenide glasses. *Applied Physics Letters*, 103(22), 2013.

[122] V. E. Rogalin, I. A. Kaplunov, and G. I. Kropotov. Optical materials for the thz range. *Optics and Spectroscopy*, 125(6):1053–1064, 2018.

[123] C. L. Davies, J. B. Patel, C. Q. Xia, L. M. Herz, and M. B. Johnston. Temperature-dependent refractive index of quartz at terahertz frequencies. *Journal of Infrared, Millimeter, and Terahertz Waves*, 39(12):1236–1248, 2018.

[124] M. Sajadi, M. Wolf, and T. Kampfrath. Terahertz-field-induced optical birefringence in common window and substrate materials. *Optics Express*, 23(22):28985, 2015.

[125] S. Kefer, T. Limbach, N. Pape, K. Klamt, B. Schmauss, and R. Hellmann. Birefringence in injection-molded cyclic olefin copolymer substrates and its impact on integrated photonic structures. *Polymers*, 16(2):168, 2024.

[126] P. Temple-Boyer, L. Jalabert, L. Masarotto, J. L. Alay, and J. R. Morante. Properties of nitrogen doped silicon films deposited by low-pressure chemical vapor deposition from silane and ammonia. *Journal of Vacuum Science & Technology A: Vacuum, Surfaces, and Films*, 18(5):2389–2393, 2000.

[127] F. Karouta, K. Vora, J. Tian, and C. Jagadish. Structural, compositional and optical properties of pecvd silicon nitride layers. *Journal of Physics D: Applied Physics*, 45(44):445301, 2012.

[128] W. Xiong, H. Jiang, T. Li, P. Zhang, Q. Xu, X. Zhao, G. Wang, Y. Liu, Y. Luo, Z. Li, J. Li, J. Yu, Z. Chao, W. Wang, and H. H. Radamson. Sinx films and membranes for photonic and mems applications. *Journal of Materials Science: Materials in Electronics*, 31(1):90–97, 2019.

[129] C. Chen, V. Palacio-Betancur, S. Norouzi, P. F. Zubieta-Rico, N. Chang, M. Sadati, S. J. Rowan, and J. J. de Pablo. Lcpom: Precise reconstruction of polarized optical microscopy images of liquid crystals. *Chemistry of Materials*, 36(7):3081–3091, 2024.

[130] L. Li, M. Salamończyk, S. Shadpour, C. Zhu, A. Jákli, and T. Hegmann. An unusual type of polymorphism in a liquid crystal. *Nature Communications*, 9(1), 2018.

[131] B.-X. Li, V. Borshch, R.-L. Xiao, S. Paladugu, T. Turiv, S. V. Shiyanovskii, and O. D. Lavrentovich. Electrically driven three-dimensional solitary waves as director bullets in nematic liquid crystals. *Nature Communications*, 9(1), 2018.

[132] M. Salamończyk, N. Vaupotič, D. Pociecha, R. Walker, J. M. D. Storey, C. T. Imrie, C. Wang, C. Zhu, and E. Gorecka. Multi-level chirality in liquid crystals formed by achiral molecules. *Nature Communications*, 10(1), 2019.

[133] M. S. Sen, P. Brahma, S.. K. Roy, D. K. Mukherjee, and S. B. Roy. Birefringence and order parameter of some alkyl and alkoxycyanobiphenyl liquid crystals. *Molecular Crystals and Liquid Crystals*, 100(3-4):327–340, 1983.

[134] S. Sen, K. Kali, S. K. Roy, and S. B. Roy. Refractive indices and dielectric studies of three phenylcyclohexane liquid crystals in the nematic phase. *Molecular Crystals and Liquid Crystals*, 126(2-4):269–279, 1985.

[135] P. van der Schoot. *Molecular Theory of Nematic (and Other) Liquid Crystals*. Springer International Publishing, 2022.

[136] N. Vieweg, C. Jansen, M. K. Shakfa, M. Scheller, N. Krumbholz, R. Wilk, M. Mikulics, and M. Koch. Molecular properties of liquid crystals in the terahertz frequency range. *Optics Express*, 18(6):6097, 2010.

[137] M. F. Vuks. Determination of the optical anisotropy of aromatic molecules from the double refraction of crystals. *Optics and Spectroscopy*, 20:361, 1966.

[138] I. Haller. Thermodynamic and static properties of liquid crystals. *Progress in Solid State Chemistry*, 10:103–118, 1975.

[139] D. L. Cheung, S. J. Clark, and M. R. Wilson. Calculation of the rotational viscosity of a nematic liquid crystal. *Chemical Physics Letters*, 356(1–2):140–146, 2002.

[140] S. J. Shivaraja, R. K. Gupta, S. Kumar, and V. Manjuladevi. Enhanced electro-optical response of nematic liquid crystal doped with functionalised silver nanoparticles in twisted nematic configuration. *Liquid Crystals*, 47(11):1678–1690, 2020.

[141] A. Schinas, S. B. Atata, D. Tsiourvas, and I. Lelidis. Influence of carbon quantum dots on the orientational order and rotational viscosity of 8cb. *Nanomaterials*, 15(16):1278, 2025.

[142] L. Y. Beliaev, E. Shkondin, A. V. Lavrinenko, and O. Takayama. Optical, structural and composition properties of silicon nitride films deposited by reactive radio-frequency sputtering, low pressure and plasma-enhanced chemical vapor deposition. *Thin Solid Films*, 763:139568, 2022.

[143] H. Kaveh, F. Jahangiri, and T. Amini. Silicon nitride based photonic crystal fiber with highly improved birefringence for low loss terahertz propagation. *Optics Continuum*, 1(2):388, 2022.

[144] P. G. Lynch, S. Baughman, T. N. Mihm, S. Sharifzadeh, and R. R. Frontiera. Identifying driving and spectator phonon modes in pentacene exciton transport. *Journal of the American Chemical Society*, 147(27):23705–23714, 2025.

[145] K. Reimann, M. Woerner, and T. Elsaesser. Two-dimensional terahertz spectroscopy of condensed-phase molecular systems. *The Journal of Chemical Physics*, 154(12), 2021.

[146] M. C. Beard, G. M. Turner, and C. A. Schmuttenmaer. Transient photoconductivity in gaas as measured by time-resolved terahertz spectroscopy. *Physical Review B*, 62(23):15764–15777, 2000.

[147] F. Novelli, A. Buchmann, I. Yousaf, L.-L. Stiewe, W. Bronsch, F. Cilento, C. Hoberg, and M. Havenith. High-mobility electrons in aqueous iodide solutions. *ACS Omega*, 10(5):5097–5104, 2025.

Acknowledgements

My biggest thanks undoubtedly goes to Laura. You gave me a chance, which means so much to me. At times it was tough, and too often because of me, but in the end I am proud of what we managed to achieve so far. But more importantly, the person who entered your lab for the first time years ago is now a stranger to me. I am a different person today, and it's thanks to your trust. The empty lab was my reason to join, but I am ending this chapter full of memories. I will never forget my time here.

To Daria, I want to say thank you for helping us along the way and for always being available. Without you, I'm not sure we would have come this far. To Matteo, thank you for taking the time and giving advice when I wasn't sure how to continue. I value it like gold. And to Riccardo, our time here in the beginning was short, but thanks to your help it was easier to do the first steps in this new project.

Also the technical help I received here at the institute is deserving of deep thanks. Especially Alex and Ranko, from the electronic workshop Michael and Thomas, and Yannick from the mechanical workshop have helped a great deal. Without them, it simply would not have been possible.

An amazing number of people have offered help with their advice, internally and externally. They listened to what I was thinking and actually gave thoughtful answers that pointed me towards new directions that I hadn't considered. I would never take this for granted and I am grateful to them. A special mention goes to Thomas, who is always full of ideas.

I also want to express my thanks to my examiners, Prof. Fischer, Prof. Bereau, and Priv.-Doz. Quint, for offering their time to engage with my work.

A lot of students and colleagues have passed through during my time here. They brought new energy, which is always needed. Henrick, Ivan, Marius, Max, Ellias, Anna, Luise, Matthias, Natalia, thank you all. Especially to Andrea, thank you for suffering through PSI with us on top of everything else.

Marta, there is no chance I would have kept my sanity without you in this last push and I don't think I was able to properly convey how much you mean to me. I am so happy that you joined and that I got to know you, and hope I could contribute to making your time here a little bit happier as well.

Mama, Papa, und Kevin, diese Zeit hat mir gezeigt, dass ich mich immer auf euch verlassen kann, und ich werde auch für euch da sein.

Looking back, the science is exciting, but it's the people that I have memories of. I was lucky to have met them.

A. THz Kerr Fits

The THz Kerr traces are fitted by the rotational diffusion model. Whereas in the main text the driven response is excluded, since it is not captured by the model and therefore would skew the results, the possibility remains that it does fir. Here, in Figure A.1 for PCH5, Figure A.2 for 8OCB, and Figure A.3 for 8CB, fit results are presented without any exclusion of data points. As can be seen by comparison of the main fits and the residuals, the results are noticeable worse.

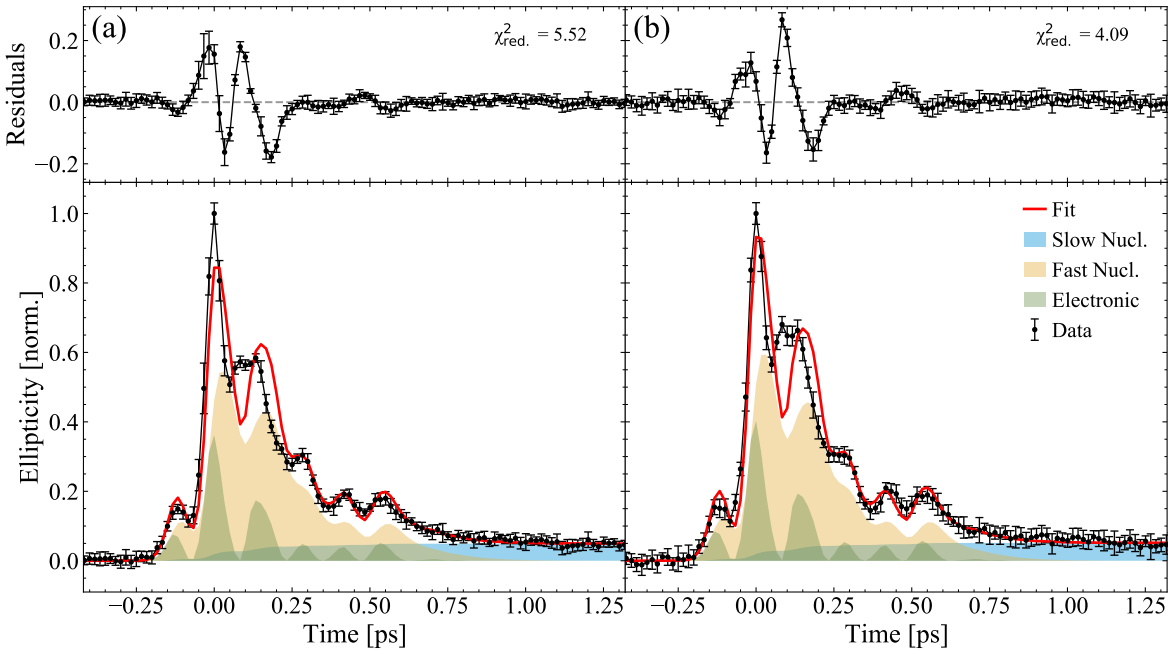

Figure A.1.: Rotational diffusion fits to the full PCH5 THz Kerr data

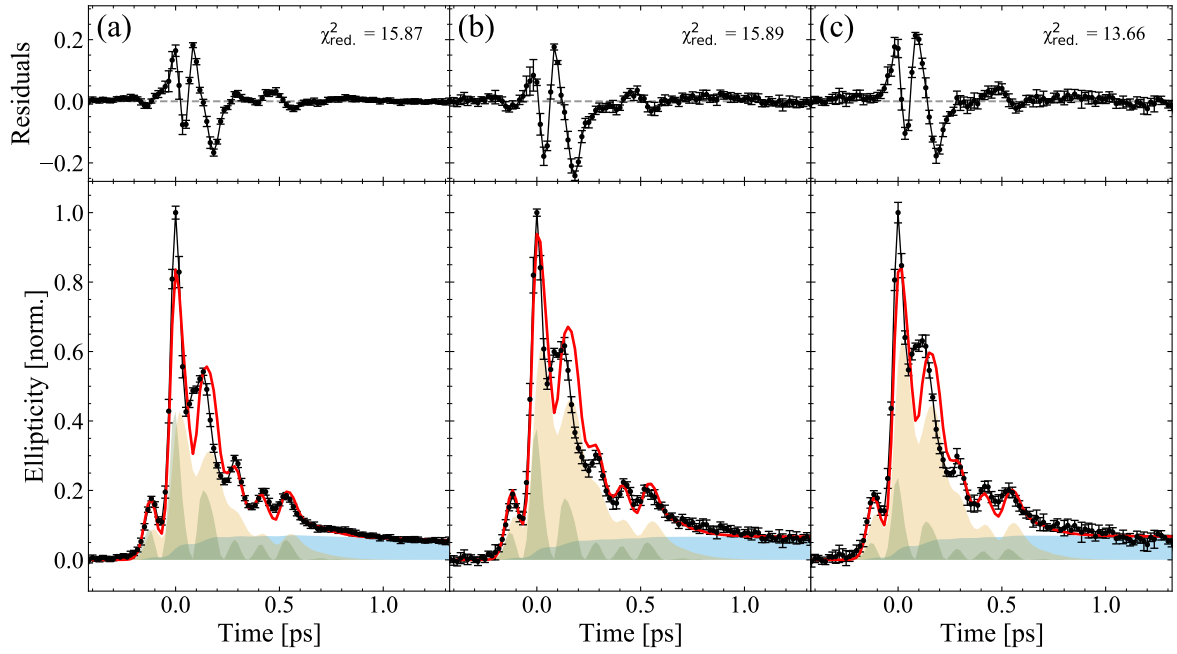

Figure A.2.: Rotational diffusion fits to the full 8OCB THz Kerr data

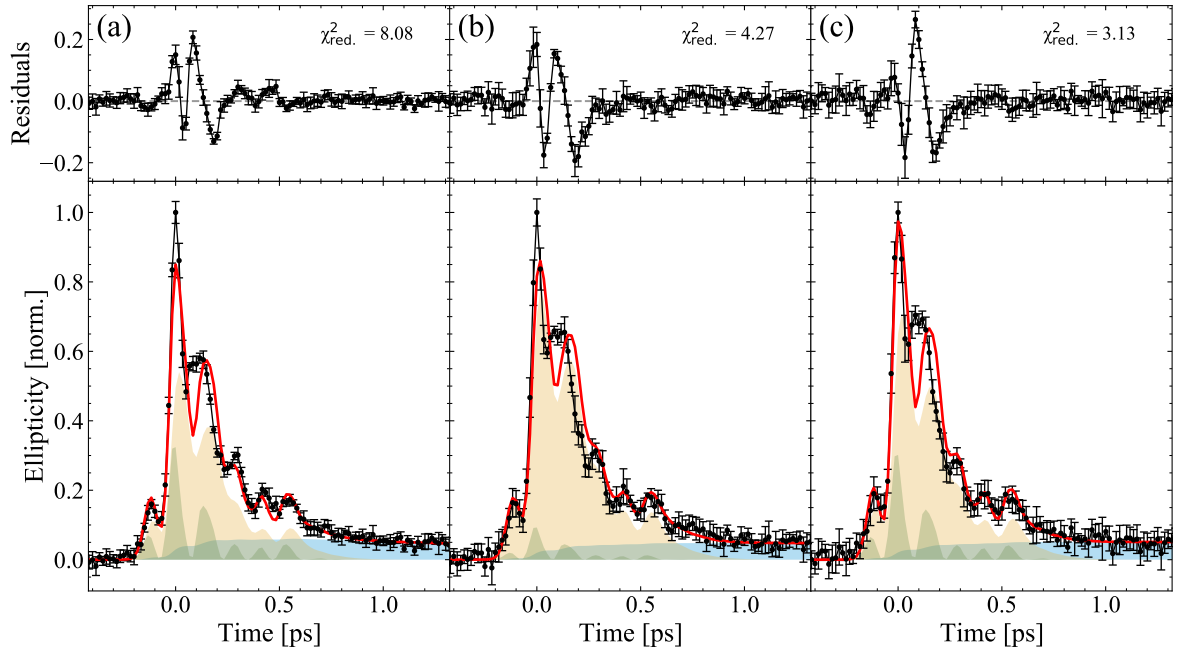

Figure A.3.: Rotational diffusion fits to the full 8CB THz Kerr data

B. 1.5 THz driven response

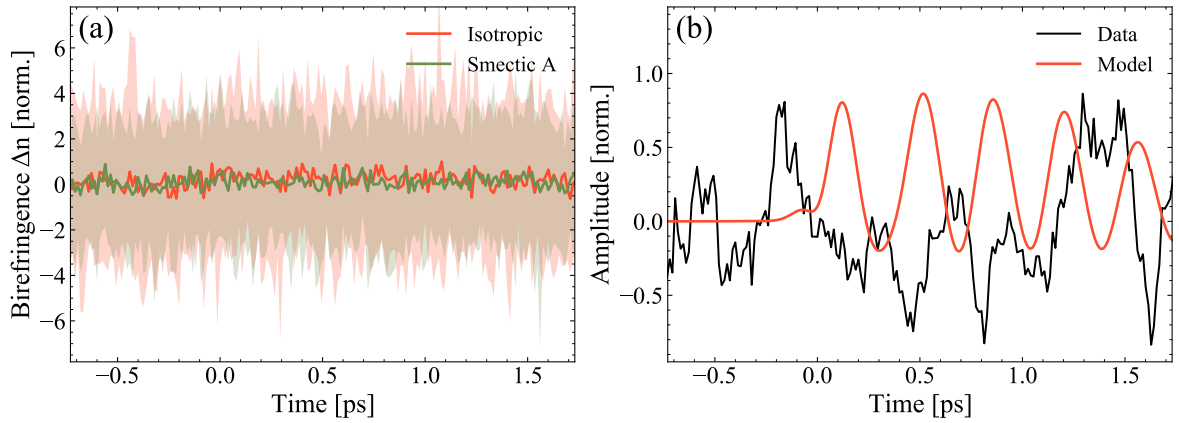

Figure B.1.: (a) 1.5 THz *Kerr responses for isotropic and smectic phases of 8OCB. (b) The isolated coherently driven response and the model prediction as normalized traces for comparison. Note: given the large uncertainty, a moving average has been applied on the Kerr traces before signal subtraction for improved readability.*

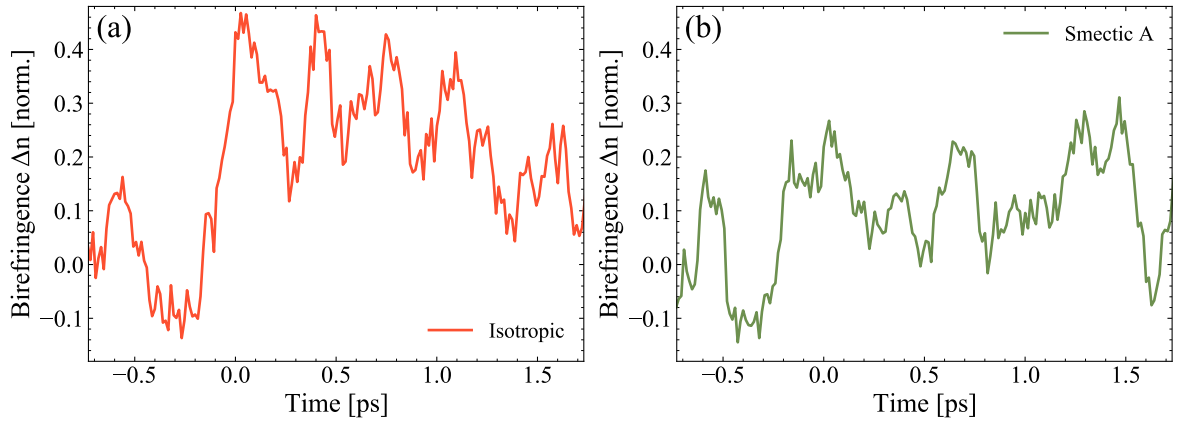

Figure B.2.: (a) 1.5 THz *Kerr responses for (a) isotropic and (b) smectic phases of 8OCB with applied moving average. A clear effect after time zero is visible.*